Non-Contact Microscale Manipulation using laser-induced convection flows

Emir Augusto Vela Saavedra

NON-CONTACT MICROSCALE MANIPULATION USING LASER-INDUCED CONVECTION FLOWS

THÈSE

présentée à

L'UNIVERSITÉ PIERRE ET MARIE CURIE

ÉCOLE DOCTORALE 391
SMAER Sciences Mécaniques, Acoustique, Électronique et Robotique de Paris

par

Emir Augusto VELA SAAVEDRA

pour l'obtention du grade de

DOCTEUR DE L'UNIVERSITÉ PIERRE ET MARIE CURIE

Spécialité:
Mécanique - Robotique

A soutenir le 28 mai 2010

JURY

Mr. Charles BAROUD	Professeur à l'École Polytechnique	Rapporteur
Mr. Pierre LAMBERT	Professeur à l'Université Libre de Bruxelles	Rapporteur
Mr. Stéphane ZALESKI	Professeur à l'Université Pierre et Marie Curie	Examinateur
Mr. Yves BELLOUARD	Professeur à l'Université Technologique d'Eindhoven	Examinateur
Mr. Moustapha HAFEZ	Docteur-Ingénieur CEA LIST	Co-directeur de thèse
Mr. Stéphane RÉGNIER	Professeur à l'Université Pierre et Marie Curie	Directeur de thèse

Contents

List of Figures

List of Tables

Notations

$\overline{\boldsymbol{\sigma}} = \sigma_{ij}$	Total stress tensor $[N\ m^{-2}]$
F_s	Forces acting in surfaces or Stress forces $[N]$
F_v	Body Forces $[N]$
$\boldsymbol{\nabla} = \dfrac{\partial}{\partial xi}$	Gradient operator $[m^{-1}]$
$x = xi$	coordinate system $[m]$
$\boldsymbol{u} = u_i$	Velocity field of the fluid $[m\ s^{-1}]$
∂S	Surface of a fluid particle $[m^2]$
∂V	Volume of the fluid particle $[m^3]$
β	Coefficient of thermal expansion $[K^{-1}]$
γ	Surface tension $[N\ m^{-1}]$
κ	Thermal diffusivity $[m^2 s^{-1}]$
$\mu = \rho\nu$	Dynamic viscosity $[N\ s\ m^{-2}]$
ν	Cinematic viscosity $[m^2\ s^{-1}]$
$\rho = \dfrac{\partial m}{\partial V}$	Density $[kg\ m^{-3}]$
b	Superficial tension's temperature variation rate $[K^{-1}]$
C_p	Specific heat at constant pressure $[J\ kg^{-1}\ K^{-1}]$
m	Mass $[kg]$
ρ_0	Referential density $[kg\ m^{-3}]$
L	Characteristic length $[m]$
U	Characteristic velocity $[ms^{-1}]$
λ	Laser wavelength $[m]$
I	Radiation intensity $[W\ m^2]$
Q_l	Volumetric heat flux induced by the laser absorption $[J\ s^{-1}]$

Introduction

This work relates to the automated parallel manipulation of parts at sub-millimeter scale and is a part of EU funded GOLEM Project. The main challenge at this scale is to develop novel methods for high throughput parallel assembly of components of a few hundreds of micrometers. At this scale, a serial approach would be extremely limited by the requirements on precision, speed ans especially by the particularities of physics.

The proposed approach in this work is opto-fluidic, based on the Marangoni effect, a convective fluidic phenomena. The Marangoni effect is explored and analyzed both theoretically and experimentally. An experimental set-up is designed and constructed in this purpose. These studies show the advantages of the proposed approach for high speed manipulation of micro-components in different sizes and geometries. The manipulation set-up is also entirely automated in order to show the parallel manipulation capabilities of this novel assembly technique.

The first chapter gives an overview of contactless manipulation techniques at microscale, such as optical tweezers, electric field, dielectrophoresis, acoustic waves and thermal motion based techniques. A comparison of the techniques points Marangoni effect as a viable solution.

The second chapter deals with the theoretical analysis of two convection phenomena: free convection and Bénard-Marangoni convection. This through a multi-physics finite elements based modeling. The governing equations for these phenomena are presented based on the fluid dynamics laws. A Proposed model is applied on a simple case of natural convection for initial analysis. Several simulations and their experimental validations are presented. Different parameters are analyzed such as water depth, temperature distribution and velocity field. Finally, a comparison between these phenomena is presented to know which mechanism predominates and is more suitable in our case. The Marangoni effect is presented as a promising method to drag micro-objects immersed in liquid media using only an IR laser beam as a heat source. This analysis allowed us to define the parameters for a conception of an experimental set-up for non-contact manipulation.

The third chapter describes the design of this above mentioned robotic platform. This platform is composed of several components: an optical microscope, a laser source as local thermal source, a scanner to address the laser with precision and other electronics. A vision system, using a high speed camera is also implemented. A calibration of this vision system is established in order to define the available precision of the overall system, dimensions and measurable velocities of manipulated parts by experimental analysis. This approach also allows to measure instantaneous acceleration values and leads to the estimation of the force applied to manipulated objects.

The fourth chapter deals with the automation of the manipulation process. The aim is to show that the proposed system is able to displace several microparts to predefined positions without user interaction. Particularly, the control of the Marangoni effect through the control of the position of the local heat source is demonstrated. The motion of this local thermal source is supplied by reflecting a laser beam on a mirror controlled by a high speed scanner. The implemented automation allows for a real time and high speed control hence it is possible to act simultaneously on several parts. The control loop is closed with vision feedback which is able to track at high frequency and sufficient precision all the involved parts at different form and dimensions. An experimental validation of parallel manipulation is describes and shows the originality of the proposed approach.

Chapter 1

Non-contact micromanipulation

The miniaturization of integrated devices with broad functionalities requires the development of new technologies that can overcome the conventional challenges in cost-effective assembly with high precision and speed. Two manufacturing routes form the basis for all miniaturization processes.

The first one is based on the continuous miniaturization and adaptation of technologies developed for larger scales systems. This method has been popularized under the name as "top-down". Due to the ever increasing difficulties raised by adhesion forces and the components dimensions, the applications of this approach is limited to the sub-millimeter range.

The second route, commonly called as "bottom-up", is based on the self-assembly of complex structures from atoms and molecules. While the method is appealing from its similarity to natural processes, our current knowledge of molecular synthesis does not allow us to fabricate components bigger than a few tenth of nanometers. It is often simpler to fabricate components with sizes in the range 0.1-1mm than it is to synthesize molecules. The bottom-up method still presents formidable challenges that make the production of complete systems based on molecular self-assembly a longer term objective for scales above 0.1 mm.

Both approaches are illustrated in Figure 1.1.

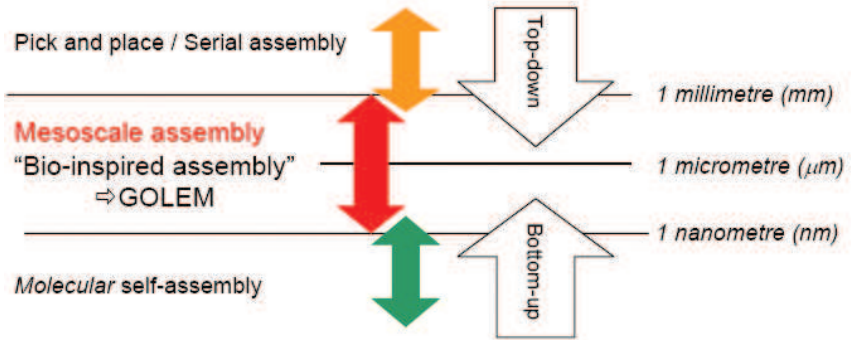

Figure 1.1: Assembly at all-scales.

Systems based on components with the size ranging from 1 μm to 100 μm -the mesoscale- cannot be efficiently produced and neither the "top-down" nor "the bottom-up" methods offer a complete answer to the problem. On the other hand, there are already various demands for such mesoscale systems. Examples are numerous and we only mention a few among them:

- In the hybrid electronic industry, components with sizes well below the millimeter are now readily available and yet find limited applications because of handling difficulties.
- Millimeter and sub-millimeter implantable diagnostic devices and implantable drug-delivery devices would be extremely beneficial for future therapies.
- Haptic devices like artificial skins with a massive amount of sub-millimeter sensors are new interfaces desired by Information Technologies.

The fabrication of mesoscale systems is not only an interesting scientific challenge but can also allow the development of high-impact and high-value products.
Therefore, there are needs for the methods which can manipulate mesoscale objects and components. A large amount of research is underway in this field, searching for flexible and versatile mesoscale manipulation methods that can be used for a high-throughput and cost-effective production in the hybrid electronic, microsystem and biomedical industries.
Such applications are beyond the limits of pick-and-place methods, such as microgrippers (Millet et al., 2004) and cantilevers (Haliyo et al., 2006), because at this scale they become too time-consuming. There are also significant difficulties for manipulation due to the dominant effect of surface forces and there is a high risk of sample contamination.

In the microworld, adhesive or surface forces such as electrostatic forces have a significant effect on the prehension task. Standard prehension strategies in the microworld must be adapted to the behaviors of micro-objects. Whereas on conventional scales, the most difficult phase of prehension is undoubtedly the gripping phase, in the microworld the release phase is particularly sensitive to adhesion. Thus when an attempt is made to release a micro-object from a gripper, the object remains stuck to the gripper, since its weight is not enough to overcome the adhesive forces. The prehension function must consequently be redesigned for such manipulation tasks. This has led to two main approaches, which can either exploit physical phenomena specific to the microworld or minimize such effects.

Alternate ways of prehension strategies can be expressed in the following two classes:

- contact-free solutions such as optical tweezers, dielectrophoretic systems or magnetic tweezers, which have the advantage that there is never direct contact between the effector and the object. This eliminates adhesive effects. The achievable blocking forces on the micro-objects are however weak, and these processes are often limited to a restricted class of materials, in terms of shape and physical properties;
- contact prehension solutions such as capillary prehensors, gel prehensors, microgrippers or adhesive prehensors are capable of manipulating micro-objects made from a wide range of materials and shapes. They are also capable of producing considerable forces, which can for example be useful during insertion operations for microassembly. These methods generally suffer from adhesive effects, and innovative release strategies must be developed in order to ensure a controlled and precise release of the object.

Non-contact methods are more suitable for fast and parallel manipulation tasks and a number of methods are being investigated using different types of driving forces, such as optical tweezers

(Arai *et al.*, 2004, Curtis *et al.*, 2002), electric fields (Moesner & Higuchi, 1997), (Chiou *et al.*, 2005) and magnetic fields (Assi *et al.*, 2002). Each of these methods is limited to specific types of objects, in terms of shape and physical properties. For example, to achieve precise manipulation using optical tweezers the object being moved must be transparent to the specific wavelength of the laser and have a spherical shape; when using dielectrophoresis techniques, the particles need to be dielectric or conductive.

The European project GOLEM[1] aims to achieve better assembly process for meso-scale objects using bio-inspired self assembly technologies. These objects can be of any kind of shapes, materials and sizes ranging from few μm up to several hundreds of μm. One of the key issues is to be able to move these micro-parts in a liquid medium independently of their composition. The manipulation methods described above are not suitable to the project as they put to much restriction in the type of object to be handled.

A much more interesting way is to move particles via the drag force of a liquid current or trapped into a liquid droplet. The actuation is in this case no more directly applied on the object but on the fluid around it. A recent and promising method is microfluidic actuation by modulation of surface stresses (Kataoka & Troian, 1999; Darhuber & Troian, 2005). In this case, fluid motion is driven by altering the surface tension at the fluid interfaces. Droplet manipulation using this technology is now a broad area of research. It has been investigated within the project GOLEM and is described further in this chapter.

Basu & Gianchandani, 2007 demonstrated micromanipulation with localized fluid actuation by shaping thermocapillary flow, or Marangoni flow, in thin, free surface liquid layers. This flow is driven by a temperature perturbation of surface tension using a micro heat source positioned above the liquid-air interface (free surface). Toroidal flows can be shaped which are centered at the heat source position. With this method, suspended microparticles of up to 30 μm in size and water droplets in oil can be manipulated without the need of microfabricated structures on substrates (Basu & Gianchandani, 2008).

Following the same principles, we have investigated the possibility to transport underwater micro-components using convection flow induced in a thin liquid layer by a focused 1480 nm infrared (IR) laser light. The generated flow is shaped as toroidal and centered at the focal point of the laser, allowing heavy and random-shaped mesoscale objects to be dragged. The flow drags these objects, which are totally immersed and in contact with the substrate, toward the focal point of laser. The principle of precise and controlled manipulation of single or multiple mesoscale objects on a non-patterned substrate was reported in (Vela *et al.*, 2008).

In this chapter, conventional non-contact approaches will be discussed. The different characteristics are summarized and compared.

1.1 Electric field driven effects

Electric fields are used for non-contact manipulation, transportation and separation of submicrometric particles suspended in aqueous media. There are four groups of electric fields methods that can be used for micromanipulation (Velev & Bhatt, 2006). Electrophoresis, where charged particles move toward the opposite sign of the electrode under constant (DC) electric field; DC electroosmosis, where fluid flows are produced by the motion of the counter-ions near the sur-

[1] http://www.golem-project.eu/

face between the electrodes; Dielectrophoresis, where a dielectric particle is attracted or repelled by the highest gradient of alternating (AC) field intensity; AC electro-hydrodynamics, where fluid flows are generated at the surface near the electrodes by the gradient of the AC field. In Figure 1.2 these four groups are shown.

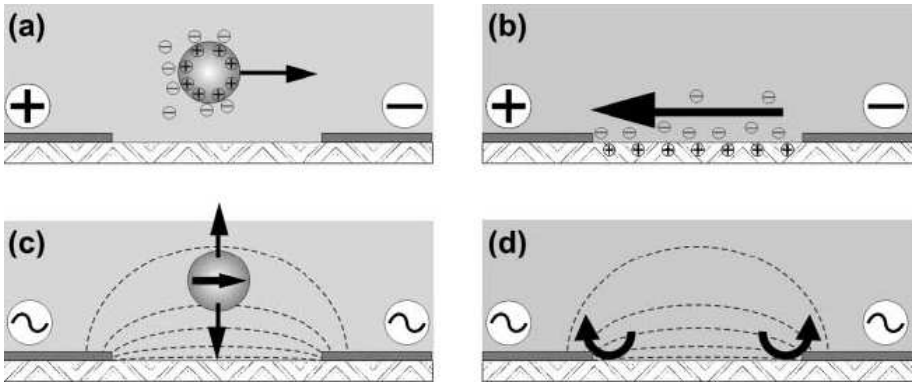

Figure 1.2: Electric field driven effects. (a) Electrophoresis. (b) DC electroosmosis. (c) Dielectrophoresis (d) AC electro-hydrodynamics.

From the methods mentioned above, the most used one for micromanipulation and assembly of micro and nanosized objects is dielectrophoresis. One drawback in using DC electric fields for manipulation of particles is the generation of electroosmosis: the ionic media develop a counterionic layer with the substrate. These ions move toward the oppositely charged electrode dragging the fluid. Thus, this fluid motion can drag the particles on arbitrary direction. For this reason, AC electrophoresis and dielectrophoresis (term introduced by Pohl, 1950) are more commonly used for separation and manipulation of microparticles.

1.2 Dielectrophoresis

AC field applied across particle suspended in liquid media generates dielectrophoretic (DEP) force. This allows precise control of the DEP forces exerted on the particles. However, the DEP force is not limited only to AC fields, however using DC field, the electric field magnitude is much smaller, making the DC dielectrophoresis impractical.

The force and torque may be approximated as (Jones, 2003):

$$\boldsymbol{F} \approx (\boldsymbol{p} \cdot \nabla)\boldsymbol{E} \tag{1.1a}$$

$$\boldsymbol{T} \approx \boldsymbol{p} \wedge \boldsymbol{E} \tag{1.1b}$$

where p is the vector moment of a small electric dipole and E is the electric field. By replacing the effective moment of the induced dipole in Eq. 1.1, the DEP force and torque are obtained (Jones, 2003):

$$\boldsymbol{F_{DEP}} = 2\pi R^3 \varepsilon_m \Re e[f_{CM}(\omega)] \nabla \boldsymbol{E}^2 \tag{1.2}$$

where R is the radius of a sphere, ε_m the dielectric permitivity of the media and $\Re e\,(f_{CM})$ is the real part of the Clasius-Mossotti factor. This factor is dependent of the angular frequency (ω) of the AC electric field. When the $\Re e(f_{CM}) > 0$, the particle is directed toward the highest electric field gradient, this attraction is called positive DEP (pDEP). The opposite effect is negative DEP (nDEP), when $\Re e(f_{CM}) < 0$ the particle is repelled from the regions of high electric

field gradient. Figure 1.3 depicts the principle of DEP and its comparison with electrophoresis.

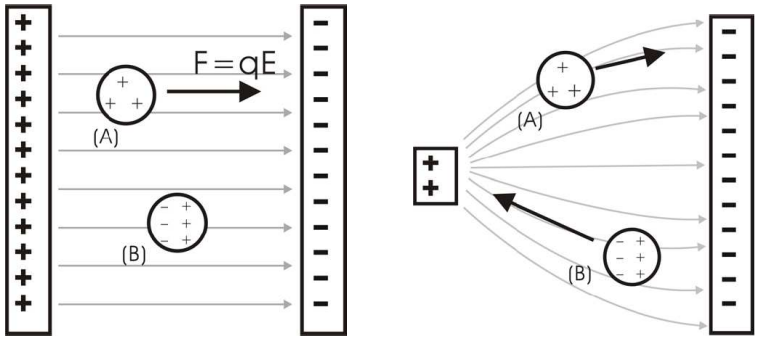

(a) Homogeneous field (b) Non-homogeneous field

Figure 1.3: Principle of dielectrophoresis

In the last 10 years, the use of DEP forces have drawn a great interest from the research and industry communities, especially in the applications in μTAS (micrototal-analysis-systems) technology. Besides, advances in microfabrication technology provides a wide variety of structure geometries, from simple planar to complex three-dimensional electrodes (Schnelle *et al.*, 2000). In this way, fully functional Lab-On-Chip (LOC) systems have been developed. Dielectrophoresis has been investigated and developed for transportation, separation (Suehiro *et al.*, 2003), (Abidin & Markx, 2005) and manipulation (Moesner & Higuchi, 1997),(Politano *et al.*, 1998) of biological and artificial micro-objects.

Hunt *et al.*, 2004 demonstrated the trapping and handling of yeast cells and polystyrene beads using positive and negative DEP. Their device was a post shaped microelectrodes array combined with a microfluidic channel, each post was 5 μm in diameter and 15 μm spaced center to center. The speed of a yeast cell (about 5 μm in diameter) from one post to another was of about 10 μms^{-1} for a 10 V and an ω of 10 MHz. Figure 1.4 shows the handling of a polystyrene bead (about 10 μm in diameter). The bead follows the minimum region of electric field (nDEP). By selectively energizing each post, the minimum region of electric field can be controlled. Thus, single and parallel addressable handling of micro-objects were performed.
Schnelle *et al.*, 2000 performed the trapping of latex beads (0,95 and 15 μm in diameter) in a 3D electrode cage (40 μm in height). For a bead 15 μm in diameter in a streamline fluid velocity of 100 μms^{-1} the critical escape voltage was of 2 V at 5 MHz (See Figure 1.5).

Many biological applications make use of dielectrophoresis. A summary of the methods used, which vary in the shape and number of electrodes, but also in terms of the nature of the objects being manipulated is given below.

Particle sorting, and in particular the sorting of biological cells, finds many applications in the field of medical research. The advantage of separating certain types of cells from an undifferentiated population is that researchers can perform more precise and better targeted studies. For example, the separation of cancerous and noncancerous cells to improve the tests of specific treatments for the disease.

Among existing sorting methods, it is worth mentioning the sorting of a population of biological cells using spiral electrodes (Figure 1.6). The different types of cells do not have the

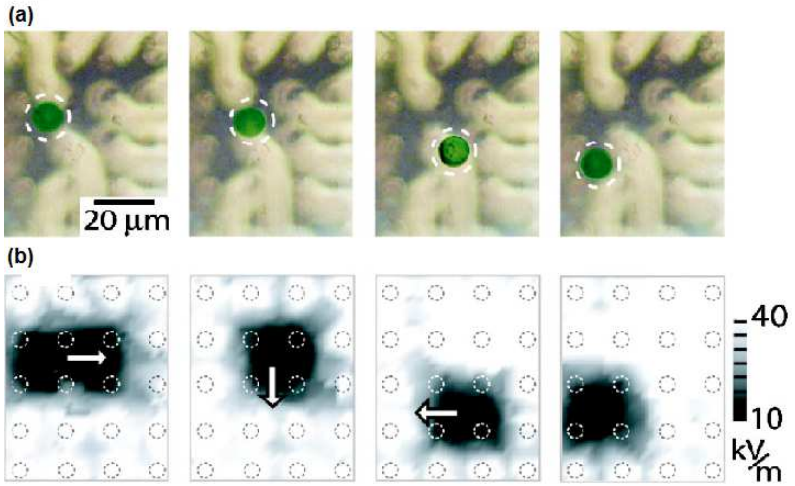

Figure 1.4: Trapping and manipulation of a polystyrene bead. (a) Bead follows the minimum region of electric field by selectively energizing the post shaped electrodes. (b) Simulations of the minimum region of electric field. The arrows indicate the direction of the trap motion.

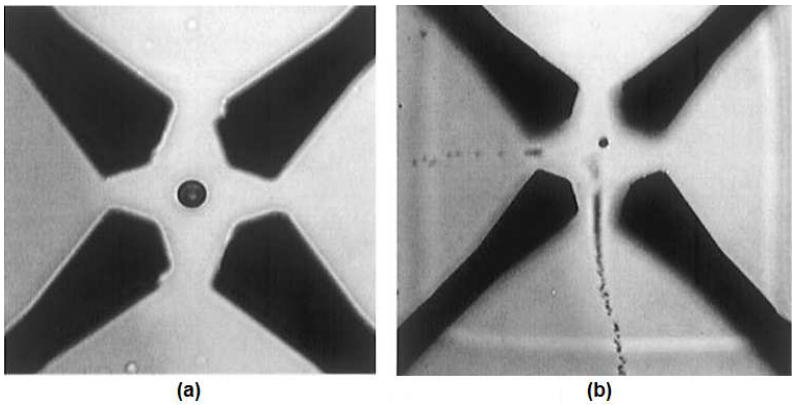

Figure 1.5: Trapping in an AC octode cage field. (a) Latex bead 15 μm in diameter. (b) Latex beads 0.954 μm in diameter.

same dielectric constant, and as a result the behavior of each population of cells is different. Thus an electrical signal with a specific frequency can be applied so that one part of the cells display negative dielectrophoresis and the other part a positive dielectrophoresis, enabling the two populations to be sorted (Becker *et al.*, 1999).

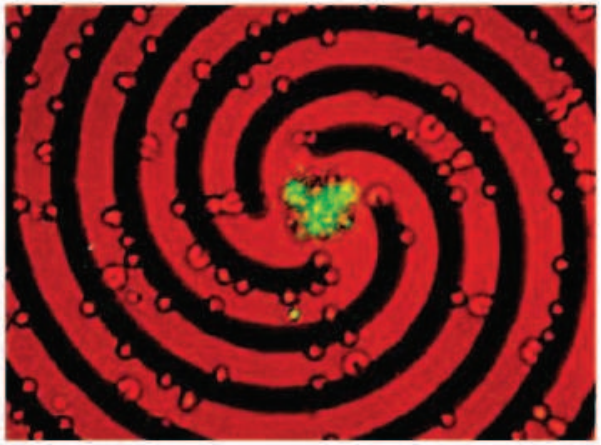

Figure 1.6: Spiral electrodes used for sorting of cells infected with malaria (in the center in green)

The use of the dielectrophoretic force can thus be used to separate cells into two populations. However, another method exists which combines microfluidics and DEP to enable the sorting into larger numbers of populations (Gascoyne & Vikoukal, 2004).

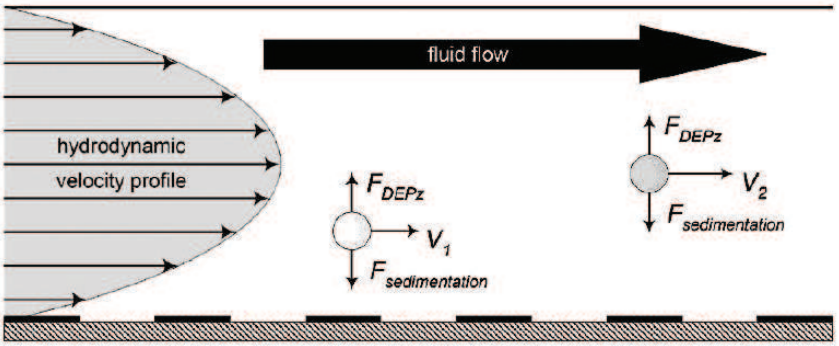

Figure 1.7: Sorting technique which combines dielectrophoresis and hydrodynamic forces.

A flux of particles (biological or artificial) in suspension in water travels along a microchannel etched onto one face of a network of electrodes that apply an electric field. The parabolic velocity profile established in the microchannel is used to sort the cells (see Figure 1.7). The altitude of each particle in the microchannel is given by the equilibrium between the dielectrophoretic force (assumed vertical) and the gravitational force. In this way, the cells that are subject to a large negative dielectrophoretic force are strongly repelled from the boundary of the microchannel and move into a region where the fluid velocity is large. The velocity in the flux of a population of particles depends directly on these electrical properties. This technique makes the sorting more selective and more practical, because the sorting takes place on a flux of particles rather than on particles within a stable medium (Figure 1.8).

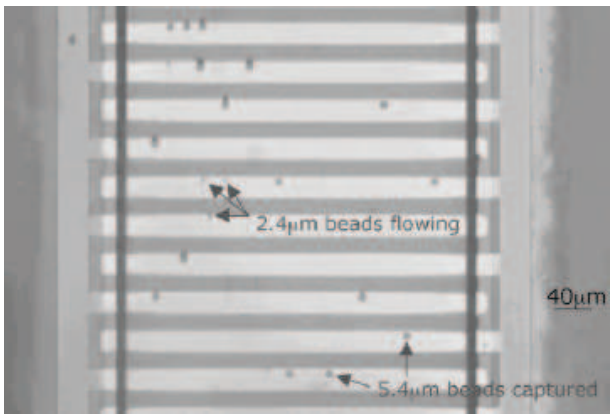

Figure 1.8: Particle sorting using a combination of dilectrophoresis and hydrodynamic forces.

Particle positioning using dielectrophoresis involves keeping a particle in a desired position defined by the applied electric field. Dielectrophoresis is able to produce a large enough force to confine a particle close to the electrodes.

Figure 1.9 shows an example of a device used for particle positioning. The electrode structure deposited onto a substrate includes square regions where the electrode coating is absent. It can be shown that the dielectrophoretic force will tend to position the beads at these sites (Figure 1.9). This technique can be used to select the material of the captured particle and to choose a maximum size of particle to be trapped. This system differs from earlier examples in that the aim is not to sort cells but to position them individually at precise locations (Frenea *et al.*, 2003, Rosenthal & Voldman, 2005) (Figure 1.9).

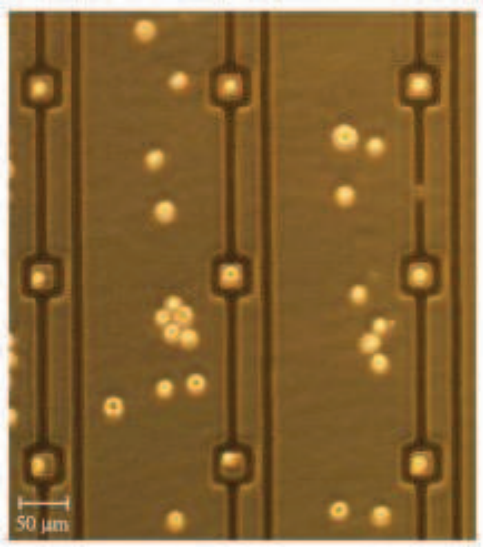

Figure 1.9: Capture of micro-objects above electrodes

The dielectrophoretic force has also been widely used for manipulating nano-objects such as carbon nanotubes (Seo *et al.*, 2005) (see Figure 1.10).

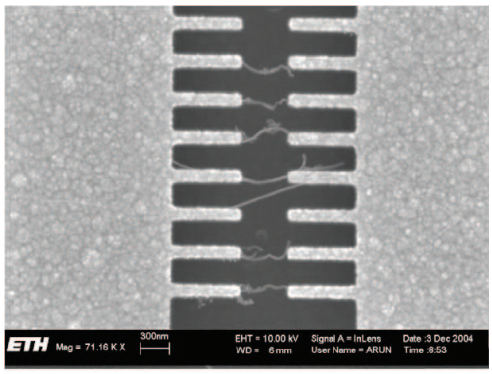

Figure 1.10: Use of dielectrophoresis in the nanomanipulation of carbon nanotubes

1.3 Optical tweezers

Since Ashkin demonstrated that it is possible to move or even levitate a dielectric bead by the radiation pressure of light (optical force) using a laser (Ashkin, 1970,Ashkin & Dziedzic, 1971), several teams have studied many techniques to use this principle for micro/nanomanipulation. A special interest is to handle and characterize biological objects such as cells (Goksör *et al.*, 2004), vesicles (Ashkin *et al.*, 1990), ADN (Chu, 1991). A recent work demonstrated the manipulation of hundreds of microparticles in parallel using holographic systems (Emiliani *et al.*, 2005).

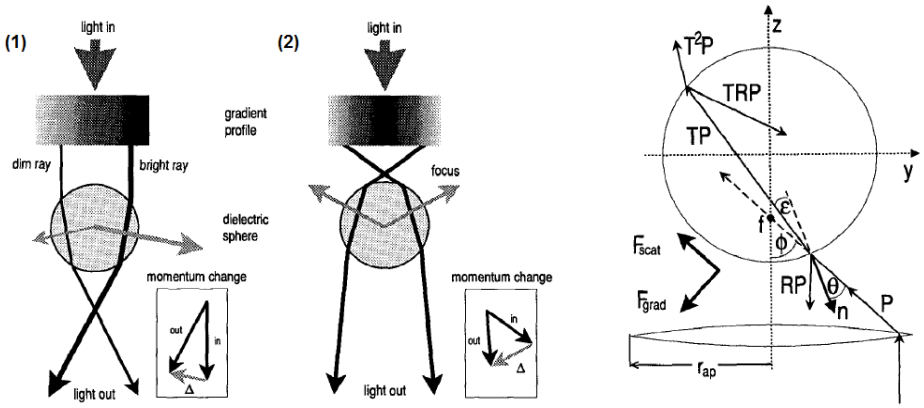

(a) (b)

Figure 1.11: Principle of optical forces. (a) Change of light momentum generating a force gradient. (a1) Gradient light profile directed to the right hand. (a2) Gradient light profile directed to the center. A vector diagram of the change of moment for the left and right ray is shown. (b) Diagram of the ray-optic theory. The axis of the scattering force is parallel to the beam and gradient force is perpendicular. R an T are the index of reflexion and refraction respectively, P is the laser power, θ the incident angle, ϵ the angle of refraction, φ the cone's half angle of the incident beam, $\mathbf{n}$ the normal vector surface, r_{ap} the aperture radius and f is the focus of the lens.

The basic explanation of this method is based on the variation of light momentum when light encounters a refracting object. So, when a laser is focused in such an object, a change in moment light is generated by the refraction of the light into the object. This produces gradient and scattering forces. The scattering force is directed along the ray beam and the gradient force

is directed toward the intensity gradient of the laser. The optical trap is produced with the gradient force, so for a stable trap the gradient force has to be greater than the scattering force. Figure 1.11a depicts this principle. (a1), the rays are refracted by the sphere generating change of moment, the brighter ray gives rise to a reaction force (gray arrow) greater than the dimmer left ray. The sum of this forces tend to pull the sphere toward the largest intensity of the laser. (a2), a parallel ray beam with a significant intensity gradient profile is refracted by a sphere, the change of moment generates reaction forces that pull the sphere upwards, toward the laser beam focal position.

The optical force can be defined as (Svoboda & Block, 1994):

$$F = \frac{Q\, n_m\, P}{c} \tag{1.3}$$

where Q is a dimensionless efficiency, n_m is the index of refraction of the medium, P is the incident laser power and c is the light velocity. Q represents the fraction of laser power used to exert force and is the main determinant of the trapping force. This factor depends on the coefficient of refraction, frequency of the laser, numerical aperture (NA) of the objective, laser mode structure and geometry of the particle.
There are three regimes for computing optical forces, the Rayleigh regime ($\lambda >> r$), intermediate regime ($r \leq \lambda \approx 1\,\mu m$) and Mie regime ($\lambda << r$), where r is the radius of the specimen and λ is the wavelength of the laser. In Figure 1.11b a diagram of the ray-optic theory developed by Ashkin for the Mie regime (Ashkin, 1992) is shown.

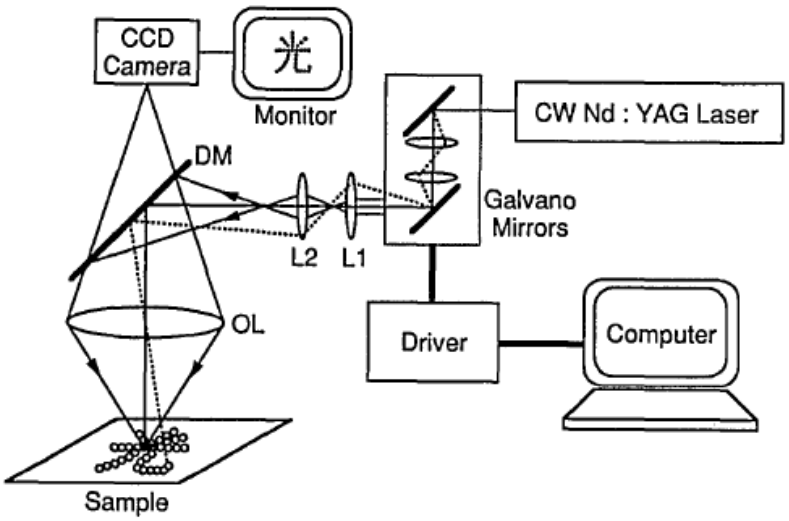

Figure 1.12: Optical tweezers setup.

In the last years, several laboratories have investigated and developed different apparatus to exploit this method. In Figure 1.12 a typical laser trapping system is sketched; this sort of system is called optical tweezers, a term referred to a single beam laser trapping. (Sasaki *et al.*, 1991) performed the manipulation of latex beads 2 μm in diameter by scanning the laser with galvanometric scanners. Thus, any type of pattern (cf. Figure. 1.13a) could be formed and moved. For instance, a circular pattern ($\sim$13.5 μm in diameter) was moved at a speed of $\sim$12.2 μm/s, scanning repetition rate of 15 Hz and applied laser power of 120 mW.

Improvements of control and manipulation of multiple microbeads for a single laser beam were demonstrated by Arai *et al.*, 2004. The microbeads not only could form a pattern but they could be manipulated independently by a synchronized laser. In Figure 1.13b, the manipulation of six polystyrene spheres (7 μm in diameter) are shown. The laser scanning is performed by galvanometer mirrors with a time of change of mirror positions of 1 ms to keep a stable manipulation. The laser irradiation time was 63.8 ms.

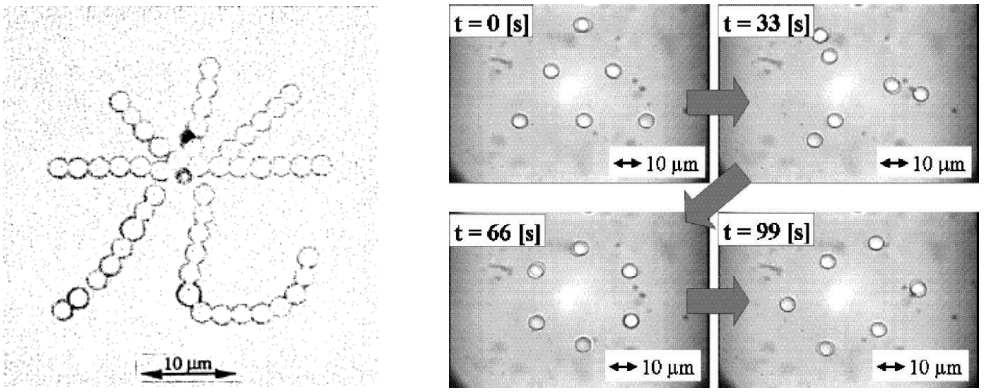

(a) Scanning laser manipulation (b) Synchronized laser manipulation

Figure 1.13: Manipulation of micro spherical beads by optical tweezers

Future directions to analyze and manipulate biological objects are on chip μTAS. Therefore, optical tweezers are suitable for on chip micromanipulation. (Boer *et al.*, 2007) demonstrated the manipulation of microbeads by optical tweezers in a microfluidic chip. It aims at analyzing biological objects within different flow reaction solutions in the same chip (microchannel of 250 x 30 μm^2 in cross section). Thus, polystyrene beads of 2 and 5 μm in diameter were trapped and moved across three different solution flows, obtaining for a 2 μm bead a force of 16 pN at a flow speed of 800 μm/s.

Various commercial devices are available for manipulating objects, such as the LaserTweezer(R) system available from the company Cell Robotics International, Palm Microlaser Systems from the company PALM MicroLaser Technologies as well as the Optical Tweezer system from the company Elliot Scientific. In this industrial landscape the product BioRyx 200 from the company Arryx, Inc. stands out because of its use of the HOT technique which allows to manipulate 200 particles in parallel (Grier & Lopes, 2007). Forces involved are of the order of a few piconewtons for objects with diameters of the order of a micrometer (Emiliani *et al.*, 2004, Nambiar *et al.*, 2004).

This principle can be used to manipulate a wide variety of micro-objects such as artificial spheres, biological objects or nano-objects such as carbon nanotubes (Agarwal *et al.*, 2005). Direct bio-manipulation where the beam is focused on a biological object can lead to damage. One solution to this problem when moving biological cells is to move them in an indirect manner, by pushing them with the help of a tool which is itself moved using the optical tweezers (Arai *et al.*, 2006).

Optical tweezers are used for microassembly applications (Holmlin *et al.*, 2000). The cells are initially bound to polystyrene beads 3 μm in diameter, using suitable molecular structures. They are then moved using optical tweezers by focusing the laser beam onto the polystyrene

beads. The polystyrene bead is brought into contact with a nearby cell, producing molecular bonding. The structure shown in Figure 1.14 can be produced using this technique.

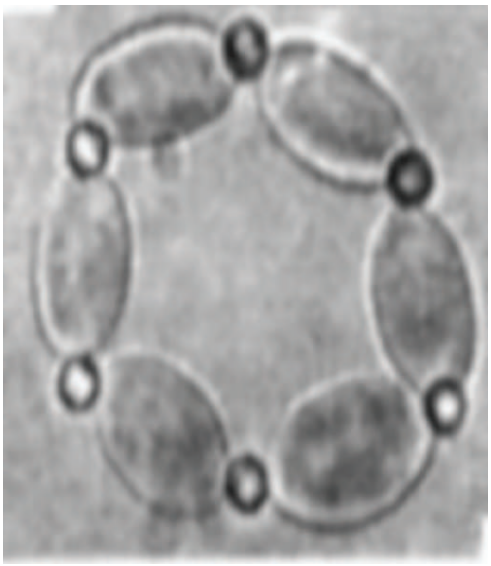

Figure 1.14: Microassembly of cells and polystyrene beads with the help of optical tweezers.

1.4 Electrowetting

This recent method is based on variation of surface tension of a polarizable and conductive liquid droplet by applying an electric field at one its edges. For this, the droplet has to be kept between two plates (sandwiched), one plate grounded and the other containing the control electrode array, the both plates forming capacitances. When an electric field is set, the charges at the surface of the droplet accumulate upon the electrode and thus diminishing the surface tension. The generated surface tension gradient drives the motion of the droplets toward the side of the active electrode (Ren *et al.*, 2002) (see Figure. 1.15a). To ensure the motion, the droplets have to be in the same size of the electrode pitch.
(Pollack *et al.*, 2000) performed the manipulation of discrete microdroplets of 100 mM KCl ranging from 0.7 - 1 μl (about 620 μm in diameter). The top plate provided a gap between the opposing electrodes of 300 μm, thus obtaining a droplet velocity of 30 $\mathrm{mm\,s^{-1}}$ for 80 V (Fig. 1.15b).

1.5 Magnetic manipulation

With the magnetic method, only the manipulation of magnetic or paramagnetic beads is possible. So, for the manipulation of biological parts using magnetic forces, functionalization of paramagnetic beads with antibodies, peptides or lectins is required so that molecules or cells can attach to beads.
The magnetic force produced on a paramagnetic bead is dependent on the induced magnetic moment of the bead and the magnetic field applied as follows:

$$\boldsymbol{F_m} = \boldsymbol{m} \cdot \nabla \boldsymbol{B}, \tag{1.4}$$

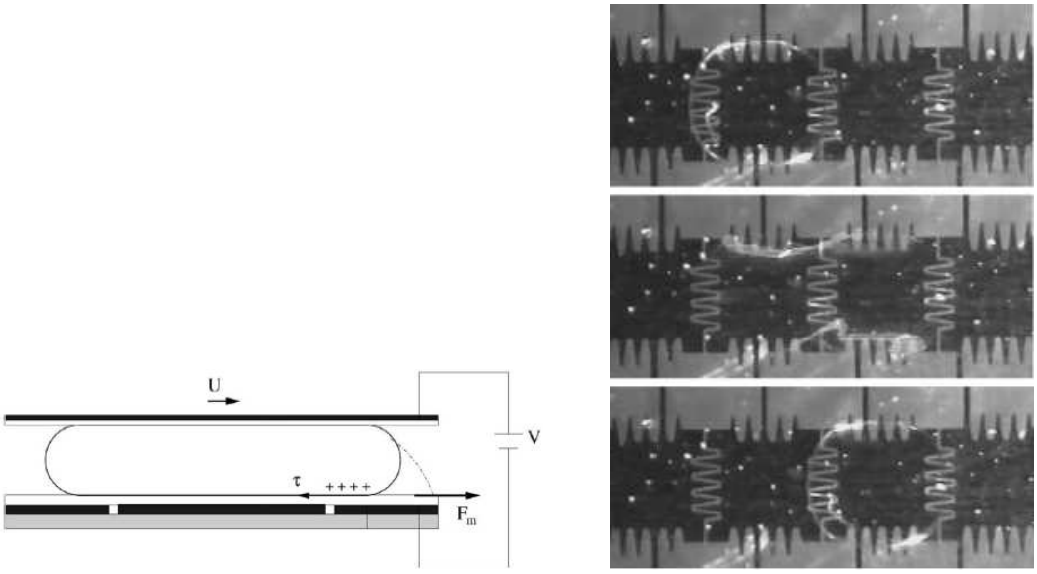

(a) (b)

Figure 1.15: Electrowetting on insulator (EWOD). (a) Principle of the EWOD, droplet sandwiched between insulator layers deposited on both electrode plates, the insulators decrease the wettability. A surface tension gradient is electrically generated for driven the droplet toward the active electrode. V is the voltage, U is the average transport velocity, τ is the surface tension and F_m is the electrostatic driven force per unit length. (b) snapshots of a moving droplet at 33 ms intervals. A 80 V potential is applied to the right electrode and droplet follows.

where $\boldsymbol{m}$ is the induced magnetic moment of the bead and $\boldsymbol{B}$ is the magnetic field. In addition, the magnetic moment is proportional to the external magnetic field $\boldsymbol{B}$, $\boldsymbol{m} = V\chi\boldsymbol{B}/\mu_0$, where V is the volume of the bead, χ is the magnetic susceptibility of the bead and μ_0 is the permeability in a vacuum.

(Lee *et al.*, 2004) developed an electromagnet matrix device to transport paramagnetic beads (2.8 μm in diameter) with yeast cells (6 μm in diameter) attached to them. The matrix consisted of 10 x 10 Au wires of 4 μm in width and spaced of 8 μm. Thereby, the objects were moved with micrometric resolution and forces of 40 pN and B of 10 mT. Figure 1.16 illustrates these results.
The manipulation of Deoxyribose Neucleic Acid (DNA) is also possible with this technique, by attaching them on the surface of a paramagnetic bead their bond characteristics can be studied, either with single (Yan *et al.*, 2004) or multiple DNA molecules. (Assi *et al.*, 2002) performed the manipulation of multiple DNA molecules attached to beads using a permanent magnet. The magnet was suspended above a microfluidic channel containing the sample (solution of DNA and functionalized beads). By varying the position of the magnet with an x-y-z stage, the DNA molecules were handled. The forces were in the range of 0.1 to 200 pN for 0 to 8 mm distance between the magnet and the microchannel.

This technique is mostly used for cell sorting. Since the cells are only very slightly sensitive to magnetic fields, the magnetic force applied directly to the cells is very weak and may not be enough to produce a displacement. The most commonly-used method involves moving the cells using magnetic energy, and hence requires them to be fixed to objects that are sensitive to the magnetic field.

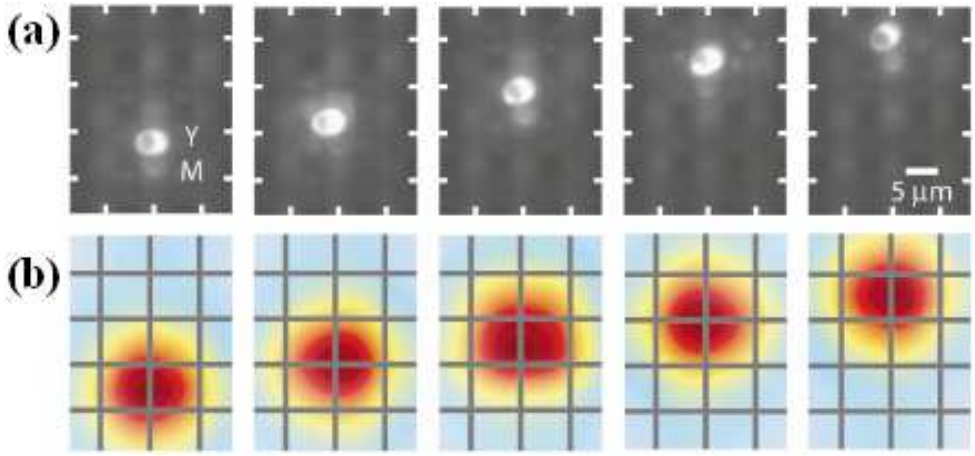

Figure 1.16: Magnetic manipulation. (a) Sequence of images showing the transport of a yeast cell by changing in steps the localized magnetic field controlled by currents in the wires. Y is yeast cell and M is magnetic bead. (b) Simulations of the magnetic field peak at the yeast position within the wire matrix.

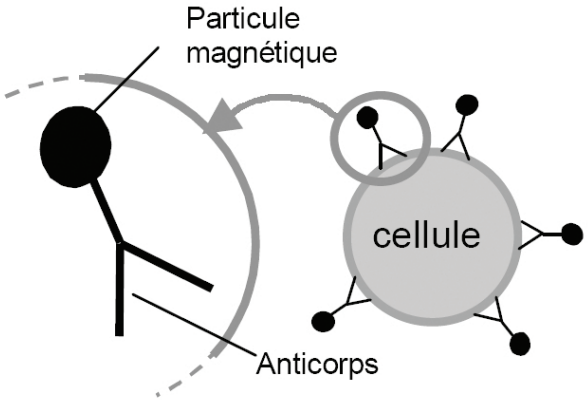

Figure 1.17: Principle of magnetic sorting of cells.

In another work, small paramagnetic, diamagnetic or ferromagnetic particles (1500-50 nm in diameter (Kemshead & Ugelstad, 1985)) are attached to antibodies (see Figure 1.17). Antibodies and their magnetic companions are introduced into the sample to be analyzed. They attach themselves to the target cells, which can then be manipulated using magnetic energy. Since the cells without companions are virtually insensitive to the magnetic field (Kemshead & Ugelstad, 1985), it is possible to use a magnetic field to separate the target cells from the rest of the population.

Recently, investigations have been carried out into optimizing the structure of the system that produces the magnetic gradient required to produce the magnetic force. These have enabled a considerable increase in the forces that can be applied. It is thus now possible to directly manipulate cells, and to sort them as a function of their intrinsic magnetic properties, without the addition of extra particles (Furlani, 2007, Zborowski *et al.*, 2003) (see Figure 1.18).

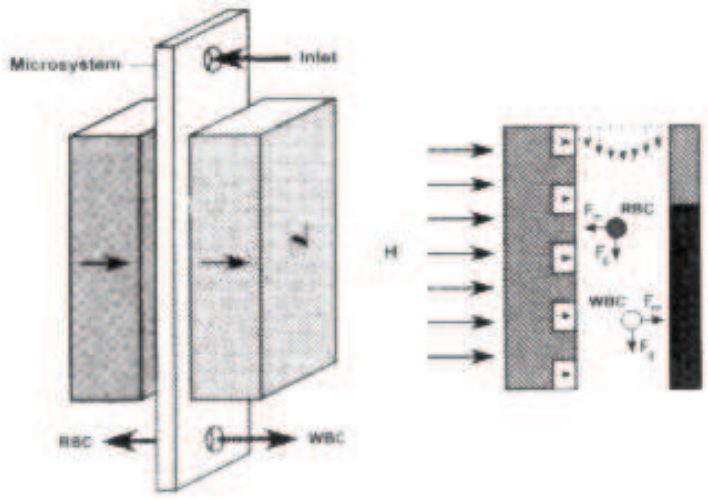

Figure 1.18: Principle of cell sorting by magnetophoresis (Furlani, 2007).

1.6 Acoustic waves

Another method to manipulate and pattern micro-parts in a parallel and massive manner is using standing acoustic waves (Shi *et al.*, 2009; Haake & Dual, 2002). One advantage of this method is the handling of micro-particles regardless of their optical or electrical properties.
The micro-parts are moved and manipulated by the propagation of acoustic waves in a substrate. The particles are in a liquid medium over the substrate. The interaction between these acoustic waves and the liquid medium causes the particles to move.
Two propagation modes are used with acoustic waves: surface acoustic waves (SAW)(Shi *et al.*, 2009) and bulk acoustic waves (BAW)(Manneberg *et al.*, 2009; Petersson *et al.*, 2007).

As an example, the working principle of SAW is presented because it is more interesting in terms of miniaturisation in comparison to BAW.
Shi *et al.*, 2009 developed an acoustic system based on standing SAW (SSAW). It is composed of a microfluidic channel on a piezoelectric substrate. On the substrate interdigital transducers (IDTs) are deposited in order to generate SSAW (see Figure 1.19a). When the SSAW interacts with the liquid medium, a longitudinal-mode leakage waves is engendered. This leads to acoustic radiation forces that act on the suspended particle to move them into the regions of minimum pressure amplitudes or nodes in the SSAW field.

The primary acoustic force exerted on the object can be expressed as:

$$F = -(\pi p^2 V_{ob} \beta_m / 2\lambda) \phi(\beta, \rho) sin(2kx),$$

$$\phi(\beta, \rho) = \frac{5\rho_{ob} - 2\rho_m}{2\rho_{ob} + \rho_m} - \frac{\beta_{ob}}{\beta_m},$$

where p, λ, V_{ob} are the acoustic pressure, wavelength and volume of the object, respectively; $\rho_{ob}, \rho_m, \beta_{ob}, \beta_m$ are the density of the object and the medium, compressibility of the object and medium, respectively. $\phi(\beta, \rho)$ determines the balanced positions of the objects: if $\phi(\beta, \rho) > 0$, the objects will aggregate at pressure nodes, and vice versa.

Figure 1.19b shows the manipulation of fluorescent polystyrene beads. The arrangement of beads in three rows is performed using the 1D mode and the beads are placed in a matrix using

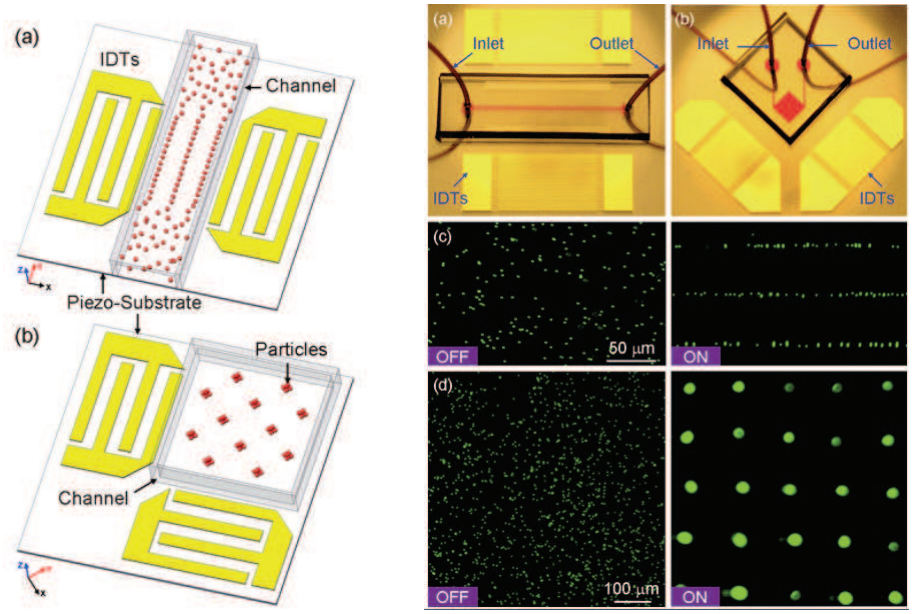

(a) (b)

Figure 1.19: Manipulation of fluorescent polystyrene beads of 1.9 μm in diameter. (a:a) Concept for 1D acoustic system. (a:b) 2D acoustic system. (b:a) 1D acoustic system. (b:b) Perpendicular arrangement of IDTs for 2D manipulation. (b:c) 1D arrangement of beads. (b:d) 2D arrangement of beads.

the 2D mode.

1.7 Manipulation via actuated flows

Recently, different modes to drive flows are drawing a great interest in the scientific community. A great advantage is the generation of localized fluid motion to drag microparts to analyze and perform self-assembly in a non-contact manner. To generate flow motion, methods such as electroosmosis, electrohydrodynamics, micromechanical and thermocapillary pumping (Burns *et al.*, 1996) are used. Most of these methods require microfabrication of fluidic channels and kilovolt sources. Therefore, a much more suitable method is the use of thermocapillary effect, where fluid motion is generated by variation of surface tension at the interface of two immiscible fluids (most commonly air-water and oil-water interface). Surface tension being dependent of the temperature, a variation of temperature causes a surface tension gradient. For pure liquids, surface tension decreases as temperature increases. Hereby, the cold regions pull the fluid from the hot ones due to the shear stress applied by the surface tension gradient. Here the surface stress is defined as follows: $\tau = \partial\sigma/\partial r$, where τ is the surface shear and σ is the surface tension.

The control of surface tension is a natural approach to drive flows because at the microscale, the surface to volume forces ratio is large. Several microfluidic apparatus have been developed to manipulate microparts in fluids or droplets as object carriers and reaction sites for chemical substances.

(Farahi *et al.*, 2004) realized a device to transport droplets in the range of pico/nanoliters. In Figure 1.20 the setup and image results are shown. As seen in Figure 1.20b, an oil droplet

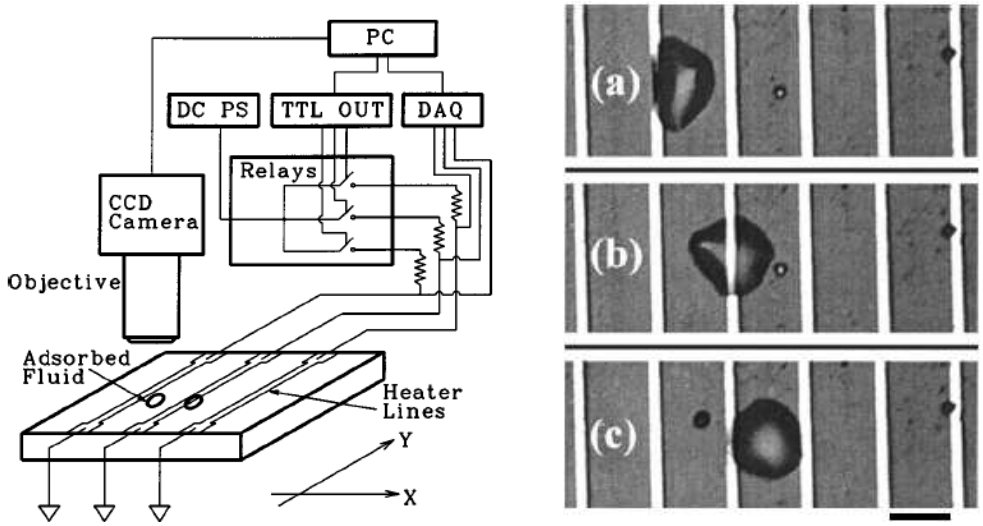

Figure 1.20: Droplet manipulation in one degree of freedom. (a) Apparatus of the fluidic manipulation. (b) Snapshots of the oil droplet displacement. Scale bar 100 μm

100 μm in diameter is moved from one metallic line to another at a speed of 1.5 mm s^{-1}. A pulse of 20 V, 300 mA, and 10 ms width was required.

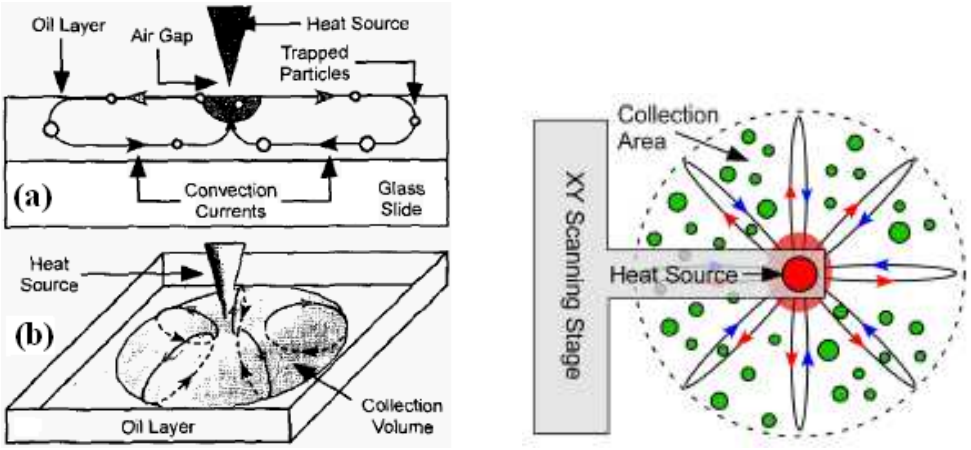

Figure 1.21: Device concept

Marangoni effect

An interesting technique for trapping and collecting micron-sized particles using Marangoni flows was developed by Basu (Basu & Gianchandani, 2005). By heating locally a thin layer (50 - 400 μm) of oil or water at the free surface, convective flows are generated due to the variation in the surface tension. This flow has toroidal and doublet shapes (Basu & Gianchandani, 2007) for oil and water layers respectively. Toroidal flow is in the volume of the oil layer, on the other hand doublet flow is at the surface of the water layer. Figure 1.21 illustrates the operating principle of the device. A micromachined tip (heat source) heats the air-surface interface generating

Marangoni flow, where the particles are trapped or collected in the toroidal currents as shown in Figure. 1.21a. The tip can be moved over the sample by a scanning stage, thus a 2D manipulation is performed. The toroidal radius depends on the thickness of the liquid layer. Thereby, very localized trapping regions are possible (∼80 μm in radius - ∼150 μm in thickness and ∼380 μm in radius - ∼1100 μm in thickness). Figure. 1.21b sketches the collection area beneath the tip where the torus is centered. The velocity of the flow depends primarily on fluid temperature which can be controlled by the input power applied to the tip. For 140 μm of oil thickness, the speed of flows is about 1500 μm/s (with 18 mW input power and 30 μm gap between the tip and oil surface). With this technique, the trapping of weed pollen 25 μm in diameter and water droplets with radii ranging from 5 - 100 μm were performed.

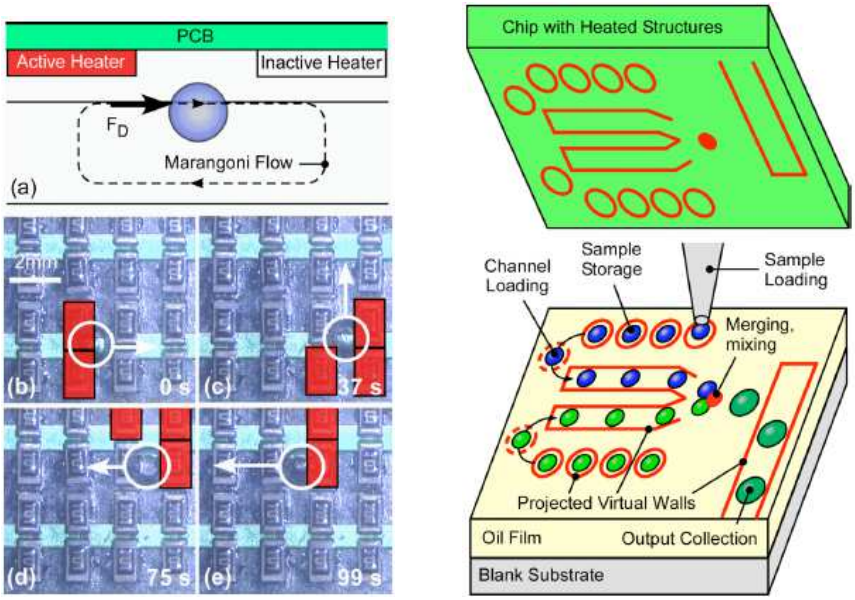

(a) (b)

Figure 1.22: Microfluidic platforms

(Basu *et al.*, 2007) proposed a microfluidic platform based on an array of microheaters suspended above an oil layer (see Figure 1.22). By activating independently each microheater, almost any sort of thermal patterns can be produced and projected over the oil surface. Thus, droplets of water in the range of 300 - 1000 μm in diameter can be manipulated by creating size-selective filters, traps, channels and pumps. For instance, a speed of about 1700 μm/s was obtained using 25 μm pollens and a speed of 140 μm/s for a water droplet of 600 μm in diameter. The liquid medium was a high density oil (specific gravity of 1.07, Dow Corning 550 Fluid). Figure. 1.22a shows the heater arrays pushing away a 900 μm droplet in diameter in a square trajectory by activating the heaters sequentially. The active heaters are highlighted with rectangles drawn on the picture. In Figure. 1.22b, a thermal pattern example is sketched, thereby a complex microfluidic system without micromachined elements may be achieved.

1.8 Summary

The following table gives a comparative summary of various non-contact micromanipulation methods.

Table 1.1: Comparisons of non-contact micromanipulation methods

	Method	Characteristic of micro-part	Force	Speed	Resolution	Comments
1	Dielectrophoresis	Conductive or dielectric		10 μm/s	low	Patterned substrates
2	Optical tweezers	Close to a spherical shape Transparent to a laser light up to 20-30 μm in size	up to 20 pN	12 μm/s (Sasaki *et al.*, 1991)	high	Depend also on the index of refraction media Radiation pressure damage
3	Electrowetting	Droplets		30 mm/s (Hunt *et al.*, 2004)	low	Patterned substrate
4	Magnetic tweezers	Magnetic properties	no limit		low	External magnetic field
5	Acoustic waves	Any shape and composition	25 pN	μm/s range (Shi *et al.*, 2009)	low	No single handling
6	Thermocapillary	Droplets		1.5 mm/s (Farahi *et al.*, 2004)	low	Patterned substrate Temperature damage
7	Marangoni flows	Any shape and composition	100s to nN up to 300 μm in size	mm/s range (Vela *et al.*, 2009)	high	Thermal damage Single and Parallel handling Depend on the liquid depth Free surface

1.9 Conclusions

Micromanipulation methods can be classified into two classes: contact (mechanical) manipulation and non-contact manipulation.
The first one has handling difficulties due to adhesion forces that increase with the micro-parts size reduction. Such methods are time-consuming and not cost-effective for a high-throughput. On the other hand, non-contact methods are more suitable for handling micro-parts in the range of 0.1 - 100 μm in a parallel and massive manner in liquid media thus making possible cost-effective and high-throughput microdevice production.

In this chapter, an overview of different micromanipulation methods is given with a comparison of contact and non-contact techniques. These analysis points some advantages of contactless techniques, especially when the size and the shape of the objects may vary. Addion phtionally, contactless methods in liquid allow to minimize the effects of adhesion phenomena, which are the most dominant forces at this scale.
Among the liquid convectienomena, Marangoni effect stands out because of its ability to generate locally high-speed flows. The strength of these flows and their spatial distribution are enough to drag several micro-parts in parallel. Moreover, As this phenomenon is based on surface forces (proportional to L), it is more suitable for miniaturisation than free convection which is based on body forces (proportional to L^3). Their theoretical and experimental analysis is presented in chapter 2. This analysis shows that this method can be implemented by using a single laser beam as a heat source. The main advantage advantage of using a laser is that it can be focused in a very small surface, thus obtaining a very localized convection flows.

Chapter 2

Opto-fluidic actuation for non-contact micromanipulation

In this chapter, two phenomena based on opto-fluidic actuation are proposed and investigated to perform non-contact micromanipulation in liquid media. Working in liquid media allows to reduce or avoid significant problems encountered in micromanipulation in the air such as capillary or electrostatic forces.

Moreover, the ability of engineering microfluidic patterns in order to handle immersed microparts in a non-contact manner would be a very good approach to perform parallel or single manipulation such as the assembly of hybrid micro-components that are fabricated with batch processes, where liquid media are omnipresent.
For this purpose, only the light interactions with fluid can be used, allowing rapid and free of contamination manipulation through laser-induced convection flows.

The two phenomena studied are natural and Bénard-Marangoni convections. Both occur with the laser absorption of a liquid medium resulting in thermal heating.
The natural convection is established by the Archimedes force, which is a body force due to gravity, and the Bénard-Marangoni convection is imparted by changes in surface forces at a fluid-air interface.

Firstly, the fluid mechanics laws that govern these phenomena are given and dimensionless numbers are used to asses which mechanism predominates. Secondly, natural convection is studied using numerical simulations in order to know the temperature distribution and velocity field. Finally, Bénard-Marangoni convection is explained and compared to the natural convection for micromanipulation.

2.1 Theoretical background

The convection phenomena depend on fluid mechanics laws. In order to explain the fluid motion, the problem is theoretically analyzed with the fluid mechanics principles. Based on experimental data, hypothesis are proposed and dimensionless numbers are calculated. This allows to determine which phenomena predominates and simplify the fluid mechanics equations.

2.1.1 The fluid mechanics laws

In fluid dynamics, the measurable quantities of a fluid particle vary with time and coordinate. An operator $\frac{D}{Dt}$, the material derivative, is introduced:

$$\frac{D\psi}{Dt} = \frac{\partial\psi}{\partial t} + (\boldsymbol{u}\cdot\nabla)\psi, \tag{2.1}$$

where ψ is an arbitrary measurable fluid quantity. The first law of fluid mechanics is the mass conservation: in a small open volume ∂V of fluid, the mass is conserved regardless the movement inside it.

$$\frac{\partial\rho}{\partial t} + \nabla\cdot(\rho\boldsymbol{u}) = 0, \tag{2.2}$$

$$\frac{D\rho}{Dt} + \rho(\nabla\cdot\boldsymbol{u}) = 0, \tag{2.3}$$

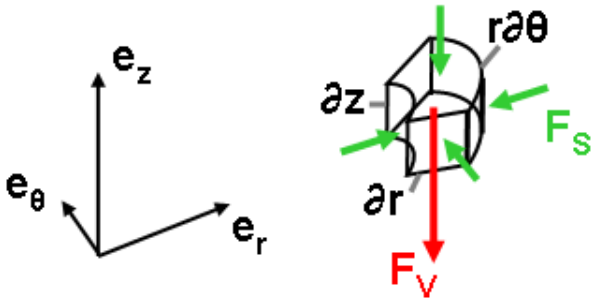

Figure 2.1: Fluid particle in cylindrical coordinates.

The second law is the momentum conservation or Navier-Stokes equation. It is the equivalent of the Newton first's law in fluidic systems (see Figure 2.1):

$$\frac{\partial(\rho\boldsymbol{u})}{\partial t} + (\boldsymbol{u}\cdot\boldsymbol{\nabla})(\rho\boldsymbol{u}) = \frac{\partial F}{\partial V} \tag{2.4}$$

$$\frac{D(\rho\boldsymbol{u})}{Dt} = \frac{\partial F_v}{\partial V} + \frac{\partial F_s}{\partial V} \tag{2.5}$$

To deal with temperature diffusion, the Fourier equation is used:

$$\frac{DT}{Dt} = \kappa\nabla^2 T + Q_l \tag{2.6}$$

where κ is the thermal diffusivity and Q_l is the volumetric heat flux due to an internal heat source.

The volumetric heat flux Q_l

The absorption of a laser beam is used as a heat source. The light absorption equation states that the variation of intensity is proportional to the intensity at a determined position:

$$\nabla I(r,z) = -(\alpha)I(r,z), \tag{2.7}$$

where α is the absorption coefficient ($\alpha = 23.45/cm$ for a 1480 nm of wavelength). The intensity gradient is negative, which means that it decreases along the light path. This lost in the laser radiative energy is transformed in heat energy in the liquid. The intensity gradient is then directly the opposite of the volumetric heat flux. Considering a Gaussian shape of the laser intensity, the volumetric heat flux gives:

$$Q_l = \alpha I(r,z) = \alpha I_0 \left(\frac{w_0}{w(z)}\right)^2 \exp\left(\frac{-2r^2}{w^2(z)}\right) \tag{2.8}$$

where I_0 is the initial intensity of the beam, w_0 is the waist of the convergent laser beam, $w(z)$ is the radius at which the intensity drops to $1/e^2$ of its axial value. $w(z)$ expression is:

$$w(z) = w_0\sqrt{1 + \left(\frac{\lambda z}{\pi w_0^2}\right)^2}$$

where λ is the laser wavelength.

Figure 2.2 illustrates the system. The laser irradiates a thin liquid layer from below. It is focused at the bottom of the layer.

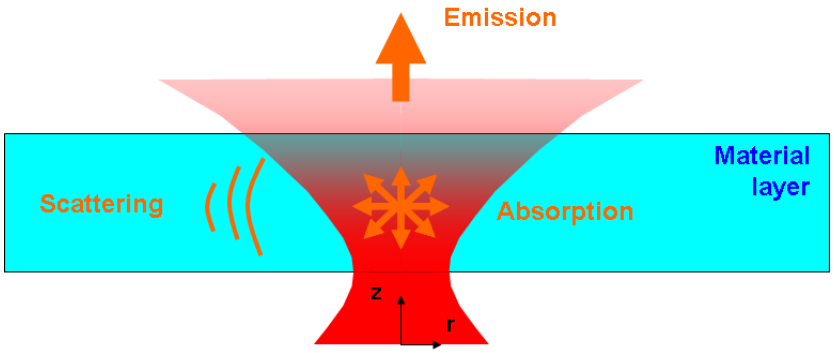

Figure 2.2: Laser absorption by a liquid layer

2.1.2 Hypothesis on the model

The system is a circular Petri dish with a thin layer of distilled water. A laser source is placed under this sample and lights the bottom of the Petri dish. The laser beam is focused by a microscope objective. Water has a good absorption rate at the chosen wavelength (1480 nm). Different hypothesis on this system are proposed:

1. The laser light force is negligible compared to the thermal effect. The only body force is the Archimedes force.

2. The distilled water may be considered as a Newtonian fluid.

3. The geometry of the problem is cylindrical, so the problem is independent of θ coordinate.

4. Only the permanent regime is considered.

As the stress forces density can be expressed by a tensor and considering hypothesis (1), the Navier-Stokes equation can be written as follows:

$$\frac{D(\rho \boldsymbol{u})}{Dt} = (\rho - \rho_0)\boldsymbol{g} + \boldsymbol{\nabla} \cdot \overline{\boldsymbol{\sigma}} \tag{2.9}$$

$\overline{\boldsymbol{\sigma}}$ is the total stress tensor that distinguishes two parts: an isotropic part $-p\delta_{ij}$, where p is the normal stress on surface, or the pressure, and a non-isotropic part. This second part is the deviatoric stress tensor, it contributes to the tangential stress and allows flow movements. Newtonian fluids have special properties with respect to the shear stress and give for $\overline{\boldsymbol{\sigma}}$:

$$\overline{\boldsymbol{\sigma}} = \sigma_{ij} = -p\delta_{ij} + 2\mu(e_{ij} - \frac{1}{3}e_{ii}\delta_{ij})$$

where $e_{ij} = \frac{1}{2}(\frac{\partial u_i}{\partial x_j} + \frac{\partial u_j}{\partial x_i})$ and μ is the dynamic viscosity. Thus, Eq. 2.9 gives:

$$\frac{D(\rho \boldsymbol{u})}{Dt} = (\rho - \rho_0)\boldsymbol{g} - \boldsymbol{\nabla} p + \boldsymbol{\nabla}(\mu \boldsymbol{\nabla} \cdot \boldsymbol{u}) \tag{2.10}$$

Hypothesis (3) and (4) allow to write the system of equations in cylindrical coordinates. Simplification due to motion absence in θ direction and the mass conservation is possible (Johnson, 1998).

$$\frac{1}{r}\frac{\partial r\rho u_r}{\partial r} + \frac{\partial \rho u_z}{\partial z} = 0 \tag{2.11}$$

$$\frac{1}{r}u_r\rho\frac{\partial r u_r}{\partial r} + u_z\rho\frac{\partial u_r}{\partial z} = -\frac{\partial p}{\partial r} + \frac{1}{r}\frac{\partial}{\partial r}(r\tau_{rr}) + \frac{\partial}{\partial z}(\tau_{zr}) \tag{2.12}$$

$$\frac{1}{r}u_r\rho\frac{\partial r u_z}{\partial r} + u_z\rho\frac{\partial u_z}{\partial z} = -(\rho - \rho_0)g - \frac{\partial p}{\partial z} + \frac{1}{r}\frac{\partial}{\partial r}(r\tau_{rz}) + \frac{\partial}{\partial z}(\tau_{zz}) \tag{2.13}$$

$$\frac{1}{r}\frac{r u_r \partial T}{\partial r} + \frac{u_z \partial T}{\partial z} = \kappa(\frac{\partial^2 T}{\partial r^2} + \frac{1}{r}\frac{\partial T}{\partial r} + \frac{\partial^2 T}{\partial z^2}) + \alpha I(r, z) \tag{2.14}$$

and

$$\tau_{rr} = 2\mu\frac{\partial ur}{\partial r} - \frac{2}{3}\mu(\frac{1}{r}\frac{\partial}{\partial r}(ru_r) + \frac{\partial u_z}{\partial z})$$
$$\tau_{zz} = 2\mu\frac{\partial uz}{\partial z} - \frac{2}{3}\mu(\frac{1}{r}\frac{\partial}{\partial r}(ru_r) + \frac{\partial u_z}{\partial z})$$
$$\tau_{rz} = \tau_{zr} = \mu(\frac{\partial u_z}{\partial r} + \frac{\partial u_r}{\partial z})$$

This equation system is valid for the two convection phenomena which are investigated. However, they differ in the boundary conditions. The equations above are used to simulate the convection phenomena.

2.1.3 Dimensionless numbers

In fluid mechanics, dimensionless numbers are powerful concepts. They can asses which fluid phenomenon dominates, as they express the ratio between different mechanisms. For example, the Reynolds number is the ratio between inertial and viscous forces. Its expression is:

$$\begin{aligned} Re &= \frac{F_{inertial}}{F_{viscous}} \\ &= \frac{\rho U^2}{L} \cdot \frac{L^2}{\mu U}, \\ &= \frac{\rho U L}{\mu} \end{aligned} \tag{2.15}$$

where U and L are respectively the characteristic values for the speed and length of the flow. If the inertial effects are much superior to the viscosity effect, the flow is defined as turbulent and is unstable. On the contrary, if inertial effects are small the flow is laminar and a permanent regime can be reached. If Reynolds number is very small ($<< 1$), the inertial term could be neglected in the Navier-Stokes equation.

In water, the Prandtl number is superior to 1 ($Pr = \frac{\nu}{\kappa} = 7.14$). The velocity changes are higher than the thermal changes, the fluid have a good potential for convection in comparison to conduction. As this number is not very high, the thermal conduction is still very effective.

In order to define the convection mode, the Rayleigh number asses whether the natural convection occurs. It is the ratio of the buoyant force (Archimedes force) and viscous force. If this number is over a critical value ($Ra_c = 1708$ for Rayleigh-Bénard instabilities), a convection flow appears. If it is below the critical value, the heat transfer is mainly conduction. The expression of the Rayleigh number is:

$$\begin{aligned} Ra &= \frac{F_{buoyant}}{F_{viscous}} \\ &= \frac{\beta \Delta T g L^3}{\nu \kappa} \end{aligned} \tag{2.16}$$

Here the characteristic length L can be the water depth.

To compute the dimensionless numbers, the values of the density and viscosity with respect to the temperature are needed.
Table 2.1 summarizes the thermophysical properties of water from 0 to 90 $°C$. It is shown that the viscosity varies significantly as a function of temperature. From this table, polynomial approximations for the density and viscosity for the temperature range of T=[293,363]K are proposed.

$$\rho(T[K]) = 796.2936 + 1.6296T - 3.2077 \cdot 10^{-3}T^2 \tag{2.17}$$

$$\mu(T[K]) = 1.6953 \cdot 10^{-}2 - 0.9.1110 \cdot 10^{-4}T + 1.2485 \cdot 10^{-7}T^2 \tag{2.18}$$

Two examples where convection phenomena can occur in the microfluidic system are presented below. The characteristic values for length and speed are defined from experimental observations. In the first example, the water depth is 1.65 mm and the medium observed speed is about 0.4 mm/s. The laser absorption produces a temperature variation of about 60°C. The Reynolds number is equal to 0.66 and the Rayleigh number is equal to 3869.55.
In the second case, the water depth is 375 μm and a speed of 5 mm/s is observed. The Reynolds number is then equal to 1.875 and the Rayleigh number is equal to 45.43.
For the two examples, the Reynolds number is around 1, because the velocity is high for the

Table 2.1: Thermophysical properties of liquid water (Straub, 1993)

T	ρ	μ	ν	k	κ	C_p	γ	b	β
$^\circ C$	$\frac{kg}{m^3}$	$\frac{10^{-6}N}{sm^2}$	$\frac{10^{-6}m^2}{s}$	$\frac{10^{-3}W}{mK}$	$\frac{10^{-6}m^2}{s}$	$\frac{10^3J}{kgK}$	$\frac{10^{-3}N}{m}$	$\frac{10^{-4}}{K}$	$\frac{10^{-3}}{K}$
0	999.84	1792.3	1.793	561.0	0.1330	4.218			-0.0672
10	999.70	1306.4	1.307	580.0	0.1384	4.192			0.0879
T_0=20	998.21	1002.0	1.004	598.4	0.1434	4.181	73	2.1	0.2067
30	995.65	797.68	0.801	615.5	0.1480	4.177			0.3034
40	992.21	653.25	0.658	630.6	0.1521	4.177			0.3855
50	988.04	547.08	0.554	643.6	0.1558	4.180			0.4578
60	983.20	466.59	0.475	654.4	0.1591	4.184			0.5232
70	977.77	404.06	0.413	663.1	0.1619	4.190			0.5840
80	971.79	354.49	0.365	670.0	0.1643	4.197			0.6414
90	965.31	314.53	0.326	675.2	0.1663	4.206			0.6967

microfluidic system. The inertial forces may not be negligible. In the first case, the natural convection is occurs, but in the second one the Rayleigh number is too small for the onset of natural convection.
As a result, another dimensionless number is introduced: the Marangoni number. It is the ratio between the surface tension force (driving force) and the viscous force (dissipative force). This number assesses the onset of the Marangoni convection, which is a surface-tension-driven phenomenon. The critical value for the onset of the Marangoni convection is 81 (Guyon *et al.*, 2001). The Marangoni number's expression is:

$$\begin{aligned} Ma &= \frac{F_{surfacetension}}{F_{viscous}} \\ &= \frac{\partial\gamma}{\partial T}\frac{\Delta TL}{\kappa\mu} \\ &= \frac{b\gamma\Delta TL}{\kappa\mu} \end{aligned} \tag{2.19}$$

where γ is the surface tension, b its temperature variation rate and ΔT is the temperature variation on the free surface.
In the first example seen above (water depth = 1.65 mm), the free surface is too high from the bottom, the temperature distribution can be considered homogeneous. In the second case, the water thickness is smaller than the absorption length ($L_{absorbtion} = 1/\alpha = 426\mu m$). At this, 60% of the laser power is absorbed, the heat flux is only 40%, the maximum temperature at the surface is estimated as 40% of the maximum temperature at the laser focal point. The gradient is then estimated to 24°C at the surface. The Marangoni number gives 960.2. In this case the Marangoni convection is dominant.

The last dimensionless number to consider is the Bond number, which is the comparison of the gravity effect to the surface tension effect. It can also be considered as the ratio of the

Rayleigh number over the Marangoni number.

$$\begin{aligned} Bo = \frac{Ra}{Ma} &= \frac{F_{buoyant}}{F_{surface_tension}} \\ &= \frac{\beta \Delta T_1 g L^3}{\nu \kappa} \frac{\kappa \mu}{b\gamma \Delta T_2 L} \\ &= \frac{\rho \beta g L^2}{b\gamma} \frac{\Delta T_1}{\Delta T_2} \end{aligned} \tag{2.20}$$

This number varies with L^2 and the ratio between the total temperature variation ΔT_1 over the surface tension variation ΔT_2. In this case, if the water depth (L) decreases, ΔT_2 increases and the Bond number decreases as well. If the Bond number is small ($<< 1$), the surface tension effect drives mainly the flow. In the first case with a larger water depth, $Bo \approx 22$. The buoyant effects drive the flows. In the second case where $L = 375\mu m$, $Bo = 0.0473$. The surface tension effects mainly drive the flows. With the approximation $\Delta T_2 \approx \Delta T_1 e^{-\alpha L}$, the Bond number is equal to 1 for $L = 900\mu m$, and equal to 0.1 for $L = 500\mu m$. The Marangoni effect is dominant when the water is under $500\mu m$.

In the following section, the natural convection is investigated with numerical simulations to define the temperature distribution in the liquid medium and the velocity profile of flows.

2.2 Natural convection

2.2.1 The microfluidic system

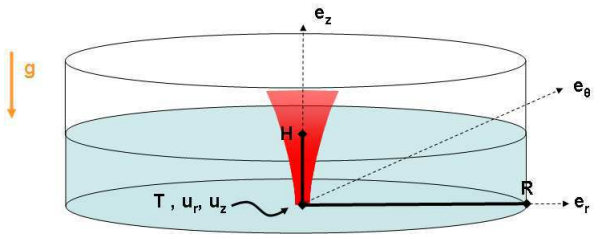

Figure 2.3: The system is a petri dish with a laser heating source at its center. Distilled water fills the dish with a depth of 1.650 mm.

In this section, the flows driven by the buoyant forces and natural are considered. The main hypothesis is that the density is only dependent of the temperature and may be approximated by:

$$\nabla \rho = \frac{\partial \rho}{\partial T} \nabla T \tag{2.21}$$

For a liquid medium, the following approximation may be used if $\beta(T_{max} - T_0) << 1$:

$$(\rho - \rho_0)\boldsymbol{g} = \rho_0 \beta (T - T_0)\boldsymbol{g}, \tag{2.22}$$

where T_0 is the ambient temperature. Also the additional hypothesis $\frac{\boldsymbol{u}\nabla\rho}{\rho\nabla\boldsymbol{u}} << 1$ is considered. The term dependent of ρ variation in the product rule formula is neglected. In this case, the problem corresponds to Boussinesq approximation: the density is considered constant except in

the Archimedes force term. The system of equations is then:

$$\frac{1}{r}\frac{\partial r u_r}{\partial r} + \frac{\partial u_z}{\partial z} = 0 \tag{2.23}$$

$$\rho_0(\frac{1}{r}u_r\frac{\partial r u_r}{\partial r} + u_z\frac{\partial u_r}{\partial z}) = -\frac{\partial p}{\partial r} + \frac{1}{r}\frac{\partial}{\partial r}(r\tau_{rr}) + \frac{\partial}{\partial z}(\tau_{zr}) \tag{2.24}$$

$$\rho_0(\frac{1}{r}u_r\frac{\partial r u_z}{\partial r} + u_z\frac{\partial u_z}{\partial z}) = -(\rho - \rho_0)g - \frac{\partial p}{\partial z} + \frac{1}{r}\frac{\partial}{\partial r}(r\tau_{rz}) + \frac{\partial}{\partial z}(\tau_{zz}) \tag{2.25}$$

$$\frac{1}{r}\frac{r u_r \partial T}{\partial r} + \frac{u_z \partial T}{\partial z} = \kappa(\frac{\partial^2 T}{\partial r^2} + \frac{1}{r}\frac{\partial T}{\partial r} + \frac{\partial^2 T}{\partial z^2}) + \alpha I(r,z) \tag{2.26}$$

and

$$\tau_{rr} = 2\mu_0\frac{\partial ur}{\partial r} - \frac{2}{3}\mu_0(\frac{1}{r}\frac{\partial}{\partial r}(ru_r) + \frac{\partial u_z}{\partial z})$$
$$\tau_{zz} = 2\mu_0\frac{\partial uz}{\partial z} - \frac{2}{3}\mu_0(\frac{1}{r}\frac{\partial}{\partial r}(ru_r) + \frac{\partial u_z}{\partial z})$$
$$\tau_{rz} = \tau_{zr} = \mu(\frac{\partial u_z}{\partial r} + \frac{\partial u_r}{\partial z})$$

There are 4 equations and 4 unknowns : u_r, u_z, T, p. The system can be solved with the following boundary conditions (see Figure 2.3):

Table 2.2: Boundary conditions

Boundary	Coordinate	u_r	u_z	T	p
Wall 1	$z = 0$	0	0		
Wall 2	$r = R$	0	0	T_0	
Free surface	$z = H$	0			p_{atm}
Symmetry axis	$r = 0$				

The last parameter to determine is w_0, the laser waist to calculate Q_l according to 2.8. The laser is focused by a 4× microscope objective whose focal length is 22 mm. The laser beam is collimated to 3 mm in diameter, the wavelength is 1480 nm. The gaussian beam properties give (see Figure 2.4):

$$w_0' = \frac{\lambda f}{\pi\frac{R_l aser}{g}} = 27.6\mu m \tag{2.27}$$

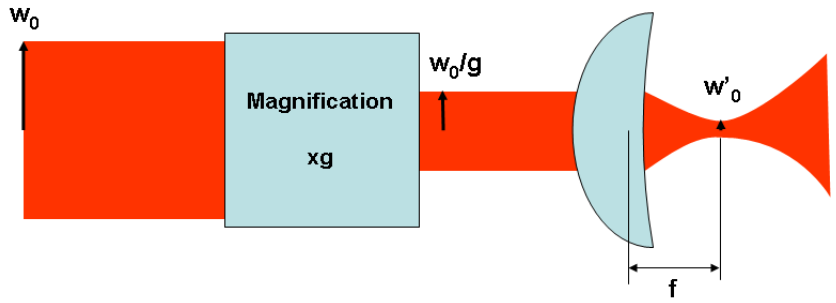

Figure 2.4: Model of an objective: magnification and focusing of the light beam.

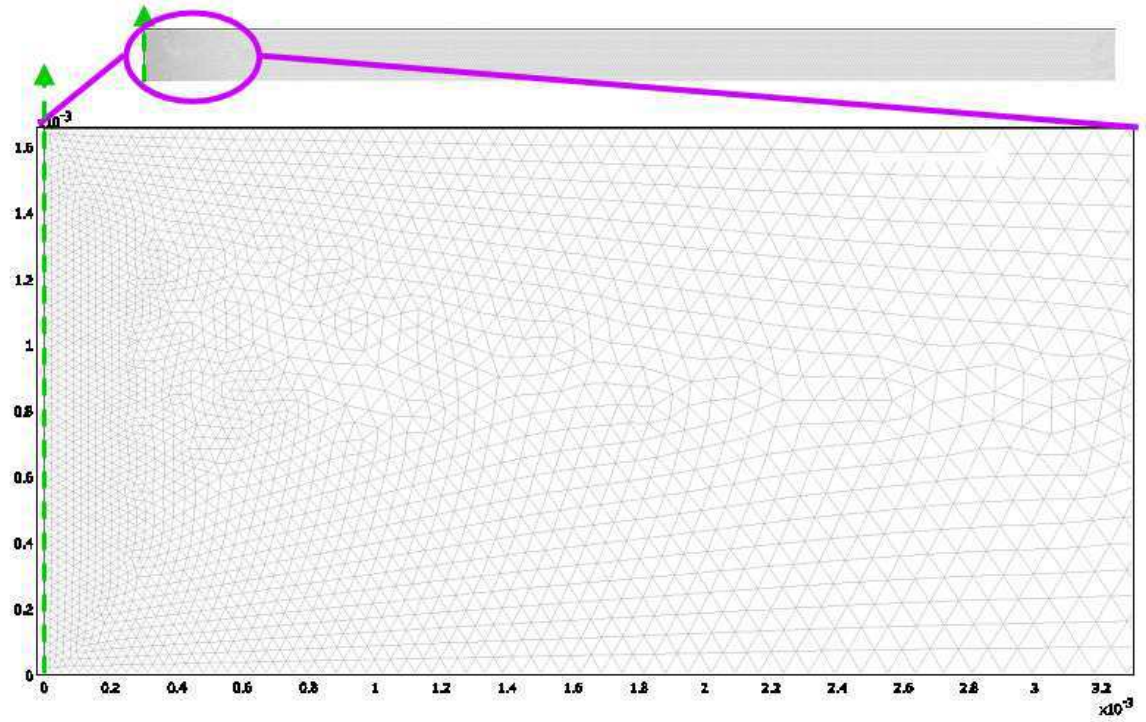

Figure 2.5: Triangular mesh of the finite element solver. The symmetry axis is highlighted in green. The upper figure represents the whole chamber and the below figure is a zoom view around the laser spot.

2.2.2 Simulations

The natural convection system is solved by a numerical method using COMSOL, which is a finite element solver software. It allows to couple different physical laws. The "Incompressible Navier-Stokes" module for fluid dynamics and the "General heat transfer" module for the thermodynamic principles are used. A cylindrical geometry or "axi-symmetry" is selected. The function of the heat flux due to the gaussian beam absorption is integrated as well. The linear "PARDISO" solver for a stationary system with 10^{-2} relative tolerance is used. In order to have a convergent solution, the heat flux is incremented step by step and introduced in the new computed fields as initial values.

The mesh is triangular and refined in the important boundaries where the temperature and velocity variation are high (see Figure 2.5 for the mesh design and Figure 2.9 for the mesh quality). The initial conditions are $T_0 = 293K$, $w_0 = 10\mu$m and $I_0 = 16mW$. The temperature distribution and velocity field are shown in Figures 2.10, 2.6, 2.7.
The maximum temperature is $86.2°C$ for a laser power of 16 mW. The laser heat is confined to a small region of the chamber: the temperature is below $40°C$ for a radial distance larger than 300μm from the laser (see Figure 2.10).
The Archimedes force drives the flows in a vertical manner in the laser spot axis. Flows are directed horizontally in the bottom and the top of the liquid layer (cf. Figure 2.6). The maximum speed is 815 $\mu m/s$ and is directed vertically from the laser spot to the top of the water layer. The radial speed, of main interest for micromanipulation, is more significant around the laser spot, 414 $\mu m/s$ on the water-air interface. A speed of 327 $\mu m/s$ is located at a depth of about 380 μm from the bottom of the Petri dish, in which the flows change their radial direction (cf.

Figure 2.7).
In vertical positions lower than where the maximum speed is located, the radial speed decreases toward the bottom of the petri dish. This is due to a boundary layer around the petri dish's walls. For viscous liquid the flow speed is null in the walls.

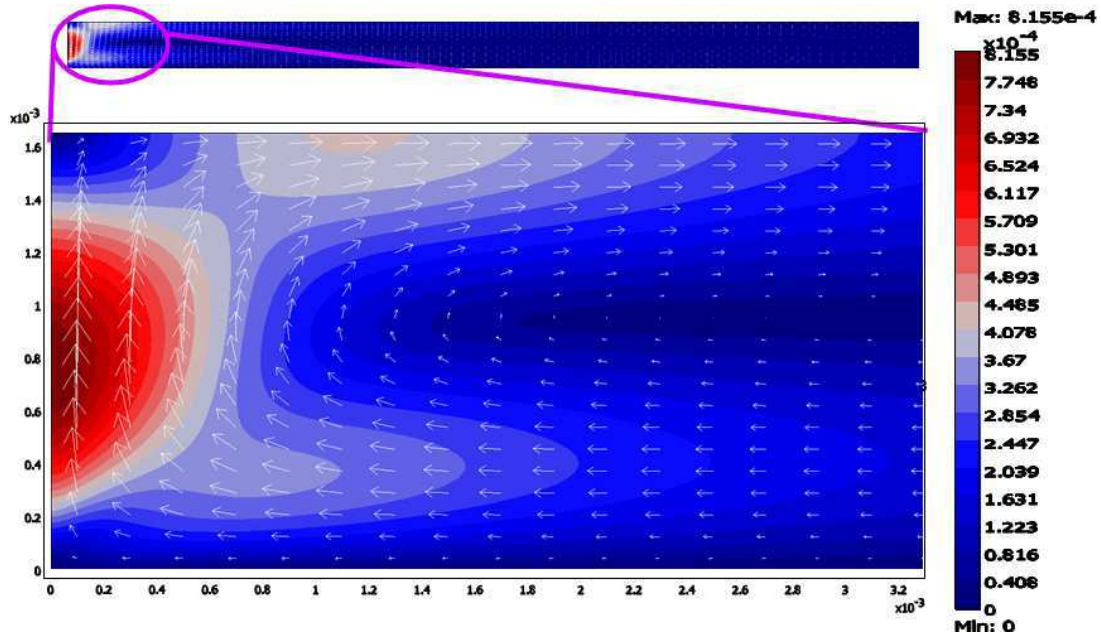

Figure 2.6: Velocity field plotted with arrows. Axis units are in meters.

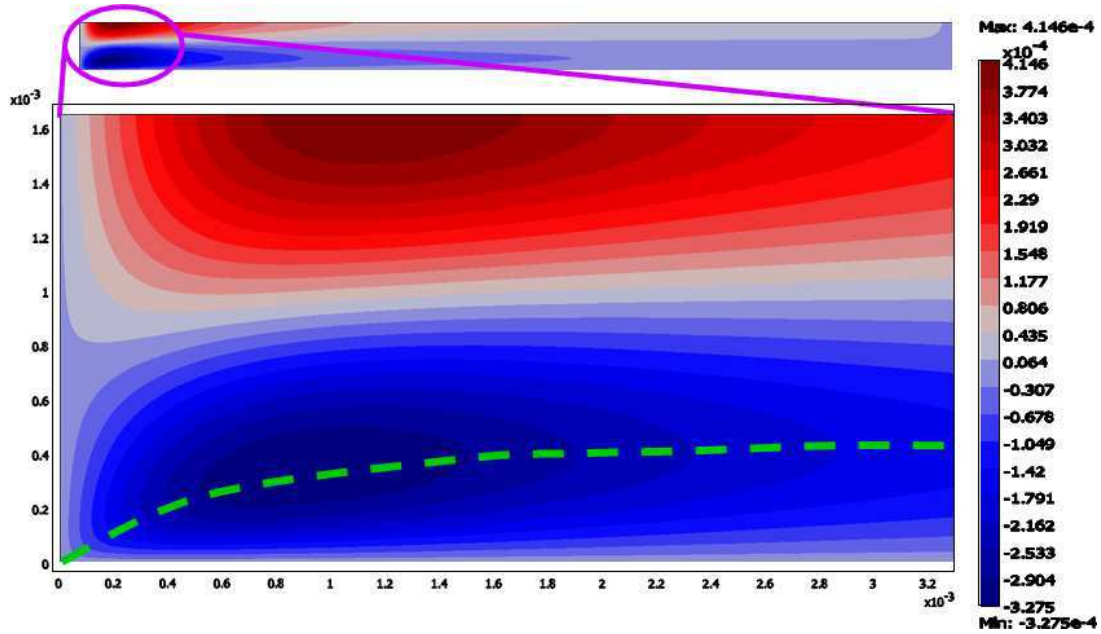

Figure 2.7: Radial speed plotted in contours in m/s. The maximum radial speed in the direction of the laser is highlighted by a dotted line. Axis units are in meters.

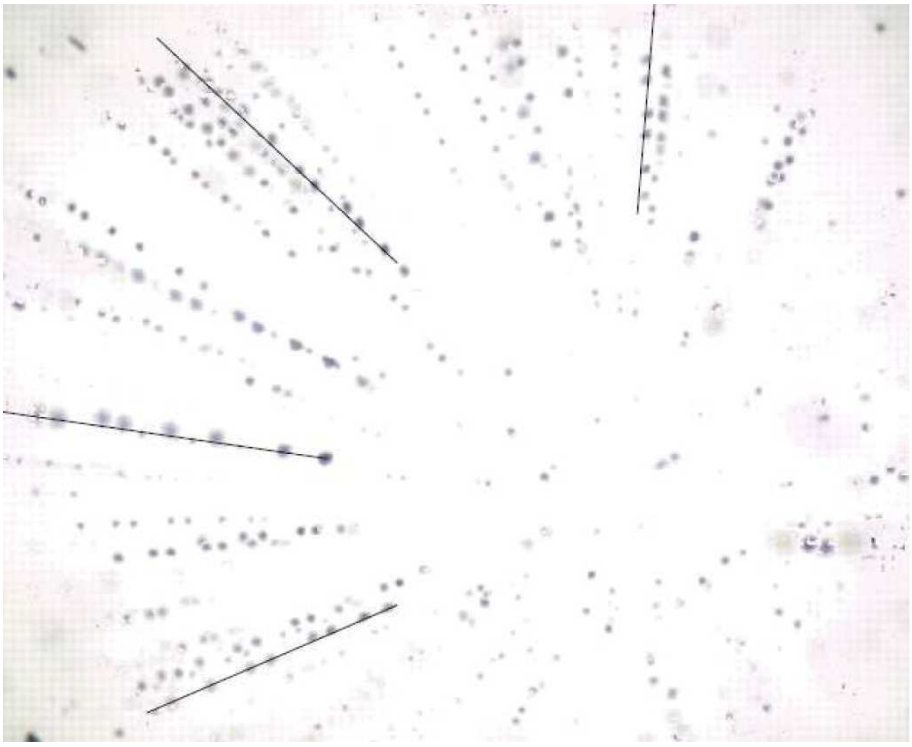

Figure 2.8: Supperposition of 10 images during a laser group manipulation of hollow glass beads. Those images were used to localized the particles in function of time and evaluate their speed.

2.2.3 Comparison to experimental measurements of flows

To compare the simulation results with the experimentally measured flows, the speed of particles with image processing is measured. Hollow glass microspheres whose density is equivalent to water, and diameters between 8 and 12 μm are used. A standard CMOS camera (12 fps,) which gives a view from the bottom of the Petri dish, monitors the experiments. The displacement of the microscope objective changes the image focal plane as well as the laser focal plane. In this velocimetry experiment, 10 s data was taken for different depths of a given water layer thickness (same thickness during the recording while moving vertically the microscope objective). In consequence, the laser spot does not have the same position in the different experiments. The positions were measured manually on the recorded images. This first experimental protocol is not precise and does not allow the treatment of a huge number of data, however it was enough to evaluate the experimental velocity for the natural convection.

It is observed that toward the bottom of the petri dish the particles are directed toward the laser, and toward the free surface they moved away from the laser beam. At the bottom, many particles stick to the Petri dish surface. In Figure 2.8, the rectilinear trajectories and the axial symmetry of the flows are shown.

Figure 2.11 compares the experimental speed values with the simulations. A first observation is that the speed is underestimated by the simulations. The reasons may be that the laser power is not well known after the objective, the simulations rely on hypothesis like the temperature independence of the physical parameters. Another reason may also be the influence of light forces, surface tension and surface deformation.
Qualitatively, the shape of the flows are almost the same and the maximum velocity is about at

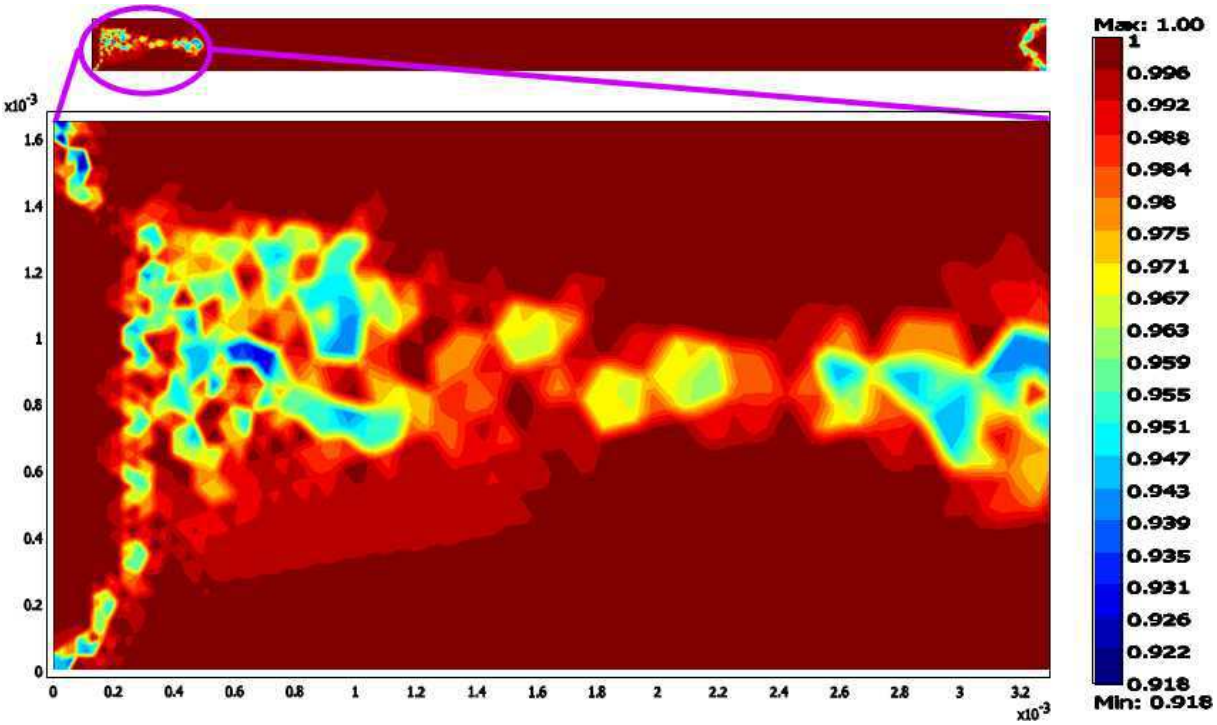

Figure 2.9: The mesh quality refers to triangle angles. For example, a equilateral triangle is equal to 1. If the triangle's angles are inferior to 90°, the solution will be continuous.

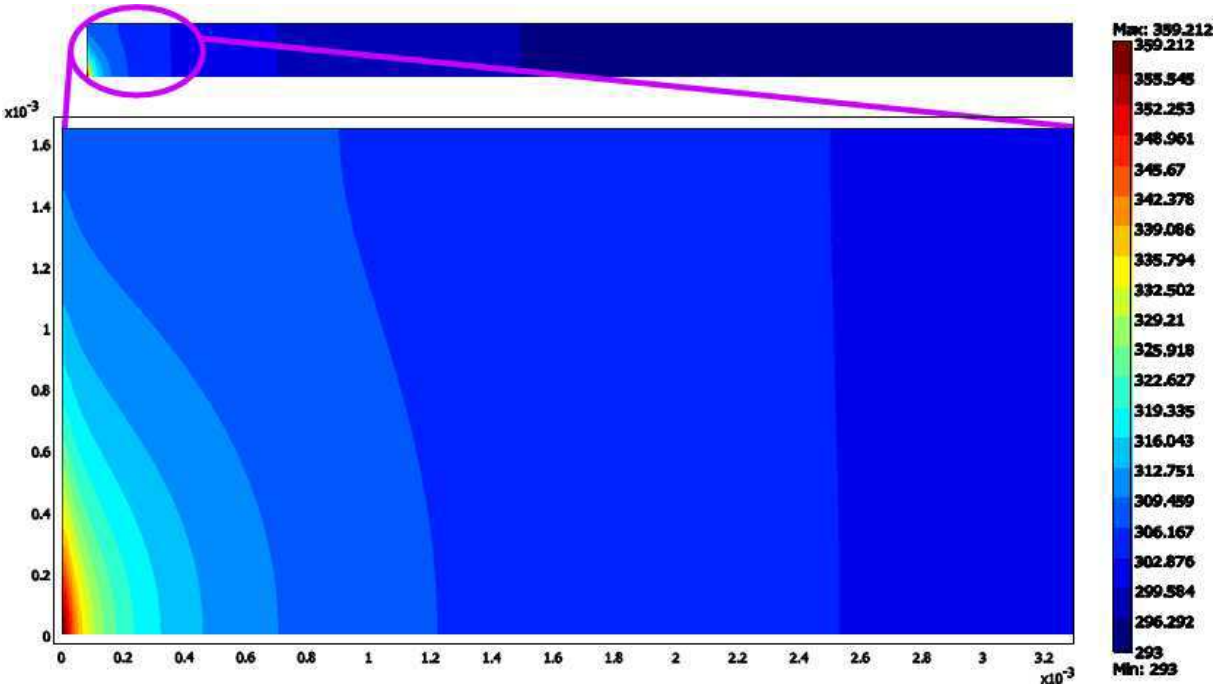

Figure 2.10: Temperature field in Kelvin. Axis units are in meters.

the same radial position. The simulations give thus a good approximation of the velocity and temperature distribution, and help to understand the influence of parameters like water depth or chamber size. Figure 2.12 shows the trajectories of flows in a 3D chamber. The convergence to the laser in the bottom of the chamber and the diverging trajectories at the surface of the liquid can be seen.

Natural convection is limited due to the boundary layer close to the petri dish surface. The height of this layer can totally cover microparts remaining on the substrate, thus reducing their motion speed. The convection phenomenon described in the next section is engendered by surface forces, which are more significant that volume forces at this scale. Therefore, the thermocapillary effect may be more suitable and interesting for micromanipulation.

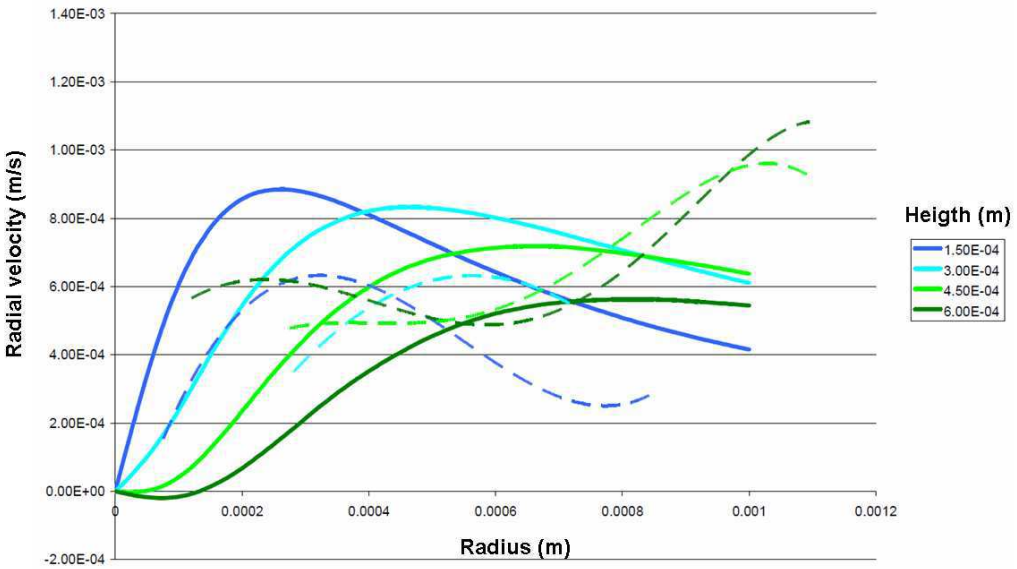

Figure 2.11: Radial speed in function of the radius and height position of the particles. The experimental data are plot with solid lines and the simulation data with dash curves.

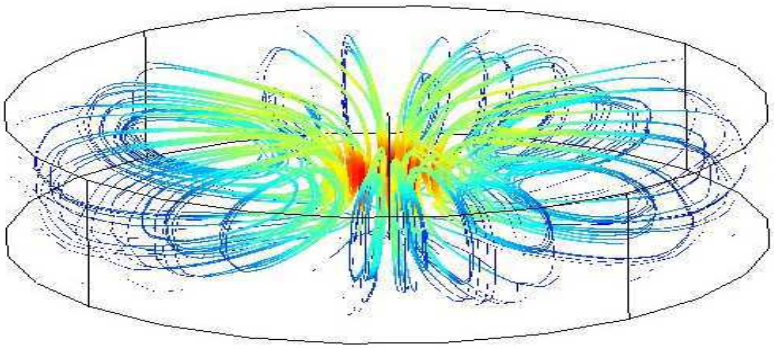

Figure 2.12: Three-dimensional simulation of the fluid trajectories in the fluid chamber with a laser heating source at its center.

2.3 Thermocapillary convection

Before explaining the thermocapillary convection or convection flows due to variations in surface tension with respect to the temperature, a definition of surface tension is presented. The surface tensions play an important role in the equilibrium and flows of fluids.

2.3.1 Surface tension

Surface tension is the energy per unit surface that minimizes the surface interface between two fluids. For instance, a water drop takes a spherical shape to have a minimum surface interface in the air. This energy is due to the internal cohesion forces (van der Waals, hydrogens, ionic and metallic bonds) exerted between the fluid molecules. At the interface, these forces are unbalanced and the work per unit surface realized by the internal forces to keep the fluid in a steady state is the surface tension. It is expressed in N/m.

Variation of surface tension

Surface tension varies with the presence of a surfactant or a temperature gradient.
A surfactant, is a chemical substance composed of molecules having a hydrophilic head and a hydrophobic tail in presence of water. Thus, this substance lays at the interface between two fluids, where the hydrophilic head is in the water part and the hydrophobic tail is in the other medium. A surfactant decreases the surface tension between two fluids because of its affinity for both of them. Therefore, a surfactant concentration gradient induces a surface tension gradient.
The surface tension variation also depends on the temperature. An increase of the temperature reduces the surface tension due to the reduction of the cohesion forces between the molecules of the fluid media. Therefore, a temperature gradient induces a surface tension gradient.

2.3.2 Marangoni effect

The Marangoni effect is the motion of a fluid due to a surface tension gradient (Maroto *et al.*, 2007). As introduced above, this motion can be generated by a surfactant concentration gradient or a temperature gradient at the interface. The fluid motion due to a temperature gradient is also known as thermocapillary convection or Bénard-Marangoni convection.

The first person who observed this phenomenon was Henri Bénard. He investigated the behavior of a thin layer of whale oil by heating it from below with a heating plate. He observed a formation of hexagonal patterns at the free surface (Bénard, 1900). He determined that at the center of a hexagonal cell the flows go up, and at its borders the flows go down (see Figure 2.13). He also explained that in the warmer regions (border of the hexagon) the flows go up and in the colder regions (border of a hexagon) the flows go down (Figure 2.14.)
However, he explained that this phenomenon is due to buoyant forces acting in the bulk of the fluid. In 1958, Pearson theoretically showed that Bénard observations were actually due to variations in surface tension caused by a temperature gradient (Pearson, 1958). This phenomenon is also known as Marangoni convection due to Marangoni's work (Marangoni, 1871).

As this phenomenon is established by surface forces, it is more suitable to work at small scales. For instance, taking L as a characteristic length, surface tension is proportional to L, pressure forces are proportional to L^2 and volumetric forces are proportional to L^3; therefore at small scales the Marangoni effect becomes more significant.

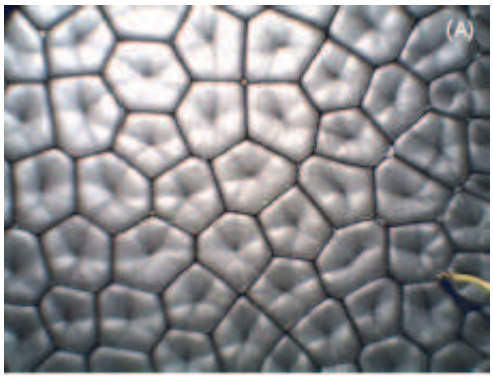

Figure 2.13: Hexagonal pattern formation at the free surface observed in Bénard convection.

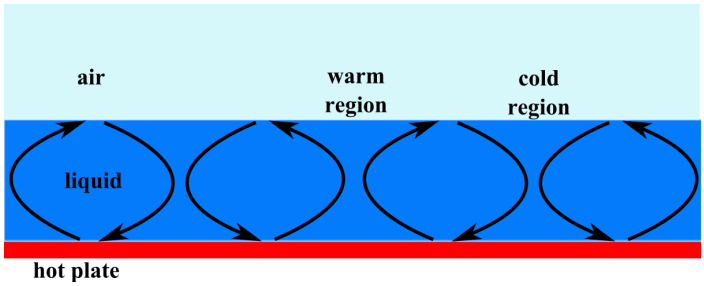

Figure 2.14: Schematic depicting the Bénard-Marangoni convection. Convective cells are shown by the arrows.

In this work, the thermocapillary or Bénard-Marangoni convection is studied and used to perform fluidic actuation-based micromanipulation at the mesoscale.

2.3.3 Working principle

Variations in surface tension at the interface between two immiscible fluids cause an imbalance in the shear stress, which in turn causes fluid motion to arise at the interface. A surface tension gradient can be generated by locally heating from below using absorption of an IR laser (1480nm) in a thin liquid layer that is in direct contact with the air. The surface tension gradient is imparted when the laser or the heat transferred from below reaches the interface. This gives rise to a shear stress gradient and a resultant motion of the fluid. This motion arises in cold regions located away from the laser beam axis and draws liquid from the warm regions. This phenomenon can be explained in terms of a decrease of cohesion forces that is caused by the temperature increase near the laser axis, while within colder regions cohesion forces remain larger. Figure 2.15 illustrates this principle.

An IR laser is used in the proposed system as a heat source to locally heat a thin liquid layer from below to engender localized Marangoni flows. In Figure 2.15a, a toroidal convective cell is established due to the surface tension gradient. At the free surface, the flow is directed away from the laser beam axis because cold regions draw the liquid from hot regions. At the bottom near the glass substrate, the flow is directed toward the laser beam creating a recirculation zone maintaining an overall null net flow for the convective micro-fluidic system. Figure2.15b illustrates the 3D toroidal shape. Figure2.15c depicts the flow velocity profile (Guyon *et al.*,

2001; DaCosta, 1993) and an immersed micro-bead that is dragged by the subsurface flows toward the laser focus. This is the principle used to manipulate meso-sized beads.

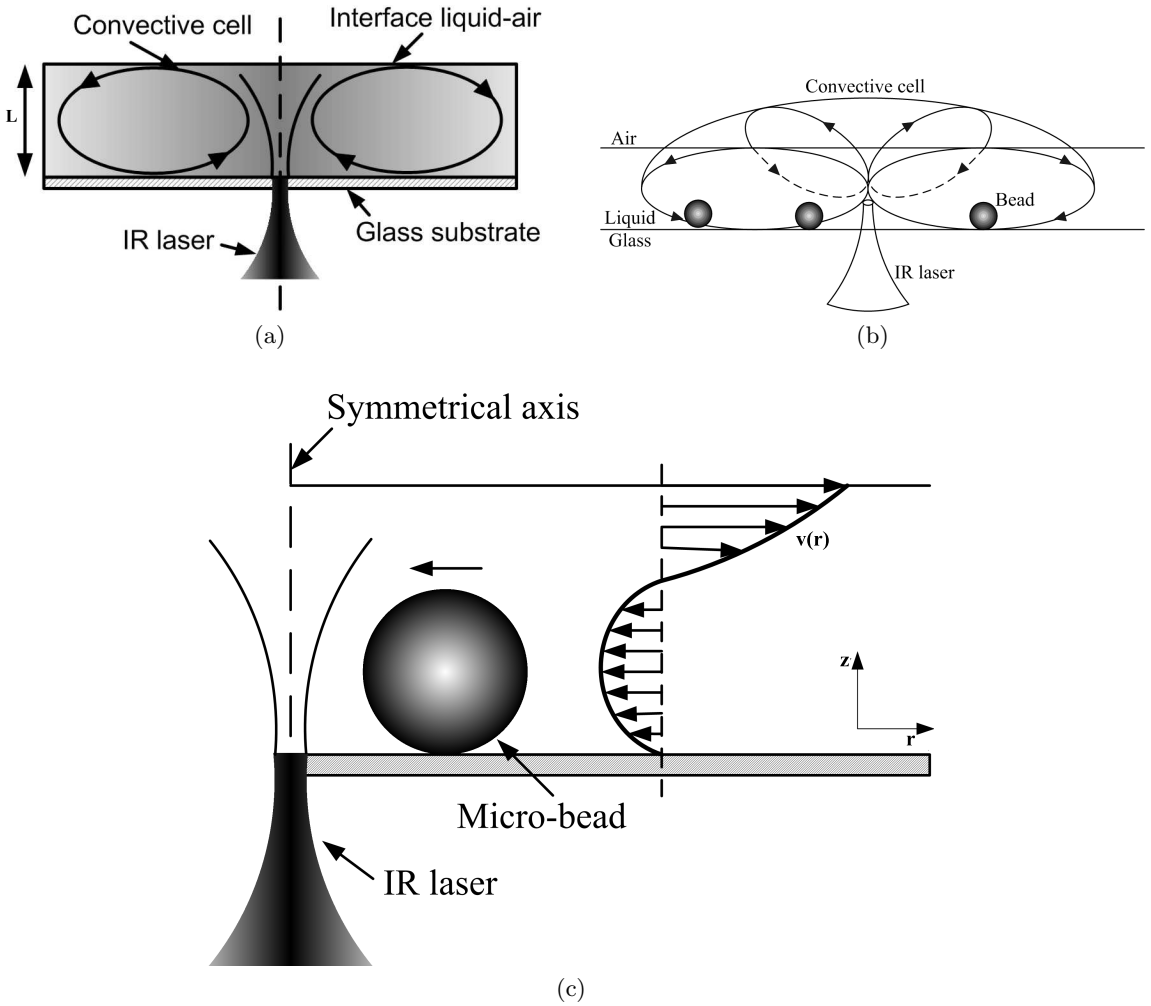

Figure 2.15: Principle of thermocapillary manipulation. (a) IR laser absorption heats a thin film of liquid from below, therefore a convective flow is generated by a surface tension gradient. (b) A 3D representation of the localized flows. (c) Velocity profile of the convection flow in a thin liquid layer heated from below. A micro-bead immersed within the liquid is reached by a velocity profile that drags it toward the laser focus. The arrow above the bead represents the motion direction.

2.3.4 Formulation

In fluid mechanics, the shear stress is proportional to the strain rate and the coefficient of proportionality is the viscosity of the fluid. In Eq. 2.28 this proportionality is given for a Newtonian fluid.

$$\tau = \mu \frac{\partial u_r}{\partial z}, \tag{2.28}$$

where u_r is the horizontal velocity and z is the vertical coordinate (see Figure 2.15c). If the viscous stresses is equal to the thermocapillary stresses at the liquid-air interface, the following

equation is obtained:

$$\tau = \mu \frac{\partial u_r}{\partial z} = \frac{\partial \gamma}{\partial T} \frac{\partial T}{\partial r}, \tag{2.29}$$

where $\frac{\partial \gamma}{\partial T}$ is the temperature derivative of surface tension b_γ. Eq. 2.29 highlights that the shear stress depends on the temperature gradient due to the temperature dependence of surface tension. $b_\gamma < 0$ for most liquids and is taken as a constant in this work. This is a valid assumption since when the temperature is lower than a critical temperature Tc, the surface tension dependence on the temperature is near linear and can be computed by Eotvo's law (Adamson & Gast, 1997). However, (Ramsay & Shields, 1893) adjusted this law by replacing the critical temperature Tc by $Tc-6$, since at this temperature the surface tension is close to zero, giving:

$$\gamma V_m^{2/3} = k_e(T_c - 6 - T), \tag{2.30}$$

where V_m is the molar volume of the liquid and k_e is a constant with a value of about 2.1×10^{-7} Nm/K for most liquids. This relationship shows that the surface tension varies linearly with respect to the temperature, and by computing the derivative, the value of b_γ is found giving a negative slope.

The equations governing fluid motion during heating with a laser beam for Marangoni convection were reported by Longtin *et al.*, 1999. These equations are adjusted according to our system.
First, the geometrical conditions of the system that is used for the experiments are introduced. Thus, the governing equations and boundary conditions can be given. A petri dish with 5.8 cm in diameter is used, in which water is filled until obtaining a predetermined water depth. An IR laser with 1480 nm of wavelength and 120 mW of power is used as a heat source in the liquid medium. This heat flux is due to the laser radiation absorption in water. The absorption coefficient is 23.45/cm for this wavelength. The laser beam is focused into the sample through a microscope objective (MO) 4× with a focal length $f = 22$ mm. To estimate the waist Eq. 2.27 is used.
The governing equations are the same that in section 1.2.1, however the boundary conditions change. Eq. 2.29 becomes a boundary condition in the equation system due to the Marangoni effect at the free surface.
The equation system is as follows:

$$\begin{aligned}
&\frac{1}{r}\frac{\partial r u_r}{\partial r} + \frac{\partial u_z}{\partial z} = 0 \\
&\rho_0\left(\frac{1}{r}u_r\frac{\partial r u_r}{\partial r} + u_z\frac{\partial u_r}{\partial z}\right) = -\frac{\partial p}{\partial r} + \frac{1}{r}\frac{\partial}{\partial r}(r\tau_{rr}) + \frac{\partial}{\partial z}(\tau_{zr}) \\
&\rho_0\left(\frac{1}{r}u_r\frac{\partial r u_z}{\partial r} + u_z\frac{\partial u_z}{\partial z}\right) = -(\rho - \rho_0)g - \frac{\partial p}{\partial z} + \frac{1}{r}\frac{\partial}{\partial r}(r\tau_{rz}) + \frac{\partial}{\partial z}(\tau_{zz}) \\
&\frac{1}{r}\frac{r u_r \partial T}{\partial r} + \frac{u_z \partial T}{\partial z} = \kappa\left(\frac{\partial^2 T}{\partial r^2} + \frac{1}{r}\frac{\partial T}{\partial r} + \frac{\partial^2 T}{\partial z^2}\right) + \alpha I(r,z)
\end{aligned}$$

The boundary conditions are:

$$z = H: \ \frac{\partial u_r}{\partial z} = \frac{1}{\mu} b_\gamma \frac{\partial T}{\partial r}, \tag{2.31}$$

$$r = 0, r = R, z = 0 : u_r = 0, \tag{2.32a}$$
$$z = 0, z = H, r = R : u_z = 0, \tag{2.32b}$$
$$r = 0, r = R : \frac{\partial u}{\partial r} = 0, \tag{2.32c}$$
$$z = 0, z = H : \frac{\partial T}{\partial z} = 0, \tag{2.32d}$$
$$r = 0, r = R : \frac{\partial T}{\partial r} = 0, \tag{2.32e}$$

where R is the radius of the petri dish and H is the position of the free surface in z coordinate.

The equation system for the Bénard-Maragoni convection was introduced as a reference for numerical simulations.

2.4 Conclusions

The Bénard-Marangoni convection appears as an adapted solution for manipulation and assembly of micro/meso components in a liquid medium.
This convection is dependent of surface forces, hence dominates the natural convection, which is volume-dependent. An analysis of dynamic Bond number confirms this approach for the microscale.

As the motion of the microparts is due to the motion of the liquid around them and these flows are generated by local heating, it is possible to create complex patterns by scanning the laser beam on the manipulation area. Moreover, the method is independent of the properties of the manipulated parts.
A detailed experimental analysis of the Marangoni convection is discussed in the next chapter.

Chapter 3

Experimental analysis of thermal-induced convection flows

> There are two possible outcomes: if the result confirms the hypothesis, then you have made a measurement. If the result is contrary to the hypothesis, then you have made a discovery.
>
> Enrico Fermi

3.1 Introduction

This chapter describes the experimental analysis of thermal-induced convection flows and the used micromanipulation system.
Main components of the system are a 2 degrees of freedom actuated mirror and an infra red laser as thermal source.
This system is used to characterize convection flows generated by laser absorption. Accordingly, an estimation of the fluidic force exerted on a spherical microbead is reported.
Finally, relevant physical parameters are discussed for an optimal use of these flows as a non-contact micromanipulation method.

3.2 Experimental set-up

The experimental set-up (see Fig. 3.1) consists of an inverted microscope (Olympus IX71) with a 4× objective (numerical aperture NA= 0.1; working distance = 18.5 mm), a high speed DALSA Genie Monochrome CMOS camera (1", 1400 × 1024 pixels, 60 fps), an IR laser (1480 nm, 120 mW; Octax GmbH) and a 2 degrees of freedom (DOF) mirror scanner.
A petri dish (soda-lime-glass, 60 mm in diameter and 12 mm in height) is used as a sample reservoir. Distilled water is used as the liquid medium. The filling depth is$\leq$ 0.6 mm for most experiments while maintaining a free surface, air-water interface. Figure 3.5 shows the schematic of the experimental set-up. A dichroic mirror (from Octax GmbH) reflects the IR laser beam into the microscope objective entrance pupil. The objective focuses the laser beam on the sample.
The dichroic mirror is mounted on a 2 DOF mechatronic device (cf. Figure 3.3). Hence, the

laser beam can be focused on any point on the bottom of the petri dish. It is also possible to produce different scanning patterns such as lines and circles.
A high-speed camera mounted on the microscope records the experiments. Additionally, a C-mount Olympus lens adapter 0.33× is coupled to the camera to enlarge the field of view on the computer screen.

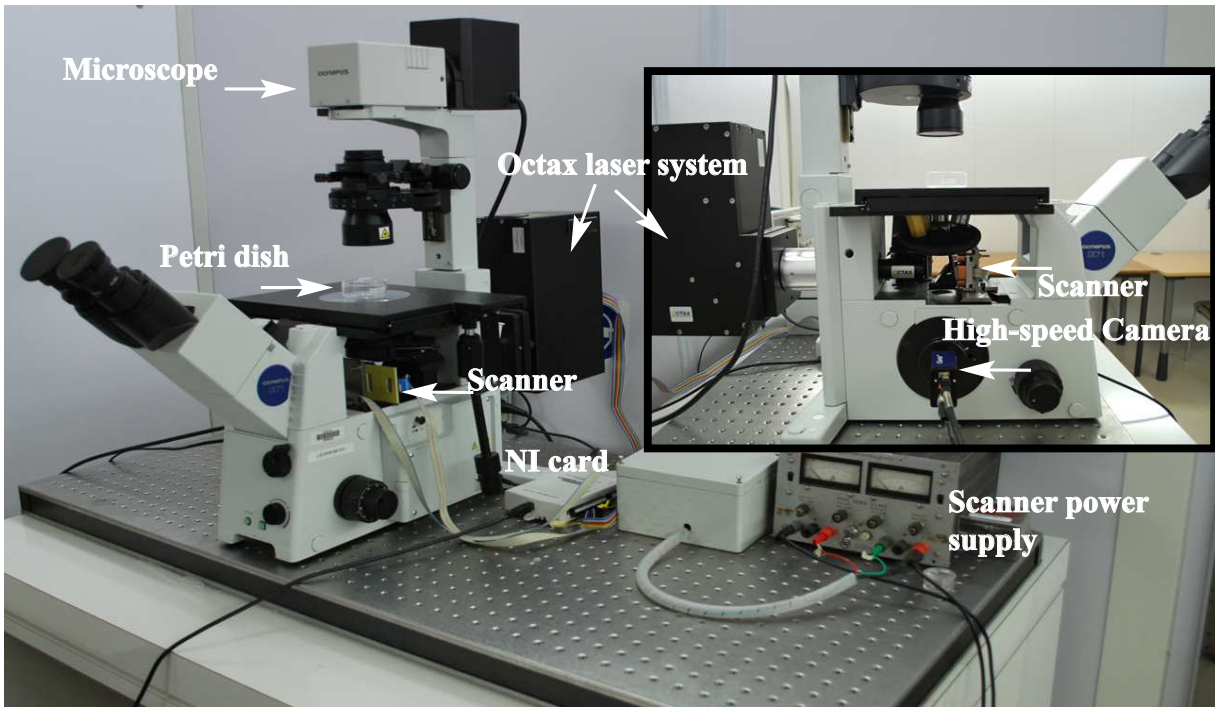

Figure 3.1: Experimental set-up. Inset: close-up view of the microscope left part.

3.2.1 Microheat source: Infrared laser $\lambda = 1480$ nm

The actuation principle is based on thermal phenomena. A local heat source is hence needed to produce thermal energy in the liquid medium.
There are different ways to generate heat in microfluidic systems for thermal-based micromanipulation, such as microheaters (Darhuber *et al.*, 2003), microresistors (Basu & Gianchandani, 2009) and photothermal effect (Ohta *et al.*, 2007). In the case of microheaters, they have to be patterned onto a substrate surface in defined paths by microfabrication processes. This approach is limited to manipulate microparts of predefined size. The displacement precision can not be varied which make this process not flexible. Moreover, it is challenging to connect independently the microheaters. Microresistors have the same drawbacks mentioned above. On the other hand, Ohta *et al.*, 2007 uses localized non-coherent light absorption onto a photopolymeric substrate. The heat produced by absorption in the substrate is transferred to the liquid medium engendering thermocapillary forces that move air bubbles.

We propose an addressable laser beam as the heat source. As laser absorption depends on the liquid media, an infra red diode laser with 1480 nm in wavelength and 120 mW in power is used. At this wavelength the absorption coefficient of water is 23.45/cm as shown in the absorption spectrum in Figure 3.2. This kind of diode laser source is generally used in biomedical application such as in vitro fertilization (Hollis *et al.*, 1996).

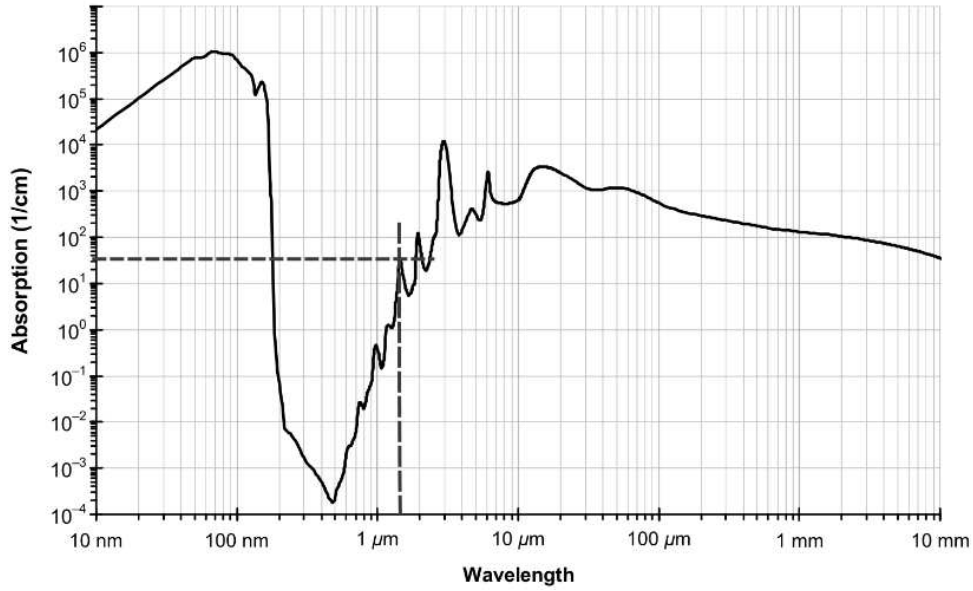

Figure 3.2: Water absorption spectrum. The dotted lines show the absorption coefficient for a wavelength of 1480 nm

3.2.2 2-DOF mirror scanner

In order to be able to address any position on the sample, the laser beam has to be moved and controlled. Several techniques are mentioned in the literature, such as holograms using a spatial light modulator (Cordero *et al.*, 2008), acousto-optic deflectors (Ferrari *et al.*, 2005; Reddy & Saggau, 2005), microlens array (Merenda *et al.*, 2007), or laser scanning with galvanometric mirrors (Arai *et al.*, 2004).

In this work, an 2-DOF TIP/TILT laser scanner (cf. Figure 3.3) is used to address the laser and to perform different scanning patterns. This device, developed by (Roselier & Hafez, 2006), is a compact mechatronic system actuated by four electromagnets in a push-pull antagonistic configuration. The forces exerted by the actuators are illustrated in Figure 3.3b. The magnitudes of these forces are identical for each magnet. They are placed on four cardinal positions around the pivot of the mirror holder. Hence, a couple of magnets induces 1 degree of freedom in rotation.
Due to its dimensions ($50\times50\times15$ mm^3) the scanner is easy to mount on the inverted microscope, under the nosepiece as shown in Figure 3.4.
As seen in Figure 3.3c, a dichroic mirror is mounted on the scanner's flat plate in order to reflect the laser beam. The scanner is mounted onto the microscope in such a way that its flat plate would be in vertical position under the microscope objective. Then the dichroic mirror is placed onto the flat plate with a 45° angle. In this configuration, the dichroic mirror makes a 45° angle with the incident laser beam and the microscope optical axis. As shown in Fig. 3.5, this configuration allows to address the laser on the sample without interfering with the imaging light toward the high-speed camera, thus reducing considerably the laser beam optical path. Also, the compactness of the configuration ensures that the micromanipulation system would fit within the inverted microscope.

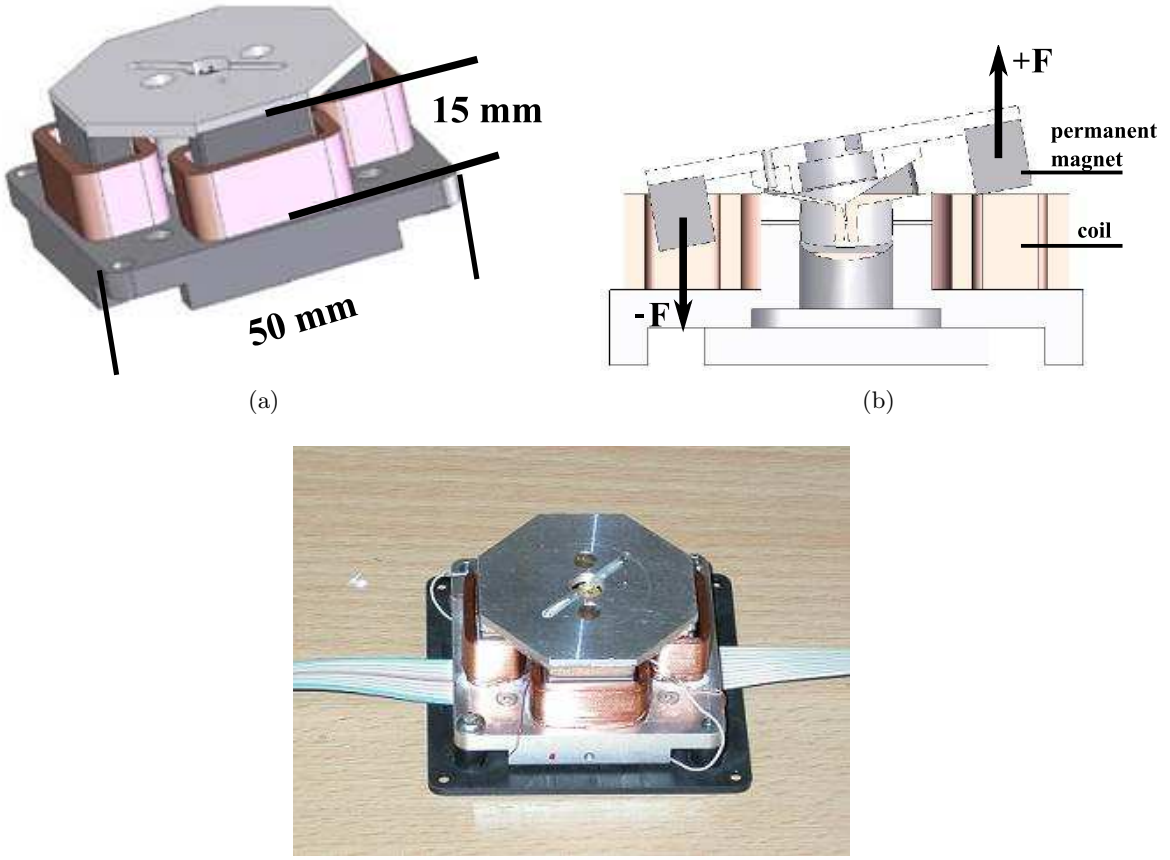

(a) (b)

(c)

Figure 3.3: TIP/TILT laser scanner. (a) Compact mechatronic device actuated by four electromagnets. (b) Cross view showing the forces exerted **F** by the electromagnetic actuators in a push-pull configuration. (c) The laser scanner prototype.

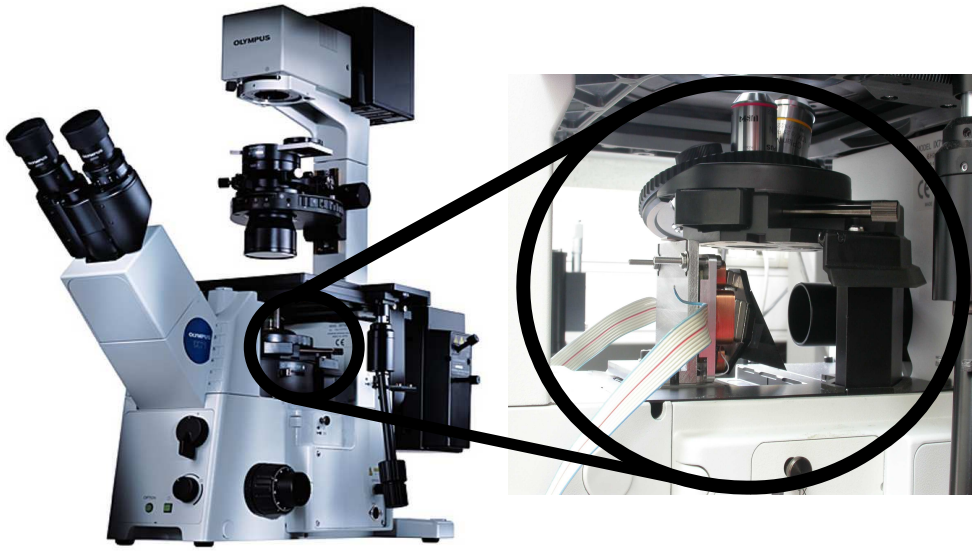

Figure 3.4: TIP/TILT laser scanner mounted on the inverted microscope, under the nosepiece.

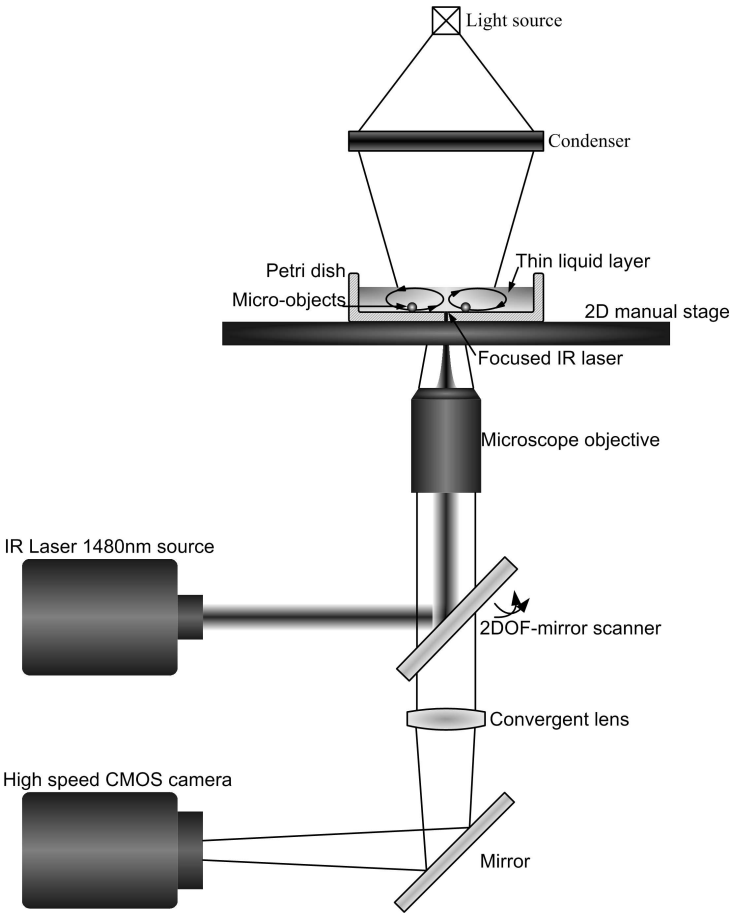

Figure 3.5: Experimental set-up. An IR laser 1480nm is directed by a 2-DOF laser scanner to the microscope objective to be focused on the petri dish bottom surface. The laser scanner also allows the imaging light to pass toward a high-speed camera.

Technical specifications

The scanner is controlled with a National Instruments data acquisition card (NI 6211, M Series 250KS/s, 16 bits). Two analog outputs are used to send the set-point signals to the two pairs of counter actuators.

In Figure 3.6, a Bode diagram of the laser scanner is shown. The input is the signal sent to the actuators and the output is obtained from the flat plate displacement. The position of the flat plate is obtained with a position sensitive detector (PSD) giving an analog output.

A resonance appears at 20 Hz. This resonance is due mainly to the bearing structure design. The slope of the amplitude Bode diagram after the resonance frequency is -40 dB/decade. The phase of the system is about -30° at low frequencies, -90° at the resonance (20 Hz) and -180° at higher frequencies.
With the frequency resonance (ω_r), we can estimate the response time to 5% before reaching the reference signal as follows: $t_{r5\%} = \frac{3}{\omega_r}$ giving 150 ms.

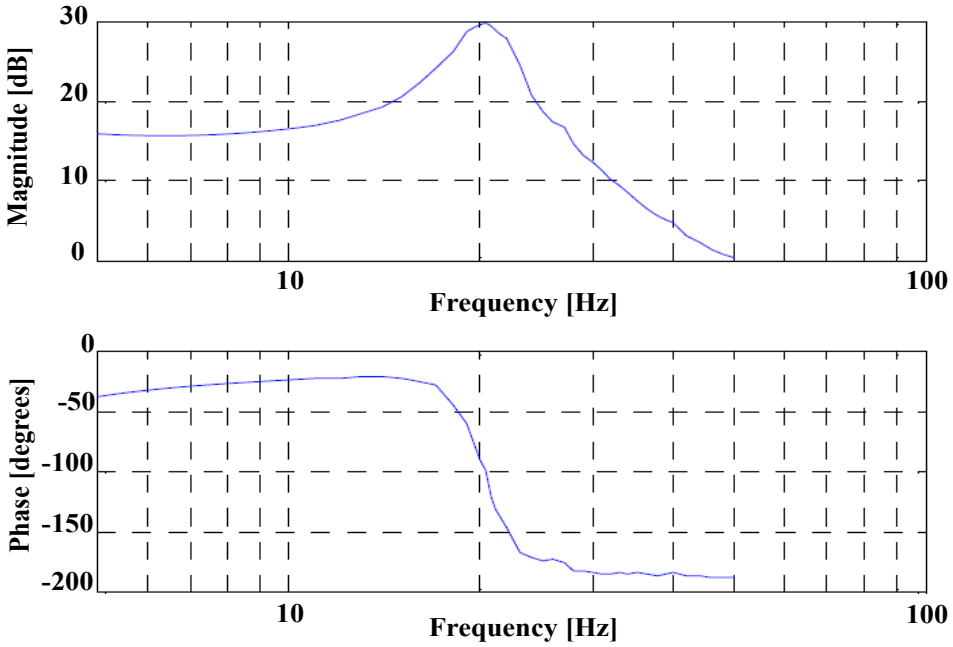

Figure 3.6: Frequency response of the laser scanner.

3.2.3 Sample preparation

A glass petri dish is used as a sample reservoir. It is filled distilled water containing micro-objects.

The petri dish is first rinsed with distilled water and then dried. Isopropanol is used as a solvent to remove any organic material. Then isopropanol is removed and the petri dish dried with pure and dry pressured gas.

Distilled water is filled through a pipette. To obtain a desired depth, the water depth is measured by focusing the microscope objective first at the glass-water interface and then at the

water-air interface. The water depth hence sequentially adjusted by adding or removing droplets with the pipette until getting the working depth.
Next, micro-objects are carefully deposited on the water-air interface using tweezers. In order to immerse objects in the medium, a droplet is removed from the sample with a pipette and then re-dropped on them.

The microscope objective is focused at the glass-water interface in order to focus the IR laser and to image the micro-objects.

3.3 Experimental analysis of convection flows

In order to characterize convection flows, velocity patterns of glass spherical beads ranging from 31 μm up to 270 μm in diameter are measured. Moreover, the effect of the water depth on the disturbed liquid zone due to the laser spot is presented. These analysis lead to an estimation of the fluidic forces acting on the spherical beads.

3.3.1 The disturbed fluidic zone

When heating a thin water layer from below using an IR laser, toroidal-shaped subsurface flows are generated around the focal point. Localized high-speed flows can then be shaped within an extent water layer. Micro-objects remaining within this region are dragged toward the focal point by the subsurface flows, and dragged away by the surface flows.
The IR laser is shot at the middle of a petri dish containing distilled water and hollow glass beads ranging from 8 up to 12 μm used as tracers. Their densities are close to water density.
Figure 3.7 shows a region of convection flows (lighter gray zone) while focusing at the petri dish's surface. This region appears when the laser is shot. Beads within this part are radially dragged by the flow toward the center, where the laser is focused. At this point beads are directed toward the water surface and they start going out of focus. Therefore a darker zone is built up. This picture was taken when the convection region reaches its maximum diameter. The water depth is 450 μm and the measured radius is about 2.15 mm.

In Figure 3.8 the variation of the fluidic radius with respect to the water depth is shown. Three different water depths, 150, 300 and 450 μm are compared. The fluidic flow radius increases with the water depth. For a depth of 150 μm a radius of about 1.2 mm is obtained; and respectively a radius of 2.15 mm for 450 μm in water depth. Each measurement is repeated five times.

In Figure 3.9 an image sequence of a convection cell build-up is depicted. Ten images are shown at 110 ms intervals. Images capture rate is 100 Hz. It was observed that at 20 ms particles laying at the bottom surface starts moving. The time for the convection cell to reach its maximum diameter is about 1 s. At 220 ms, the diameter is already about 70% of its maximum value.

3.3.2 Velocity measurements

To proceed with bead velocity measurements, toroidal convection flows are generated by heating a thin water layer from below using a focused IR laser. A spherical glass bead is placed at a distance from the IR focal point. When the laser is switched on, the fluid starts moving and the bead is dragged toward the laser. The motion of the bead is captured by a high-speed camera

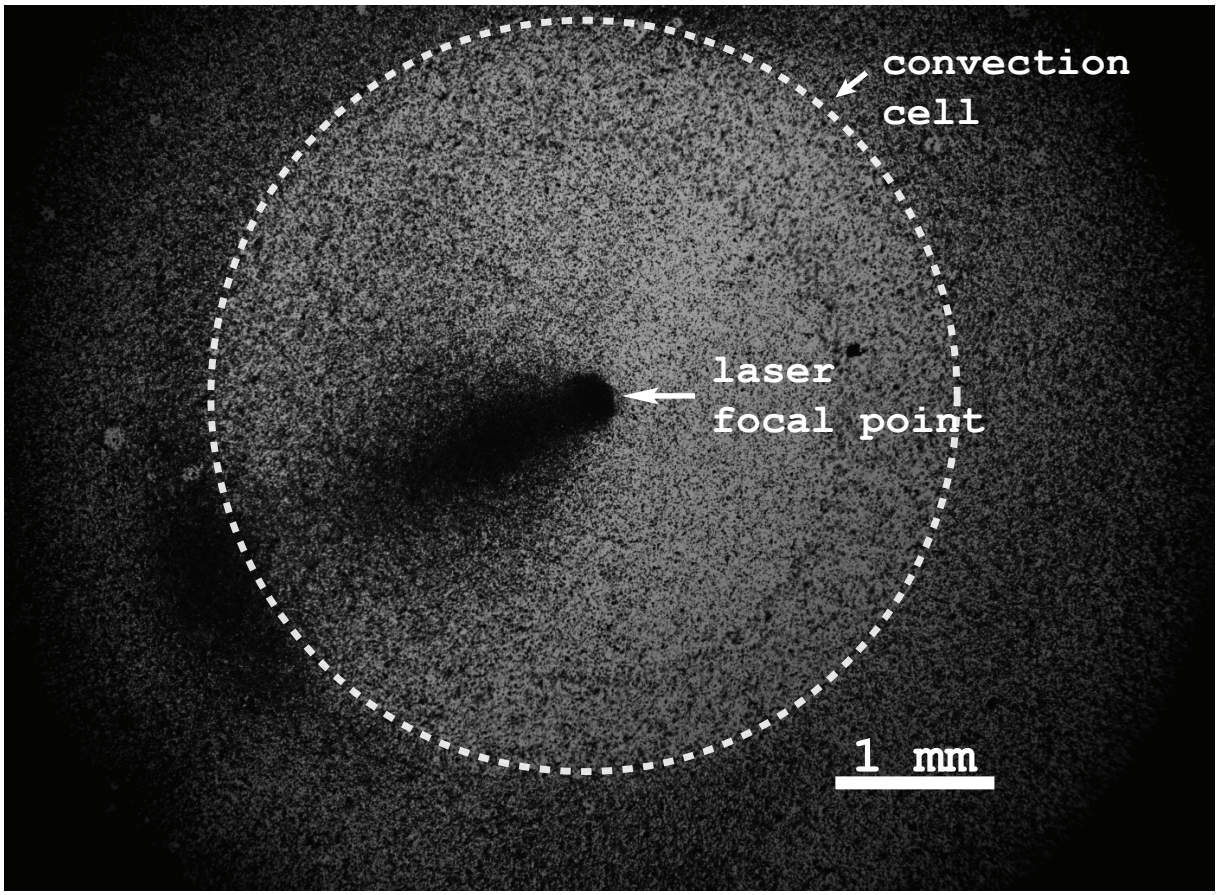

Figure 3.7: Picture of a convection cell within 450 μm of water depth. At the center, the accumulation of beads show the laser position. Hollow glass beads in the range of 8 up to 12 μm are used as tracers.

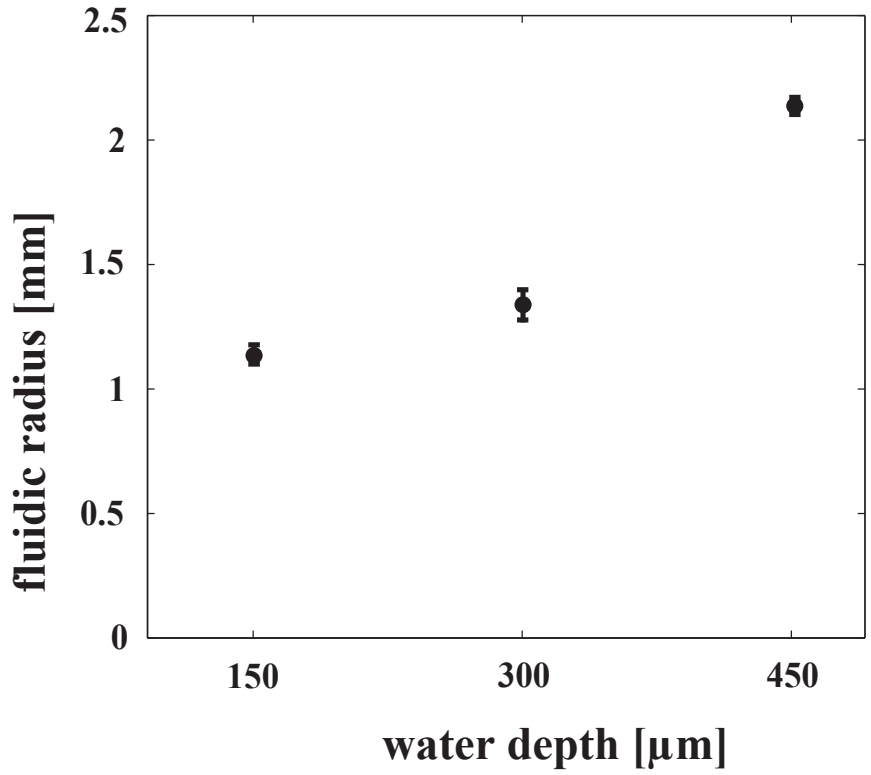

Figure 3.8: Fluidic flow radius vs different water depths. The radius increases with the water depth. Error bars are taken over ten measurements.

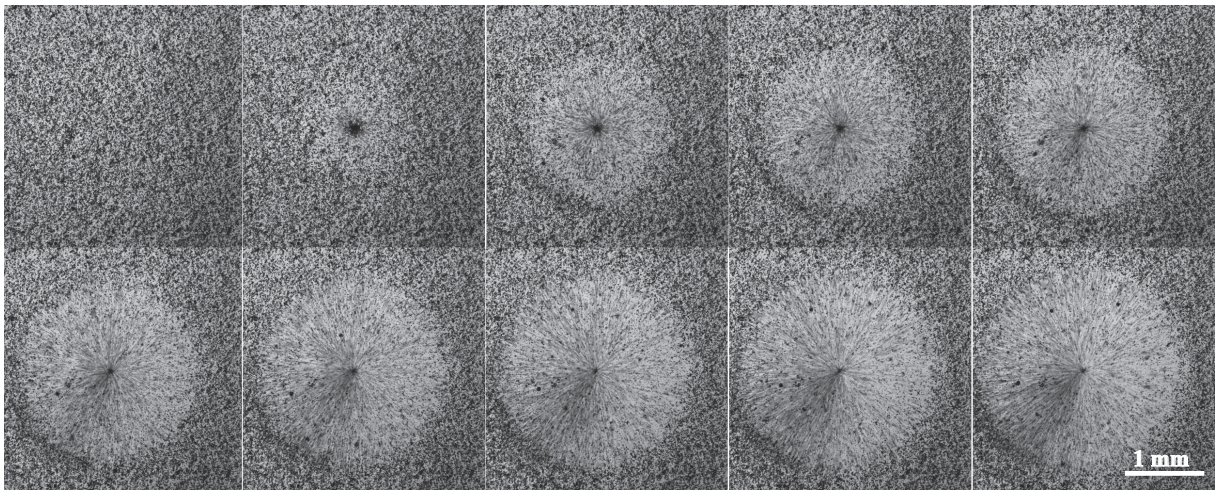

Figure 3.9: Convection cell build-up while irradiating with an IR laser. The laser position is at the center of the convection cell. Every picture is shown at 110 ms of intervals. The water depth is 150 μm and particles used as tracers are hollow glass beads of 8-12 μm in diameter.

at a frame rate of 80 Hz. The sequence is analyzed by image processing to compute the bead position in respect to the laser focal point. The velocity profile is then obtained by the difference between two successive bead positions multiplied by the frame rate.

The velocity of different bead sizes within different water depths are investigated. The bead sizes range from 31 μm up to 270 μm. The water depth values are 375, 450, 600 and 750 μm. It should be noted that the beads remaining at the petri dish surface before switching the laser on are laying on the glass-water interface. Each measurement shown is the mean of ten measurements.

Figure 3.10 shows an image sequence and associated image processing for bead velocity measurements. A glass bead was placed at a specified distance (about 800μm) from the laser focus. The laser is then switched on in a continuous mode and switched off once the glass bead reaches the laser focal point. When the IR laser was on, the bead moves toward the laser focus (white region in Figure 3.10a) and stops close to the focal point. The glass bead's displacement is monitored with the high speed CMOS camera at 80 Hz. The images are processed (3.10b) one by one, to determine the distance and velocity field between the bead's center of mass and the laser focal point. The velocity is then computed by multiplying the difference between two successive center-of-mass positions and the frame rate.

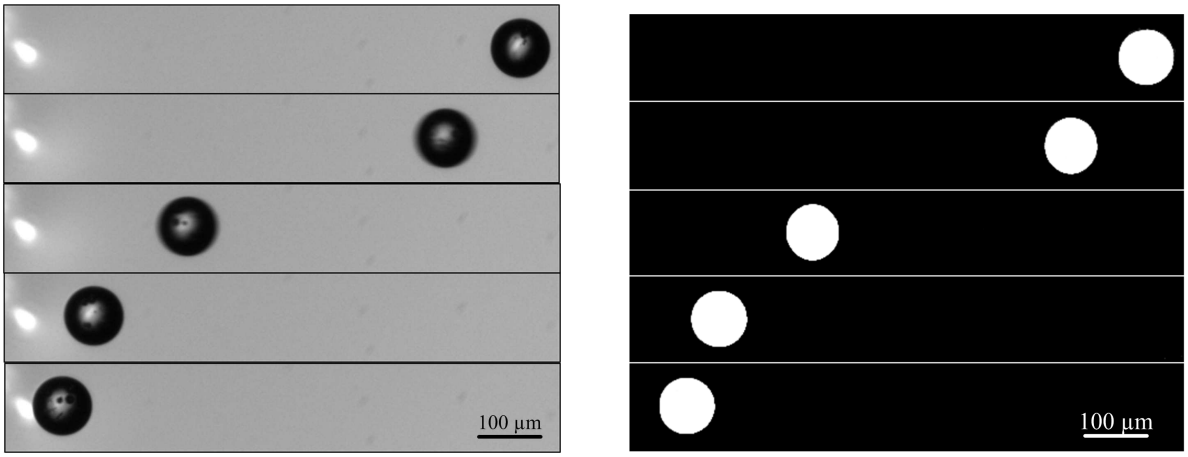

(a) (b)

Figure 3.10: Image sequences for velocity measurements of a spherical glass bead with 92μm in diameter and within 600μm of water depth. One image every 212.5ms is shown. (3.10a) Sequence taken at 80Hz. (3.10b) Image processing to determine the velocity field between the laser and bead. The mass center is obtained from the white region for each image, and then the distance between two successive mas center is computed and multiplied by the frame rate. Scale bar 100μm.

Figure 3.11 depicts the radial velocity field of a glass bead of diameter 92 μm, immersed in water and in contact with the petri dish surface. The zero point of the x axis corresponds to the focal point of the laser. Marangoni convection depends inversely on the liquid depth: the smaller this depth, the larger the flow velocity. Three different water depths of 375, 450 and 600 μm were investigated.
As shown in this Figure, the bead velocity field increases while decreasing the water depth. This is due to the increase of the temperature gradient at the water-air interface, as more energy

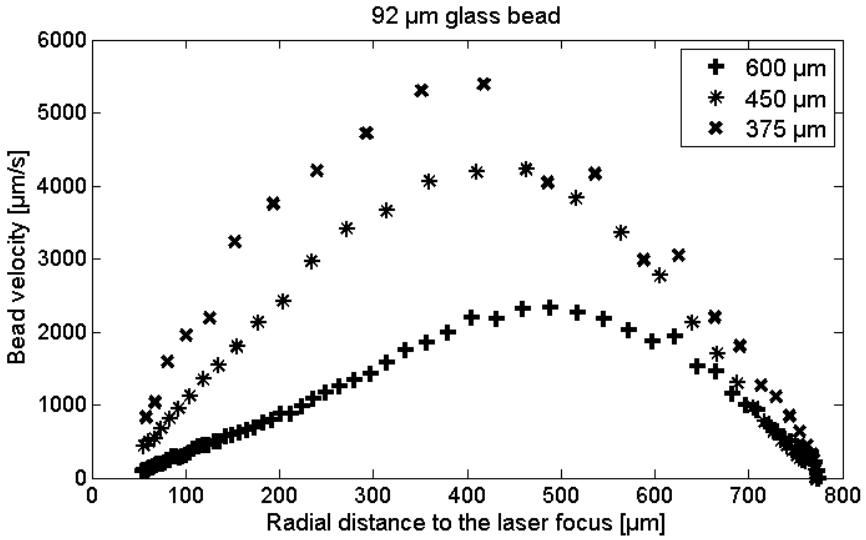

Figure 3.11: Velocity of a glass bead with 92μm in diameter vs the radial distance of the bead center to the laser focus (origin) with 3 different water depths.

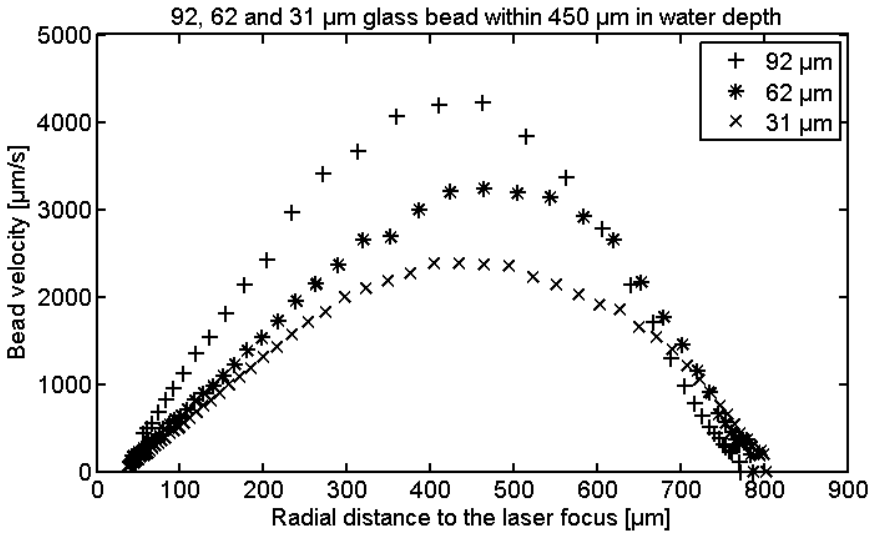

Figure 3.12: Velocity of 3 different glass beads of 92, 62, 31 μm in diameter vs the radial distance to the laser focus.

from the laser beam reaches this interface: the absorption coefficient, 23.45/cm, leads to a laser penetration of about 425 μm. An increase in the temperature gradient causes an increase in the velocity gradient.

It is observed that the bead velocity increases until reaching a maximum, then decreases as the bead approaches the laser focal point. This is because that at the beginning the bead starts being dragged by the flows, thus gaining in speed. However, approaching the laser or heat source, the flows starts going up. It means that the flows change their direction from radial to vertical. Therefore, the bead is dragged by a decreasing radial flow. As a result, the bead stops in the laser position where the radial flow is null.

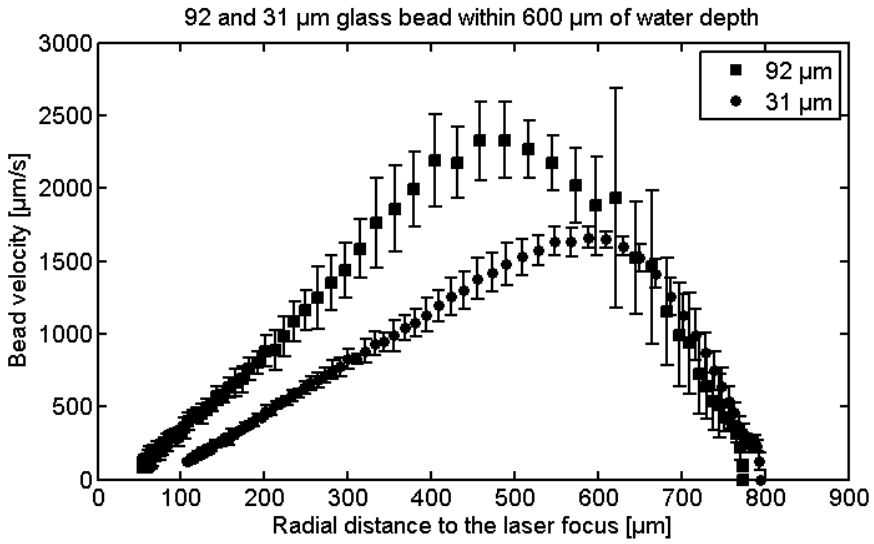

Figure 3.13: Velocity of glass beads with 92 and 31 μm in diameter for 600 μm water depth vs the radial distance to the laser focus. Error bar is calculated over ten measurements.

A comparison between the velocity fields of different bead sizes is depicted in Figure 3.12 for 450 μm water depth. It shows that the bead velocity depends on the bead size for a given water depth (450 μm). Naturally, the drag force is also larger. A larger bead will also be heavier. However, at this scale surface effects are dominant over inertial effects and the flow has a greater surface area to push against. For smaller beads, there is a smaller contact surface area with the flow and they may become totally immersed in the boundary layer, decreasing significantly their velocity.

Figure 3.13 shows the velocity profiles for beads of 92 and 31 μm in diameter (the largest and smallest beads used for these measurements) in a water depth of 600 μm. The error bar is calculated as the standard deviation over ten measurements. The errors are larger for higher velocities. These errors are due to the bead initial positions with respect to the laser focal point.

Figure 3.14 illustrates the maximum bead velocity for different bead sizes, 31, 45, 62, 71, 79 and 92 μm in diameter, in three different water depths 375, 450 and 600 μm, respectively. Notice that in all cases, the maximum velocity increases while decreasing the water depth. For a given depth, considering all the different bead sizes, the maximum bead velocity tends to decrease as bead size get smaller. The water depth are increased by 75 μm and then 150 μm from 375 μm, to reach 450 and 600 μm. By taking the maximum peak velocity for 375 μm of water depth as

reference, a 92-micron bead exhibits a speed decrease of 21% and 54.8% as water depth increases from 375 μm to 450 μm and 600 μm respectively. The velocity decrease is about 2.6 times when reducing the water depth by a factor of 2 (150 μm).
For a 31μm bead the speed decreases were about 16.8% and 42.4%. For a 71 μm bead, the velocity decrease is about 3 times. From Figure 3.14, one can conclude that if the water depth is increased by a factor of 2, the velocity for a constant bead size decreases between 2.5 to 3 times.

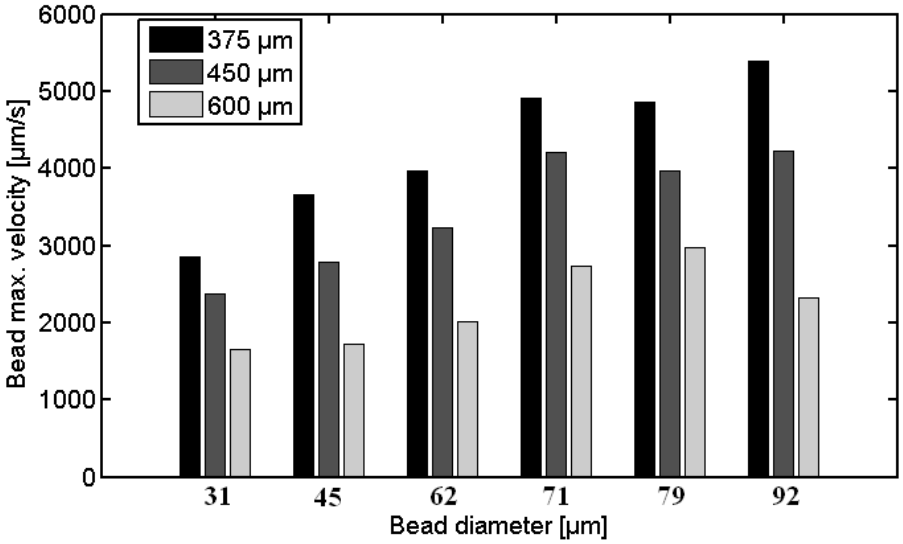

Figure 3.14: Peak velocity of glass beads 31, 62, 71, 79, 92μm in diameter respectively for three different water depth of 375, 450, 600μm.

As shown in Figure 3.15, the velocity profile of a thin liquid layer locally heated from below has a pair of counter subsurface convection flows. Close to the free surface, flows are directed away from the heat source, and toward the reservoir surface flows are directed toward the heat source. Hence, convection flows reverse their direction from the top (top subsurface flow: TSF) toward the bottom (bottom subsurface flow: BSF) at a given depth. At this position, flows are almost null.

As seen previously, a bead velocity increases with the bead size. It would reach its maximum velocity if the bead size is exactly the dimension of the BSF depth, as the whole BSF velocity profile would drag the bead. However, if the bead size is larger than the BSF depth, it is expected that the velocity decreases because of the counter flows in TSF region.

3.3.3 Influence of larger beads

Velocity measurements on a 240 μm in diameter glass bead are presented in Figure 3.16. A larger bead size is selected to find the decrease of the bead velocity by decreasing the water depth. The bead is placed at about 550 μm from the laser focus. The laser is then switched on during 100 ms. Three different water depths are investigated, 250, 300 and 450 μm.
As compared to previous results, the bead velocity increases by decreasing the water depth from 450 to 300 μm. Maximum velocity values range from 4.3 mm/s to 6 mm/s. Therefore, the distance covered by the bead increases while decreasing the water depth. For 300 μm the

distance covered is 270 μm and for 450 μm, a distance of 220 μm is measured as the fluid velocity for a smaller water depth is larger.
On the contrary, when the water depth is almost identical to the bead size, the bead velocity decreases, as in the case of 250 μm water depth and a 240 μm bead. The counter TSF flow acts also on the bead's top part, diminishing drastically its velocity. In this case, a maximum velocity of about 1.8 mm/s is found and the distance covered by the bead center of mass is about 80 μm.

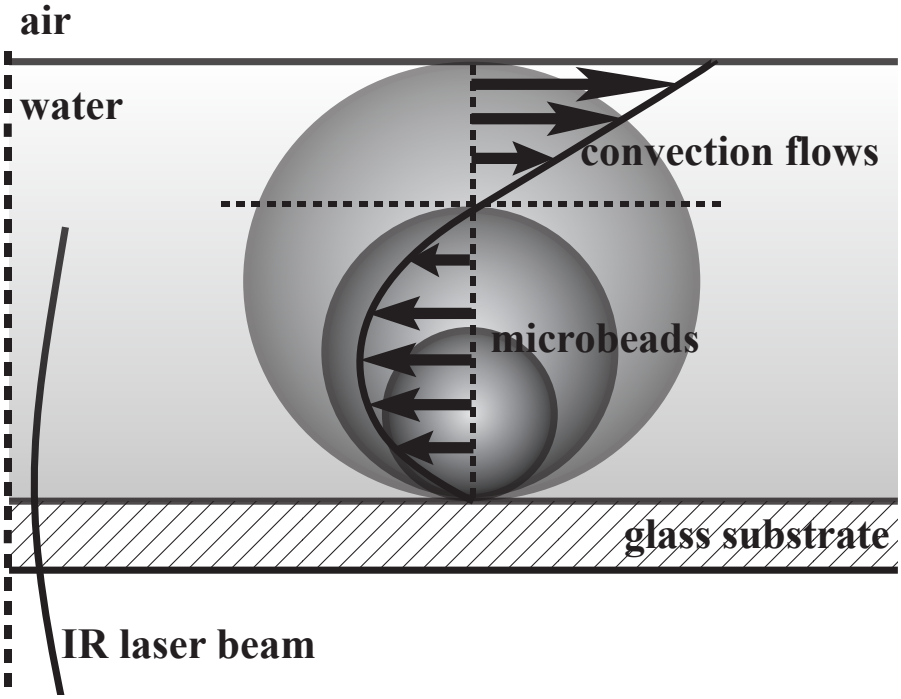

Figure 3.15: Illustration of the fluid velocity profile with respect to microbeads size. Around the free surface, flows go away from the heat source (IR laser beam), around the reservoir bottom surface flows are directed toward the laser beam. Keeping the water depth constant, a microbead can be dragged either by the bottom subsurface flows or also by the top subsurface flows.

3.3.4 Micro-objects floating on the water-air interface

As the top subsurface flows (TSF) is directed away from the heat source, micro-objects remaining at the free surface are repelled from the heat source. However, when the bead size becomes larger than the TSF depth, the the bottom subsurface (BSF) acts also on the microbead. Hence, for a given floating micro-bead size, it can be dragged toward the heat source, when the influence of the BSF over the bead become larger than the TSF influence (cf. Figure 3.17).

Figure 3.17 depicts the convection flows velocity profile with respect to a floating microbead size. For a constant water depth, a floating microbead can be dragged away from the heat source or toward the heat source, depending on its size.

Figure 3.18 shows an image sequence of a floating glass bead in motion. The bead size is 180 μm in diameter. Each image is taken at 33.3 ms of intervals. The position of the IR laser shot is represented by the white region. At water depth 450 μm it is observed that the bead goes away from the laser beam. It means that the TSF are dominant over the BSF, or the bead

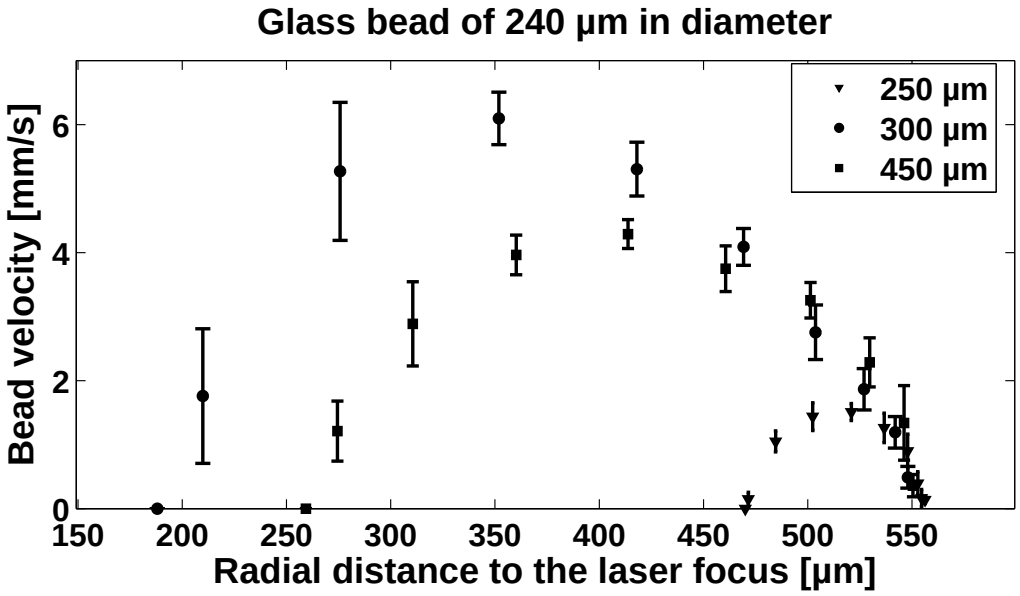

Figure 3.16: Velocity profile of a 240 μm glass bead for 250, 300 and 450 μm of water depth. The bead is placed at about 550 μm from the laser focal point. The laser is switched on during 100 ms.

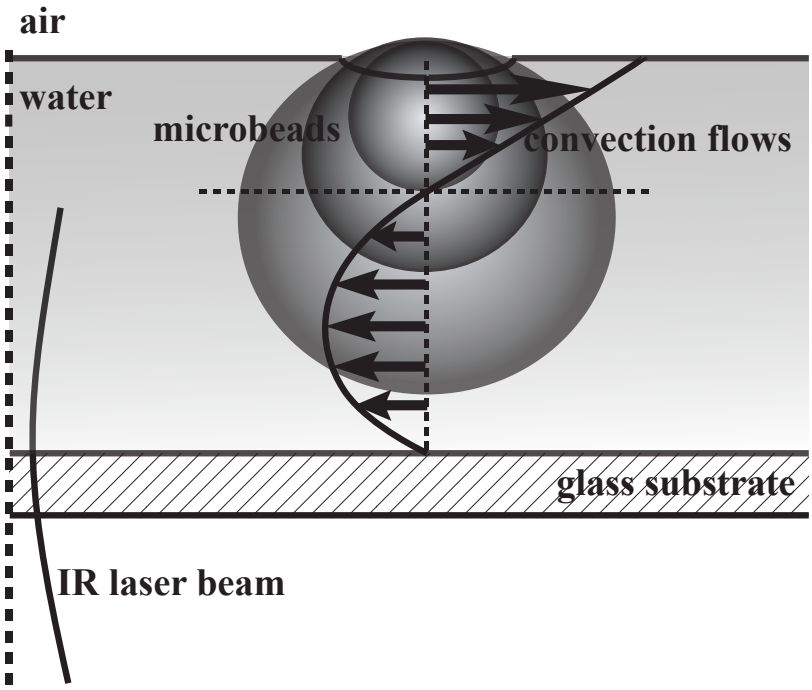

Figure 3.17: Illustration of the convection flow profile with respect to floating microbeads in a thin water layer. If a microbead bead size is comprised within the top subsurface flows (TSF), the bead is pushed away from the heat source. For a much larger microbead, the bottom subsurface (BSF) flows acts also the bead and this one is dragged toward the laser beam.

is only subject to the TSF.
When the water depth is reduced from 450 to 375, 300 and 265 μm, at 300 μm the bead velocity is diminished significantly, meaning that there was no dominance observed between TSF and BSF. At d=265 μm, the bead goes toward the laser beam as observed in Figure 3.18b. In this case, the BSF is dominant over the TSF.
For a bead of 270 μm in diameter at d=750 μm the bead is pushed away from the laser, at 500 μm it remains almost static, and finally at 450 μm is dragged toward the laser beam.

With these localized convection flows, it is hence possible not only to manipulate immersed micro-object but also floating beads. As observed, it is much more controllable to drag floating beads toward the heat source than away from it. In this configuration, the bead is attracted to the laser remaining close to it. However, this kind of trapping scheme has not been investigated in this work.

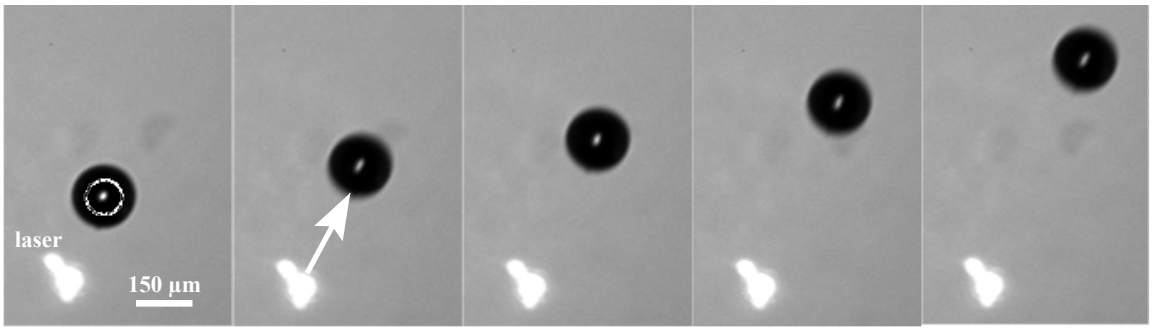

(a)

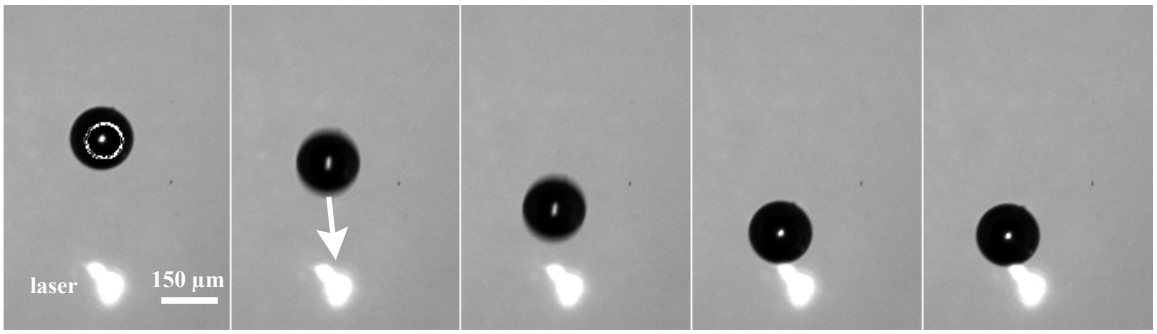

(b)

Figure 3.18: Image sequence showing the displacement of a floating glass bead of 180 μm in diameter. The dashed circles illustrate the bead-air interface. The white region is a focused red laser and indicates the IR laser shot. Every image is shown at intervals of 33.3 ms. (a) The microbead goes away from laser beam within 450 μm in water depth. (b) The microbead goes toward the laser bead within 265 μm in water depth.

3.3.5 Estimation of the manipulation force

In the proposed convection flow based manipulation process, the motion of microparts in the liquid is due to the motion of the liquid around which exerts a viscous force on them. This force is naturally proportional to the velocity difference between the flow and the object, hence is limited by the maximum velocity of the liquid. Thus, the evaluation of the manipulation force

requires to define the velocity profile of the convection flow.

In order to estimate the fluid velocity profile that drags a spherical beads and supposing that the immersed beads remain on the substrate surface, a rolling with sliding model is considered. It is assumed that the spherical bead and the horizontal plane are rigid and non-deformable

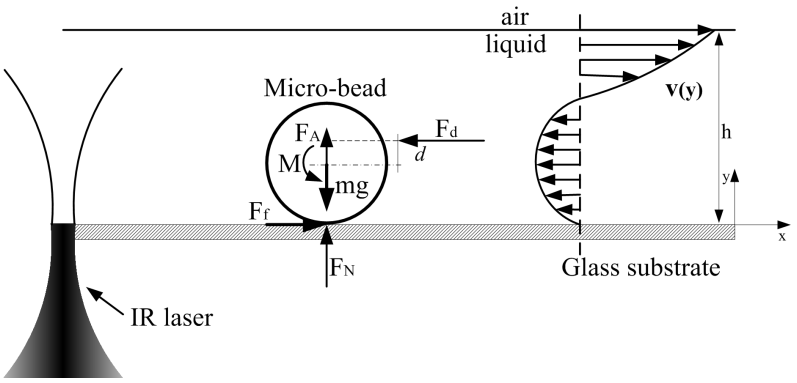

Figure 3.19: Schematic of the forces involved for the estimation of the fluidic forces exerted on a spherical microbead within a liquid medium.

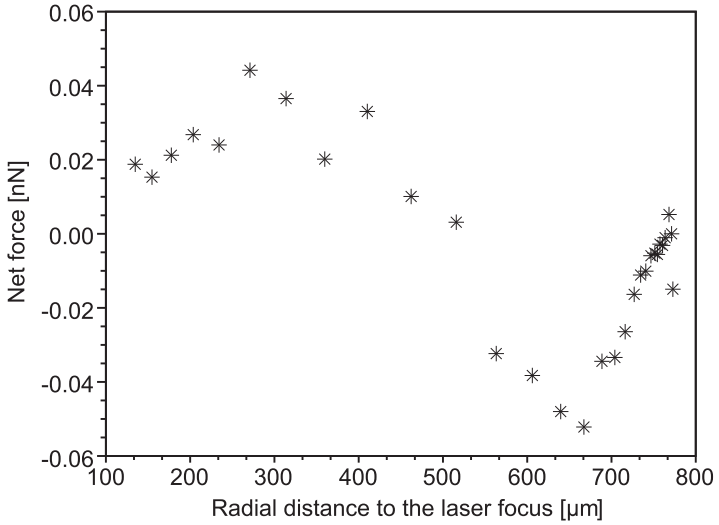

Figure 3.20: Net force computed with the bead center of mass acceleration (cf. Eq. 3.1). A glass bead of 92 μm in diameter is used within 450 μm in water depth. The acceleration data is taken by deriving twice the bead position.

bodies. The micro-sphere is uniform of mass m and radius R.

The dynamic equations that describe the motion of the bead can be written as:

$$\sum F = ma_{cm}, \tag{3.1}$$

$$\sum M = I_{cm}\alpha, \tag{3.2}$$

where a_{cm} is the acceleration of the bead center of mass, I_{cm} ($2/5mR^2$ for a sphere) is the moment of inertia about an axis through the center of mass, M is the resultant torque, F is the net force and α is the angular acceleration. a_{cm} is computed from Figure 3.12, by derivation of the velocity data with a time step of 1/80 s. The net force F is then calculated multiplying a_{cm} by the mass of the bead (see Figure 3.20).
Althought it is observed that the bead rolls while moving, only the motion due to the linear acceleration of the bead is considered here as a first approximation. The moment equation is not analyzed.

Based on these equations, a force analysis on a bead gives the following set of equations (a schematic of this analysis is shown in Figure 3.19). The net force is the sum of the viscous drag force exerted by the fluid and the friction.

$$F = F_d - F_f, \tag{3.3}$$

where F_d is considered the viscous force applied on the bead and F_f is the friction force opposing the bead motion.
As the motion is rolling with sliding, the friction force is a kinematic friction force:

$$F_f = \mu_k F_N, \tag{3.4}$$

where μ_k is the coefficient of kinematic friction between the two surfaces and F_N is the normal force exerted on the bead. This latter force is equal to the difference between the bead weight and the Archimedes force $F_A = \rho g V_{volb}$, where ρ is the water density, g is the acceleration of gravity and V_{volb} is the bead volume.
Therefore the force equation on the vertical axis is:

$$F_N = mg - F_A. \tag{3.5}$$

The mass of the bead is $m = \rho_b V_{volb}$ where ρ_b is the density of glass (2500 Kg/m^3) and $V_{volb} = 4/3\pi R^3$.

The coefficient of kinematic friction for a glass-glass relative motion within water medium is $\mu_k = 0.2$ (Ishibashi *et al.*, 1994).

As the acceleration is measured through velocity, and the mass of the bead is known, the viscous force applied on the object can be written as:

$$F_d = ma_{cm} + F_f \tag{3.6}$$

F_d is due to the relative velocity between the spherical bead and the convection flow:

$$F_d = A(v_f - v_b), \tag{3.7}$$

where A is the drag coefficient in low Reynolds Stokes flow for a spherical shape: $A = 6\pi\mu R$, v_f is the velocity of the fluid and v_b is the velocity of the bead (cf. Figure 3.12).

Hence, using equations 3.6 and 3.7 v_f can be expressed as:

$$v_f = \frac{ma_{cm} + F_f + Av_b}{A} \tag{3.8}$$

These results are reported in Figures 3.21 and 3.22 for the force due to flows speed and the estimated speed of flows respectively.

The maximum force that can be exerted on the bead is naturally located at the maximum flow velocity point. It appears that with convection flows, significant forces can be exerted. For instance, these forces are much larger than optical tweezers forces: 5 nN vs tens of pN.

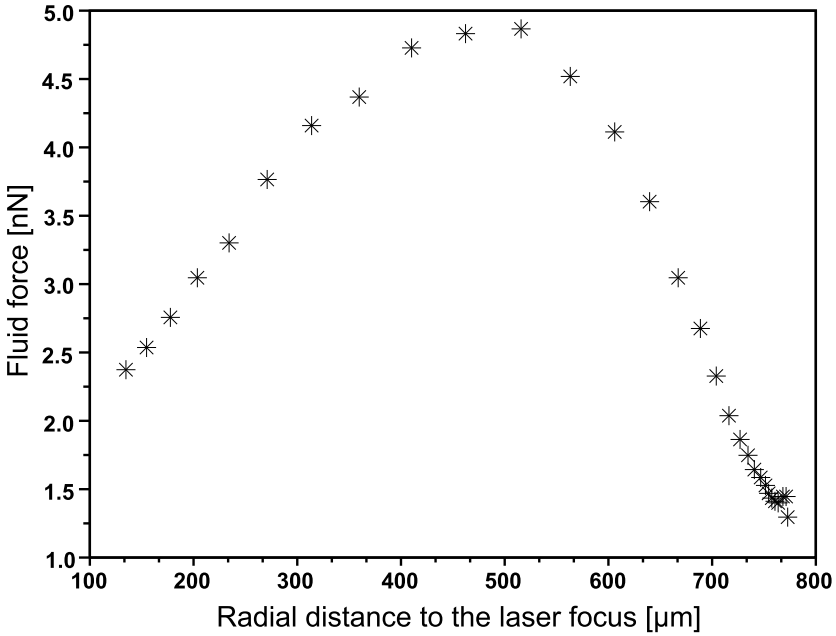

Figure 3.21: Estimation of the force that the flows exerted on a 92μm-sized glass according to Eq. 3.8.

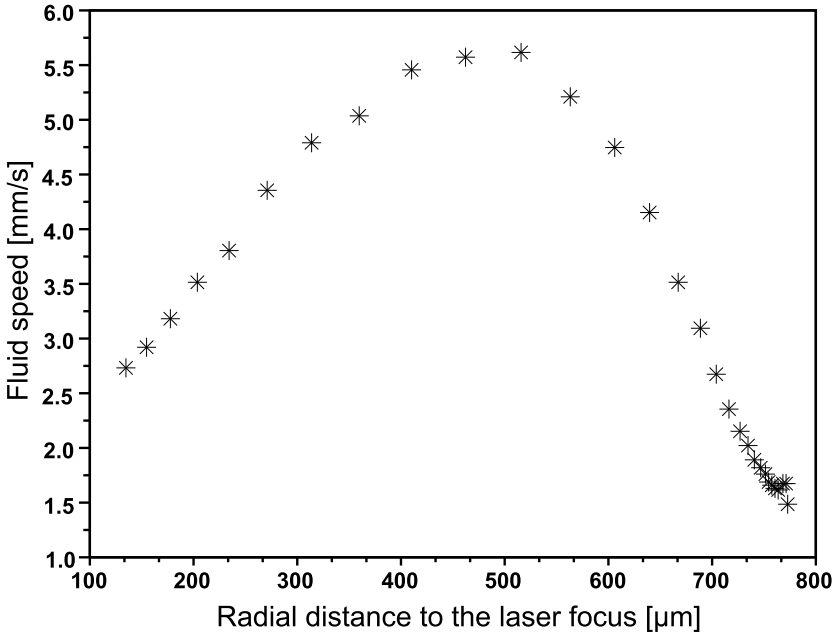

Figure 3.22: Estimation of the flows velocity distribution that drags a 92μm-sized glass immersed in a water depth of 450 μm according to Eq. 3.8.

3.4 Conclusions

An experimental set-up have been developed in order to generate thermocapillary convection flows which are used to drag micro-parts. A focused 1480 nm IR laser was used to locally heat a thin liquid layer of distilled water and to generate localized convection flow.

This permitted manipulation without the need for patterned or microfabricated substrates. A simple petri dish was filled with liquid water to a predetermined depth.
Velocity measurements of glass beads (ranging from 31 to 92μm in diameter) were performed with a high speed CMOS camera. Results showed that the largest glass bead (92μm in diameter) was dragged at about 5.5 mm/s in 375μm water depth. It appeared that the bead velocity depends on the bead size. The larger the size, the larger the velocity, because the flow velocity profile on its surface is larger. For smaller beads, the velocity profile decreases due to the boundary layer at the substrate-water interface.
The bead velocities also depend on water depth; the smaller the water depth, the higher the bead velocity. The manipulation velocity could be controlled to handle particles by adjusting the water depth.

Also, a force model is proposed in order to estimate the exerted forces by the flows on the beads. It appears that it is possible to exert forces approximatly 100 larger than optical tweezers.

Chapter 4

Toward a fully automated vision-based opto-fluidic system for non-contact micromanipulation

> There is a computer disease that anybody who works with computers knows about. It's a very serious disease and it interferes completely with the work. The trouble with computers is that you 'play' with them!
>
> Richard P. Feynman

The growing development and production of microsystems in both the industrial and research field requires versatile and high-autonomous micromanipulation systems. The increase in the diversification, therefore in complexity, of these systems such as MEMS, NEMS, MOEMS and recently bioMEMS, needs the use of different and several microfabrication processes to engineer microcomponents. And these components, made of different geometries, materials and properties, have to be assemble to form microsystems for a wide variety of applications. Due to the potential market of these micro and nano devices, industries need to improve their throughput. Indeed, the micromanipulation and assembly of these components rely on operators limiting large production. However, with autonomous micromanipulation and assembly systems high-throughput and cost-effective devices could be carried out. Moreover, more precise and reliable manipulation and assembly could be achieved.

This field is rapidly progressing as autonomous micromanipulation is of great interest nowadays. Several research groups are working on micromanipulation systems. Most of works are based on mechanical or contact micromanipulation mode (Dionnet *et al.*, 2004, Sitti & Hashimoto, 2000, Probst *et al.*, 2009). However, contact micromanipulation is a slow process that does not allow parallel manipulation capabilities due to the limited displacement speed of the microtools (tens of microns per second).

Among non-contact micromanipulation systems, optical tweezers have reached a high degree of autonomy (Tanaka *et al.*, 2008, Arai *et al.*, 2004). Nevertheless, this technique is limited to objects up to tens of microns in size.

Autonomous micromanipulation is also of interest in biology and the manipulation of living cells such as bacterias and embryos (Yu & Nelson, 2001).

In the previous chapter, it has been demonstrated that convection flows induced by a laser can be successfully used to displace microscopic particles in a liquid medium. In order to automate this novel manipulation method, it is necessary to implement a closed loop feedback mechanism. The chosen feedback is vision through optical microscope. Several image processing methods are first evaluated in order to implement the most adapted to the system. Then the calibration of the micromanipulation system is detailed, followed by the operation modes developed.

4.1 Vision feedback for micromanipulation

Vision feedback is widely used for robotic manipulation, especially in the macroscale where cameras can be easily used as optical sensors.
In the microscale the use of vision feedback is attractive because of the lack of alternative sensing systems. Optical microscopes are coupled to a camera to provide a visual feedback to the user or a position information to microrobotic systems.
In nanomanipulation, due to the limited optical resolution, other instruments are used for position feedback such as a Scanning Electron Microscope (SEM). Even hybrid systems (optical microscope-SEM) can be used for a 3D micro/nanomanipulation (Jähnisch & Fatikow, 2007).

This section addresses different methods in vision feedback using image processing for microscopic applications in order to select the most adapted to our system. Image processing will allow to calibrate the system and to track the moving particles. For calibration, the detection of the IR laser position on the sample is needed. For tracking, a robust and fast method is required.

4.1.1 Optical flow

This method is used to estimate the relative motion of features in an image at time t with respect to an image at time $t+\delta t$. It is based on the smooth intensity variation of these features between two successive images, $I(x, y, t)$ and $I(x + \delta x, y + \delta y, t + \delta t)$. Moreover, the feature motion between two images is assumed to be very small in order to obtain:

$$\frac{\delta I}{\delta x}V_x + \frac{\delta I}{\delta y}V_y = -\frac{I}{t},$$

where V_x and V_y are the optical flow velocity of $I(x, y, t)$. In microscopic environments where the illumination and environment are well controlled, this method is proved to be robust.
As an example, (Yu & Nelson, 2002) uses an optical flow tracking algorithm for visual servoing of a microrobotics system. A tip of an injection pipette is tracked to inject foreign genetic material into cells.

4.1.2 Image segmentation

Segmentation is widely used from microscopic detection to vision-based robot control. It is an image process that partitions an image into homogeneous non-intersected features in which connected pixels are labeled.

There are different techniques to implement image segmentation such as histogram thresholding and edge detection (other approach can be used (Pal & Pal, 1993)).

Histogram thresholding is one of the simple and popular image segmentation techniques where a gray level information is used. Thresholding techniques can be classified as global thresholding and local thresholding. When only a threshold is used for the whole image, it is global thresholding. When an image is partitioned into several subregions, several thresholds are necessary for each region, it is local thresholding or also called adaptive thresholding. In case where an image is partitioned into two regions, black and white, it is called bilevel thresholding.
Edge detection can also be used for image segmentation. Features are obtained by detecting a strong gray level gradient at the object's borders. Methods such as Sobel gradient and Laplacian operator are generally used. The Sobel's operator is a first differential operator with a very good immunity to noise. On the other hand, the Laplacian operator is a second differential operator and responds strongly to corners, lines, and isolated points. However, it is heavily influenced by noisy images.

(Chen *et al.*, 2006) showed the use of advanced segmentation techniques such as the Watershed segmentation to detect and track individual cells in a living cell population (cf. Figure 4.1).

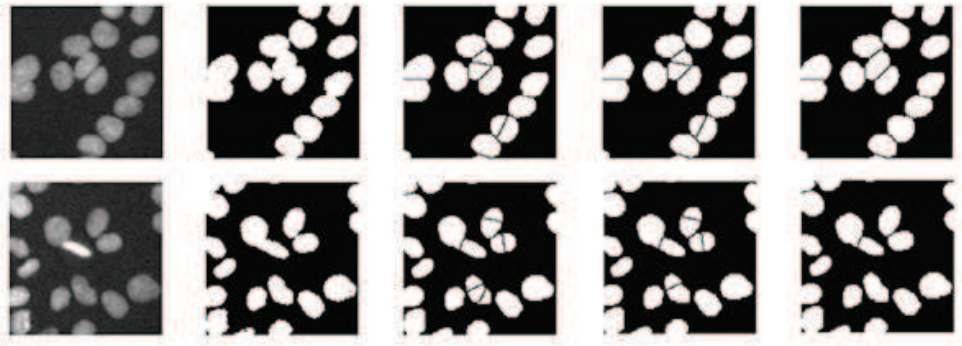

Figure 4.1: Image segmentation of cells (Chen *et al.*, 2006). It shows the separation of features with different advanced segmentation techniques

4.1.3 Hough transform

This method is most commonly used to detect lines and circles. It is a robust method when working under noisy conditions such as optical microscopes. Hough transform involves transforming each of a figure points in a parametric representation within a parametric space. For example, a line is represented by a point in its parametric space. In order to find a line in a picture, every point is transformed in its parametric representation. However, an infinity of lines can passes through a point, a family of lines. This family is represented by a sinusoidal curve in the parameter space. Hence two points have two sinusoidal representation, and the intersection point of these curves is the line passing through both points in the picture.
The Hough transformation has a generalized form, any shape of feature can be detected. However, the number of parameters increases with the complexity of the feature shape. Therefore, this method becomes time-consuming in computer vision.
This method was used by (Pawashe & Sitti, 2006 and Tanaka *et al.*, 2008) to detect micro-objects. (Pawashe & Sitti, 2006) performed automatic micromanipulation of sphere by a mechanical technique with vision feedback. (Tanaka *et al.*, 2008) used also image processing to automatically handle non-spherical micro-objects using optical tweezers.

Figure 4.2 shows the Hough transform used by (Pawashe & Sitti, 2006).

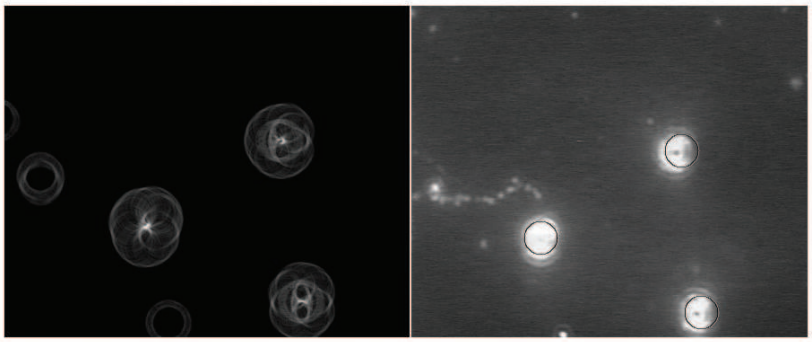

Figure 4.2: Micro-sphere detection using the Hough transform (Pawashe & Sitti, 2006). In the left hand side the parametric space is shown and in the right hand side the micro-spheres detected with its respective localization (drawn circles) are depicted.

4.1.4 Image correlation

Image correlation is a method to compute how much an image feature matches another. It is used to find the location of a feature in an image by comparing it with a template image. The template is overlaid on a region of interest by moving it pixel by pixel at one time. At each pixel position a correlation coefficient is computed. As a result a 2D matrix of coefficient values are obtained. The maximum coefficient of this matrix gives the center of the searched feature with a tolerance of one pixel. The correlation is also robust to noisy images.
This technique is commonly used in biology to track cells and study their behavior (Gelles *et al.*, 1998).
The normalized correlation coefficients are computed as follows (OpenCV library)[1]:

$$\mathbf{R}(x,y) = \frac{\Sigma_{x'}^{w}\Sigma_{y'}^{h}(\mathbf{T}(x^{'},y^{'}))(\mathbf{I}(x+x^{'},y+y^{'}))}{\sqrt{\Sigma_{x'}^{w}\Sigma_{y'}^{h}(\mathbf{T}(x',y'))^2\Sigma_{x'}^{w}\Sigma_{y'}^{h}(\mathbf{I}(x+x',y+y'))^2}},$$

where R is the correlation coefficients, w and h are the width and the height of the template image respectively, T is the template image, I is the search region of interest (ROI), $(x^{'},y^{'})$ and $(x+x^{'},y+y^{'})$ are the pixel positions in the respective images (template and search ROI). This gives a result between 0 and 1.

In Figure 4.3, an image correlation is shown. In order to track a bead, a template of this bead (inset: top right of the figure) is first captured. The template is then correlated with the image in order to calculate the correlation coefficients. The maximum coefficient gives the position of the bead (lightest dot in the bottom picture).

The following table gives a comparison between the image processing discussed.

From Table 4.1, segmentation is selected to detect and count the number of micro-objects in the sample. As the objects to be detected are well-contrasted with the background (cf. Figure 4.3), a segmentation can be easily applied using only a threshold. Moreover, segmentation allows to detect any object's shape (in contrast to the Hough transform). Segmentation is also

[1]Open Source Computer Vision. SourceForge.net, http://sourceforge.net/projects/opencvlibrary/.

Figure 4.3: Images of a correlation method applied to track a glass spherical bead. The bottom image is the result of the correlation method applied to the top image. In the top right corner the template is shown.

Table 4.1: Comparisons of image processing methods

Method	Robustness	time to process	feature detection
Optical flow	low	no so fast	bad
Segmentation	low	fast	good
Hough transform	high	no so fast	good for lines and circles
Correlation	high	fast if ROI very small	good. Template required

used to calibrate the system, where the laser position is required. This process is explained in the next section.
For the bead tracking process, correlation is preferred because it is robust, fast for small ROIs and accurate.

4.2 System calibration

The micromanipulation system has to be calibrated due to distortions introduced by the laser-scanner, in order to have a precise control on the beads positions.
This means that the laser, displaced by the tip/tilt scanner on the sample, is not projected exactly on the desired position. For instance, if a square reference is given to the scanner, on the sample this desired square trajectory of the laser is curved due to the scanner's distortions (see Figure 4.5). These distortions are explained in details in (Hafez, 2000).

To correct these distortions a third degree polynomial approximation is used in order to have:

$$x_{corrected} = a_x x + b_x y + c_x x^2 + d_x xy + e_x y^2 + f_x x^2 y + g_x x^3 + h_x y^2 x \tag{4.1a}$$

$$y_{corrected} = a_y x + b_y y + c_y x^2 + d_y xy + e_y y^2 + f_y x^2 y + g_y x^3 + h_y y^2 x \tag{4.1b}$$

where $x_{corrected}$ and $y_{corrected}$ are the corrected positions to be sent to the scanner command, x and y are the desired positions of the laser on the sample. To calculate the coefficients, at least eight positions values of x and y are required to obtain a system of eight equations and eight unknowns. The index 1 to 8 represent eight measurements of the laser positions. The resulting

equation system is as follows:

$$\underbrace{\begin{bmatrix} x_{1corrected} \\ \vdots \\ x_{8corrected} \end{bmatrix}}_{X} = \underbrace{\begin{bmatrix} x_1 & y_1 & x_1^2 & x_1y_1 & y_1^2 & x_1^2y_1 & x_1^3 & y_1^2x_1 \\ \vdots & & & & & & & \vdots \\ x_8 & y_8 & x_8^2 & x_8y_8 & y_8^2 & x_8^2y_8 & x_8^3 & y_8^2x_8 \end{bmatrix}}_{P} \times \underbrace{\begin{bmatrix} a_x \\ \vdots \\ h_x \end{bmatrix}}_{C}, \tag{4.2}$$

As C is the unknown, the inverse of P is calculated to obtain:

$$P^{-1}X = C \tag{4.3}$$

In Figure 4.4 the process where X, P and C intervene is shown.
In order to solve this system, a square reference composed of eight positions values is used for X (see the square marks in Figure 4.5). The values of P, the eight laser positions that correspond to the command reference X, are captured by a camera and calculated by image segmentation (see Figure 4.6). The IR laser causes a circular shadow in the water layer, this shadow is detected with image background subtraction. It means that, an image of the sample without laser is first captured with a camera. The laser is then shot into its respective reference position in order to capture a second image containing the IR laser's shadow. By subtracting both images, only the IR shadow is obtained (cf. Figure 4.6a). The center of the shadow, center of the IR laser, is computed with image segmentation using thresholding (see Figure 4.6b).
P is then calculated with the eight laser's positions, X is the command reference and C is calculated according to Eq. 4.3.
C is used to correct the desired positions and compute a new command reference for the scanner. For instance, if a line trajectory of the laser is desired (square marks in Figure 4.7), a curve reference trajectory has to be sent to the scanner according to Eq. 4.1 (circle marks in Figure 4.7).

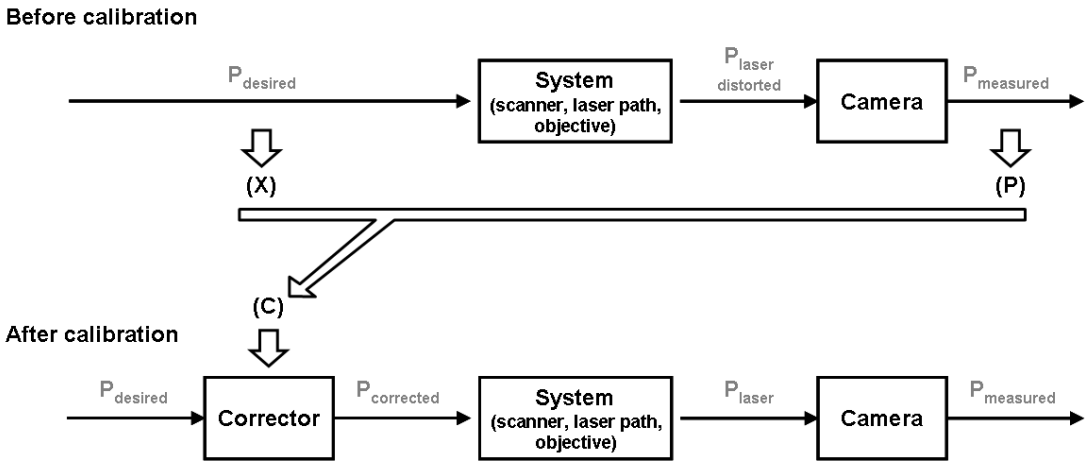

Figure 4.4: Block schemes illustrating the calibration process where the polynomial approximation is used.

A flow chart for the calibration process is shown in Figure 4.8. Eight reference positions are sent to the laser, at each position the laser is detected using image processing and its center is calculated. This is performed consecutively for the eight reference positions. Once the laser' positions computed, the coefficients for the polynomial approximation are calculated.

The calibration process allows to have a precise control on the bead's positions, thus the manipulation system is implemented in two operation modes: manual and automatic.

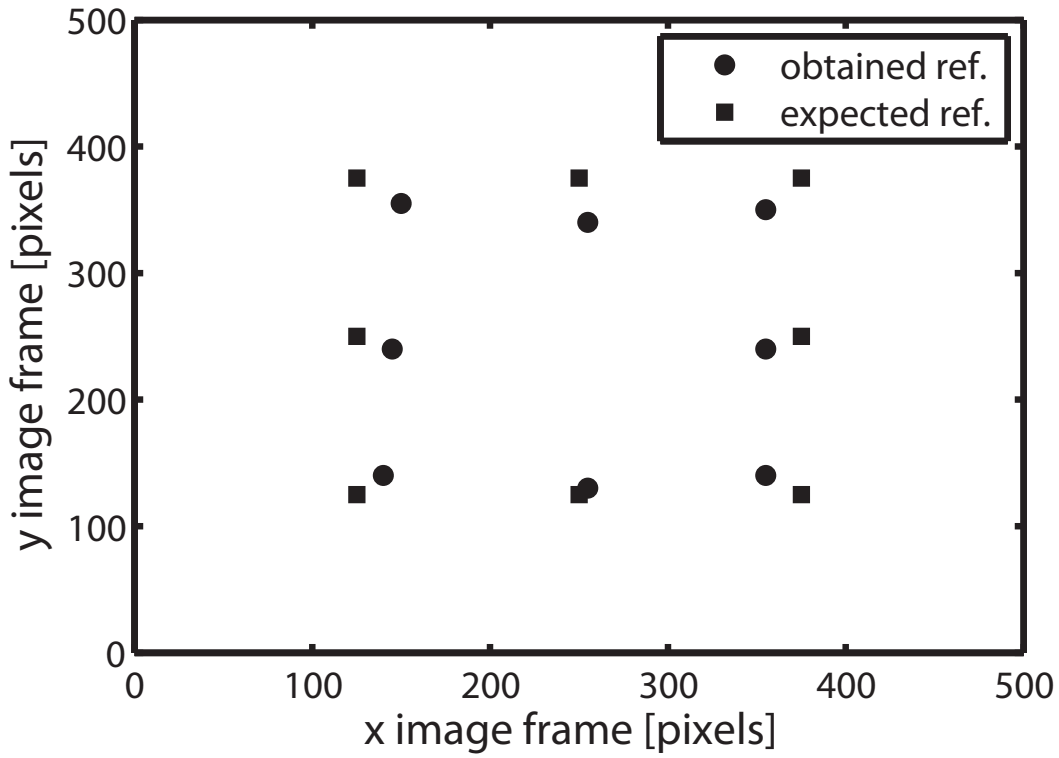

Figure 4.5: Simulation of geometrical distortions. If a square reference is sent to the laser scanner, a curve quadrilateral is obtained on the sample due to the scanner's distortions.

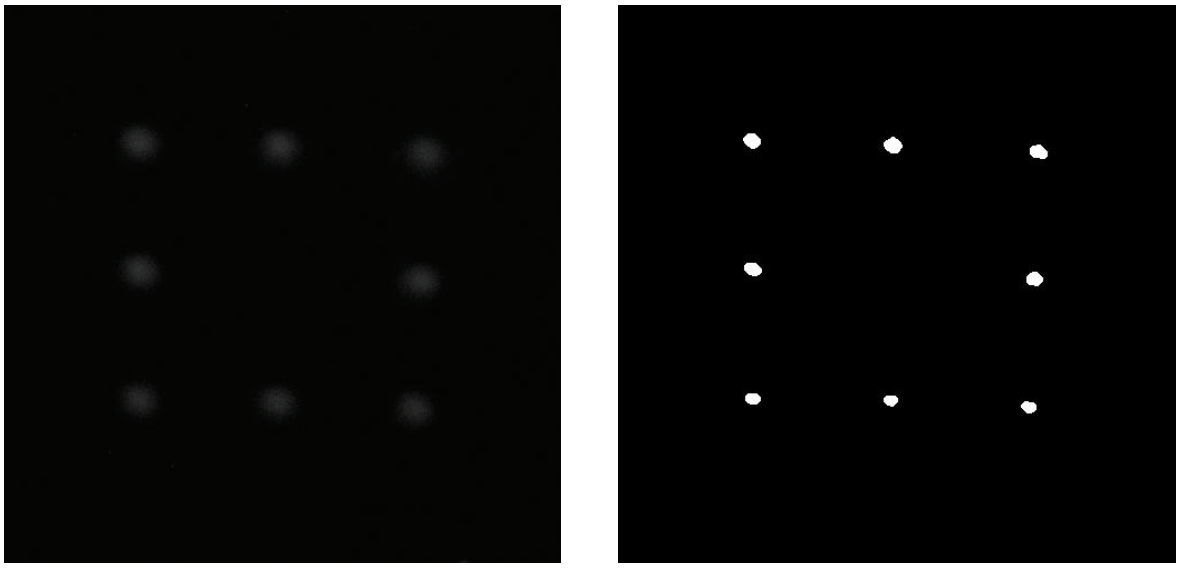

(a) (b)

Figure 4.6: Superposition of eight images containing the reference laser positions on the sample. (a) Background image subtraction to detect the IR laser positions. (b) Image binarization of each point found after background subtraction. Then morphological operations are used to improve the image quality. Computation of the objects' center of mass using OpenCV.

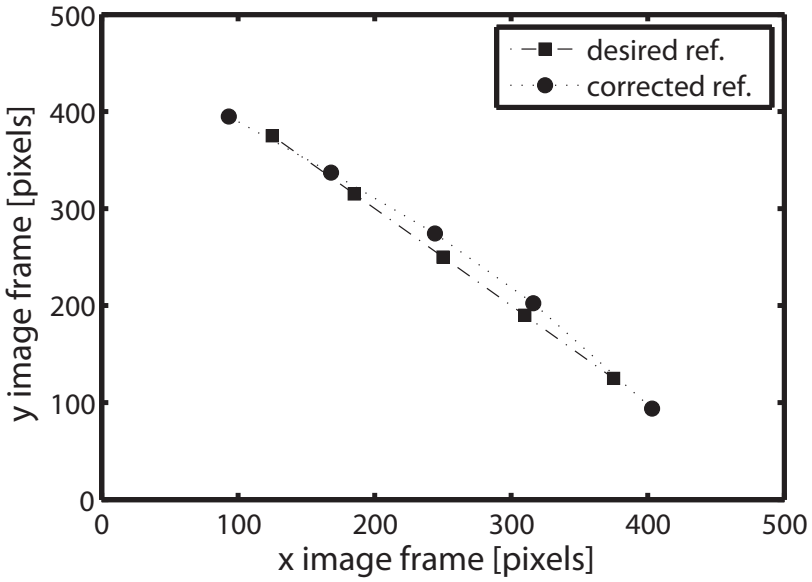

Figure 4.7: The calibration process allows to obtain a line reference on the sample (square marks) by sending a curve trajectory (circle marks) to the laser scanner. This curve is determined by a polynomial approximation.

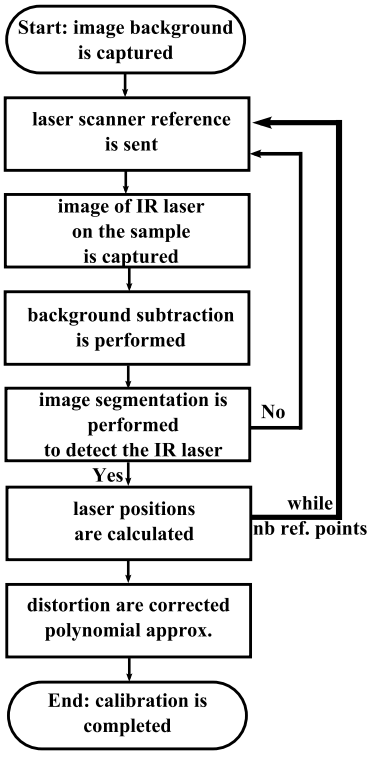

Figure 4.8: Flow chart illustrating the system calibration process.

4.3 Micromanipulation: Operation modes

Two operation modes have been implemented with a C++ program:

1. A manual operation mode, in order to handle different micro-parts such as spherical beads, silicon cubes solder beads and capacitors to move them in desired positions. In this mode, the user, through a computer mouse, addresses the laser at a target position within the image frame to drag the micro-objects toward this position in the workspace.

2. An automatic operation mode, in order to handle multiple beads autonomously. In this case, a reference position value is introduced in the program. The laser is then automatically addressed to a determined position close to the bead to drag it toward their final positions.

4.3.1 Manual operation mode

A manual micromanipulation mode is first implemented, in which the user can drag different types of beads such as glass beads, silicon microcubes, solder beads and capacitors.
The user controls the laser-scanner displacement by moving a computer mouse onto the video frame displayed on a Graphical User Interface (GUI). The user can shoot the IR laser at a desired position by pressing the mouse's left button. The laser exposure time is a parameter that can be changed in the computer program.
The user has to manage to shoot the laser at a distance from the micro-object in order to drag it. As seen in chapter 3, the beads go faster when the laser is irradiated at a predetermined distance from the beads. The bead velocity depends on this distance and the exposure time.
The only feedback that the user have is the video frame displayed on the computer screen. The user has to correct the laser position with respect to the micro-part position by looking at the computer screen.

Figure 4.9 illustrates the overview of the manual operation mode. The user controls the laser position and laser exposure time with the computer mouse. When a mouse click is performed, the mouse position in pixels is introduced in the program. The laser-scanner and IR laser are then actuated and pointed at the mouse position. The user has to see the bead position and to displace the IR laser with respect to the bead in order to drag it close to the desired position destination.

This manipulation mode is used to handle spherical beads and larger and heavier non-spherical parts. In the case of heavier micro-parts, acoustic vibrations are applied to the substrate in order to break the adhesion forces between the parts and the substrate.

Handling of spherical beads

The handling of spherical beads is shown in Figure 4.10. In the first sequence of pictures, the separation of three beads previously in contact and placing them at different positions is performed. The bead sizes lie between 75 up to 85 μm in diameter. They are immersed in distilled a water depth of 300 μm. Pictures are taken every 8 seconds. The bead speeds are in the range of 1 to 3 mm/s. The red dot is the position of the IR laser. Manipulation is simply made by moving the laser focal point with the mouse and by clicking to apply a 20 to 100 ms of the IR laser (cf. Figure 4.10a). The user has to point the laser at a suitable position with respect to the beads in order to handle them with a desired speed. In addition, the user has to deal with

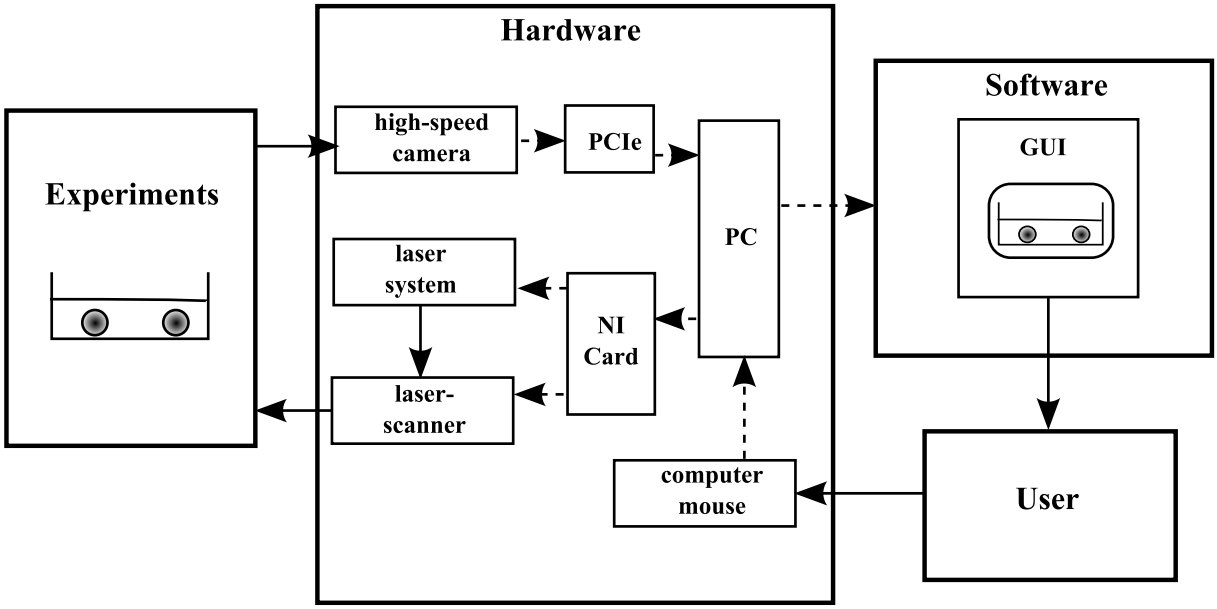

Figure 4.9: Representation scheme of the manual operation mode.

the displacements of the beads at the same time for one laser shot.

The manipulation of beads by scanning the laser in a circular pattern was successfully performed. The particles are in this case trapped in the middle of the circle. This result is interesting because the particle stays away from the laser irradiation. Also, we observed that the micro-objects trapped this way tend to rotate at a slow speed. The direction of the rotation can be controlled by the direction of the laser rotation. This feature may be use for precise positioning either in translation or rotation. Figure 4.10b shows three beads, ranging from 75 to 85 μm in diameter, trapped in the center of a circular laser pattern. A circular pattern is projected on the working surface to trap the objects. The objects remain in the center due to the radial flows acting in them.
Parallel manipulation of beads was also demonstrated using a linear scanning of the laser. In this case the beads follow the laser line in an aligned formation.

Handling of non-spherical micro-parts

Different micropart shapes can be also dragged. Figure 4.12a shows the drag of a silicon micro-cube of 100 μm in side. It is immersed in a PBS solution of 400 μm in depth. The white dot shows the laser position. A speed of 800 μm/s can be reached. Even if the micro-cube has a much larger surface of contact with the substrate and it does not roll, it can be dragged easily at a reasonably high-speed.

In Figure 4.12b, silicon parts of about 200 μm of maximum size are dragged. They are large particles with a non-defined geometrical shape. They are also very thin, about 20 to 30 μm in thickness. In this case, the current affecting the object is quite low because of the boundary layer of the liquid flow. However, they are quite easily manipulated. They are actually trapped in the recirculation zone spinning at the speed of the flows. Figure 4.12b shows a task consisting of bringing all the parts together. Total manipulation time is 20 seconds. The water depth is 300 μm.

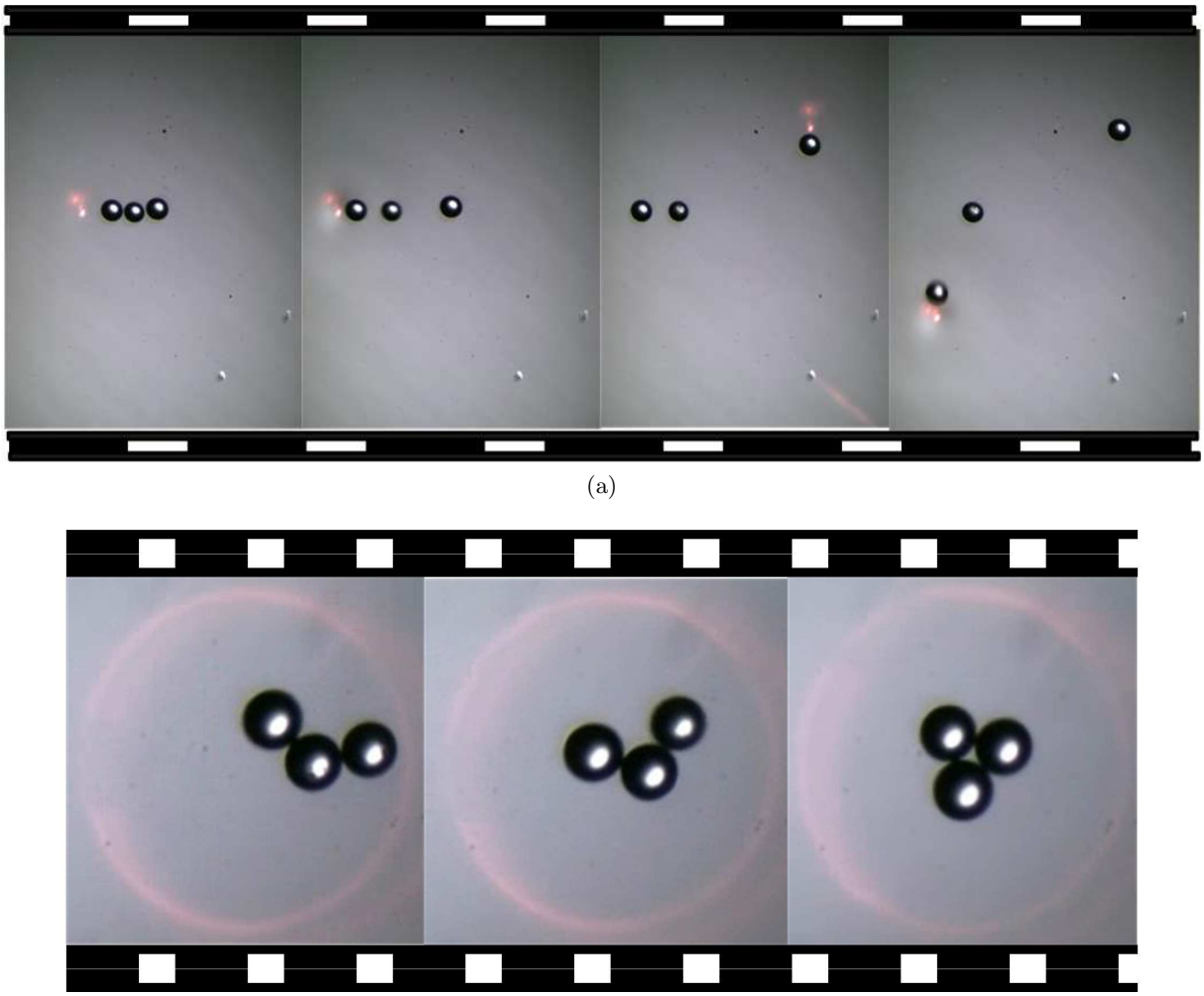

Figure 4.10: Pictures depicting the manipulation of beads. (a) Separation of three beads of 75 to 85 μm in diameter. The red dot is the laser position. b) Trapping of micro-spheres inside a laser circular pattern. Glass beads of 75 to 85 μm in diameter.

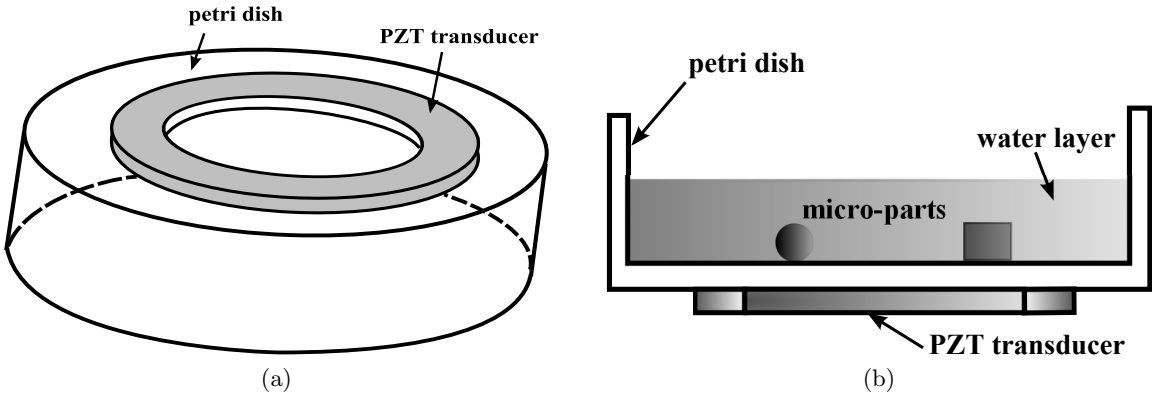

Figure 4.11: Annular PZT piezo-transducer is glued on a petri dish. It engenders acoustic vibrations to push the micro-parts up from the substrate. (a) View of the petri dish bottom surface. (b) Side view of petri dish and transducer.

The strong dynamics of these flows allow to drag much larger and heavier microparts. Some examples are solder beads and microcapacitors. However, for these cases, an annular PZT transducer is used to engender acoustic vibrations in the substrate in order to reduce the adhesion forces. This transducer is glued on the petri dish substrate as shown in Figure 4.11.
Figure 4.13a depicts the handling of a lead-tin solder bead of about 200 μm in diameter. This bead has not a spherical shape, increasing significantly the contact area with the substrate. In this case, the flows are not able to drag the solder bead because of the adhesion forces with the substrate. To drag this object, acoustic waves are used to reduce the adhesion forces in such a way that the solder bead is pushed up from the substrate due to acoustic vibrations. The manipulation is slow, each of the pictures are shown at an interval of 1.6 s.

Figure 4.13b shows the manipulation of a micro-capacitor within 300 μm in water depth. Its dimensions are 400 $\times$ 200 $\times$ 50 μm^3. To drag this capacitor, the same PZT transducer is used. The transducer is actuated with a swept back and forth signal from 20 kHz to 150 kHz in 50 ms with an amplitude of 5 V peak-to-peak.
The measured manipulation speed is between 20 to 50 μm/s. Each image is shown at an interval of 4 s.

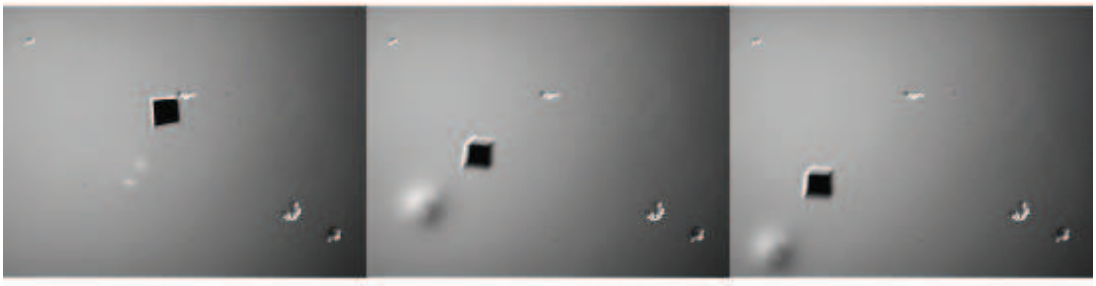

(a)

(b)

Figure 4.12: Manipulation of non-spherical parts. (a) Silicon cubes of 100 μm in size are dragged. (b) Silicon parts of 200 μm as maximum side are being grouped. The white dot is the laser position.

The manual operation mode does not allow to handle multiple micro-beads in a fast and precise manner. On the other hand, an automatic operation mode has been implemented to allow a fast and accurate multiple bead manipulation.

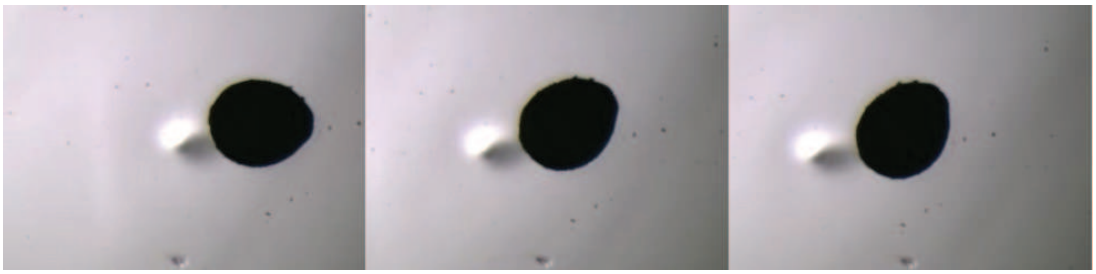

(a)

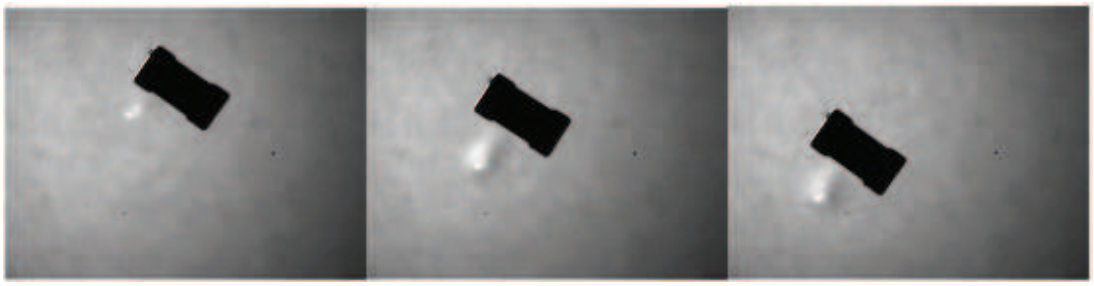

(b)

Figure 4.13: Pictures depicting the manipulation of large and heavy micro-parts. (a) Lead-tin solder bead of 200 μm in diameter is dragged. (b) Manipulation of a capacitor of 400 $\times$ 200 $\times$ 50 μm^3 in size. A PZT transducer is used to reduce the adhesions forces with the glass substrate.

4.3.2 Automatic operation mode

Automatic systems for micromanipulation are of great interest in the microtechnology and biology industry or in the research field. It can provide precision, accuracy, massive manipulation and therefore cost-effective production. It can also reduce significantly the time-consuming process of manual operation modes. Even in the research laboratories it is of great interest to be equipped with automatic manipulation to test or asses several micro-processes in a more reduced time such as self-assembly, mixing chemical components, gathering or sorting micro-parts.

In this section, the automation of the micromanipulation system is presented. This is possible due to the predictable convection flows behavior described in chapter 3 and the negligible inertial effects.
As an example of automatic manipulation, the handling of two glass spherical beads ranging from 30 to 90 μm in diameter are reported. Additionally, with the algorithm discussed below, spherical beads up to 300 μm can be automatically manipulated.

Algorithm for automation

An algorithm for automatic operation mode has been developed based on a visual servoing, in which the beads are tracked till their final position. The flow chart explaining this algorithm is shown in Figure 4.14. The control algorithm used is as follows:

1. Initialization: Detection of spherical beads using segmentation within an image frame of 500 $\times$ 500 pixels in size.

2. Image templates of beads are taken and search region of interest (ROI) are located at the bead's center of mass.

3. Reference goal positions are introduced by an user through a computer mouse or specified in the program.

4. Close-loop starts: Image correlation starts to the tracking process.

5. The line passing through the bead center of mass position and goal position is computed.

6. Laser-scanner is positioned at a predefined distance d from the bead and the IR laser is shot during an exposure time t_e. The laser position is located at a distance d that belongs to the precomputed line.

7. The ROI position is updated to the present bead position.

8. The bead is placed at the goal position, the laser-scanner is then positioned at its initial position. End of process.

The algorithm tests if the bead reaches the goal position, otherwise it continues to the bead's center of mass calculation. The IR laser is then shot at a distance d belonging to the line passing through the bead and the goal position. The calculation of the bead position is tested. If the bead moves too fast and goes out of the search ROI, the process restarts for detecting the bead location.

Program implementation

The automatic mode is implemented using the C++ language in a windows operating system. A multithreaded program was necessary to perform the tracking process, the IR laser shot with a determined exposure time and the GUI display in an independent manner. A serial program blocks these processes while one of them is performed.
To implement a multithreaded program in C++, OpenMP[2] application programming interface (API) was used. It is an open source library not difficult to be implemented.

Figure 4.15 shows the threads used in the program. Thread1: Image acquisition and GUI display; Thread2: image processing; and Thread3: DAQ NICard, command for laser-scanner and IR laser shot. These threads communicate each other through shared variables. As the threads are asynchronous, these resources must be protected to avoid their overwriting while communicating, otherwise it can cause wrong calculations.

Tracking method and position feedback

The beads have to be tracked in order to know their position at all times. Their positions provide to the system the feedback to know where the laser has to be addressed and if the beads have reached the desired destination.
Image correlation is used to track the beads. Its computing time depends on the ROI size. A ROI size of 100 $\times$ 100 pixel is used and the time to find a bead (10 to 20 pixels in diameter) within this size is about 2 ms.

Figure 4.16 illustrates how the tracking method works. After detection of bead by segmentation, the templates are captured and the ROIs are positioned at the beads' center of mass. Once the correlation is performed in the whole ROI, the bead position is obtained. A line path is then calculated between the bead and goal positions. The laser is shot a distance d from the

[2]OpenMP: Open Multi-Processing API. http://openmp.org

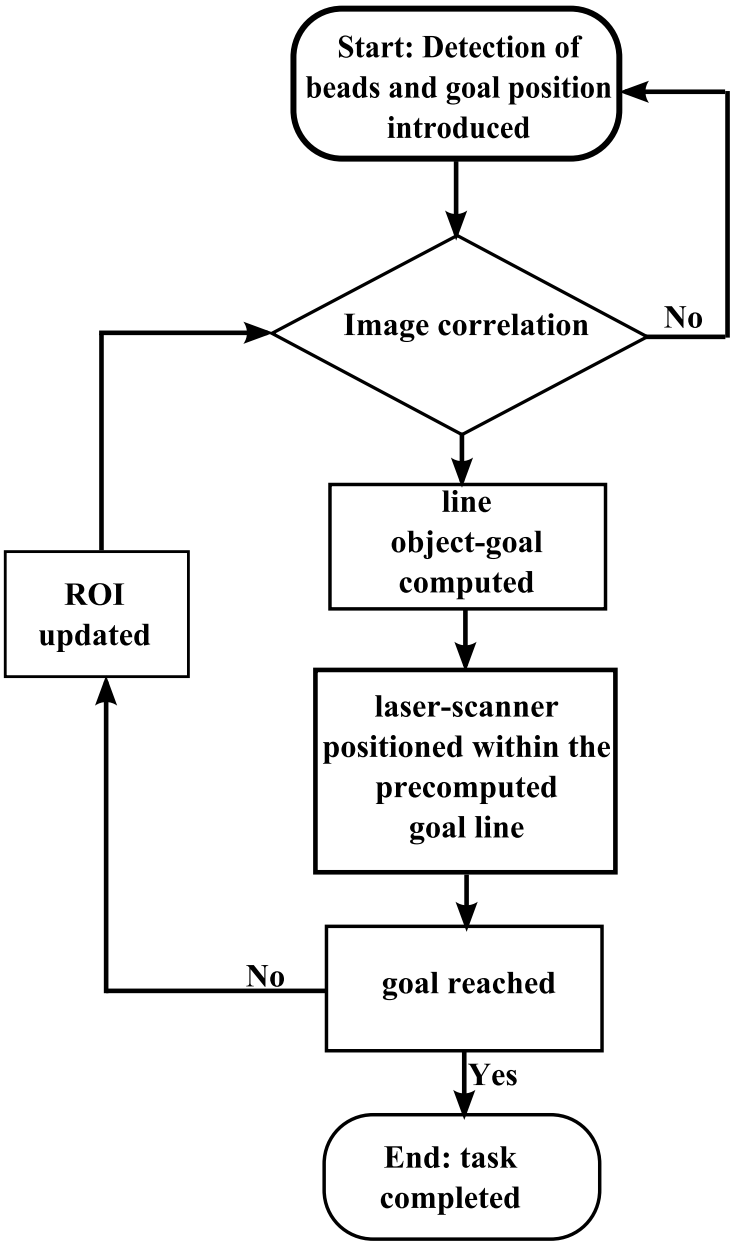

Figure 4.14: Flow chart illustrating the control algorithm used for automation.

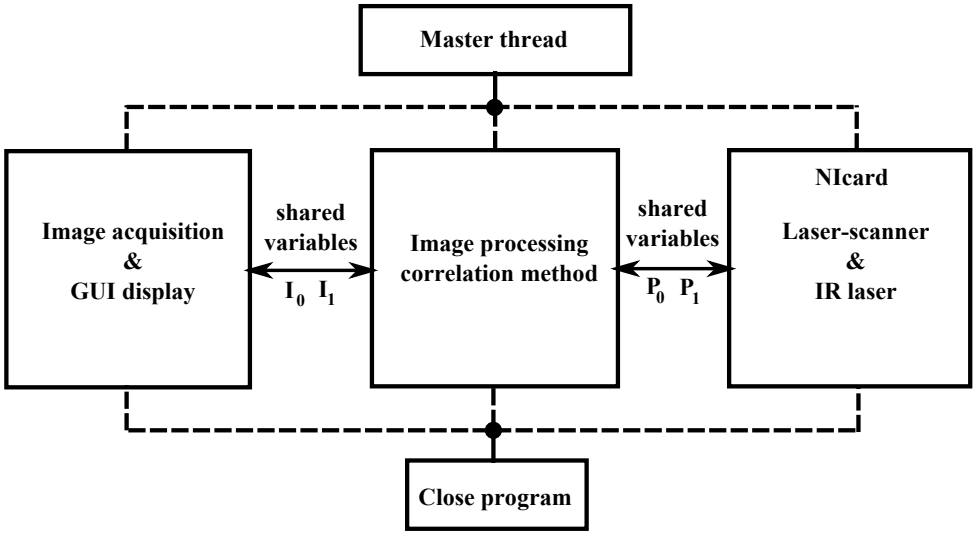

Figure 4.15: Block diagram of the implemented multithreaded program. The main program is divided into three independent programs which communicates between each other with shared and protected variables. $\mathbf{I_{0,1}}$ and $\mathbf{P_{0,1}}$ are images and position shared variables.

bead. The bead is displaced by the laser shot. The correlation is performed in order to compute the new bead position. Once the bead position is computed, the ROI updates its location in order to have the present bead position at the ROI's center. For a new bead position, the line path is recalculated to address the IR in this line.
For each iteration, the distance between the bead and the goal position is compared to a desired accuracy distance introduced in the program. When the bead-goal distance is smaller than the accuracy distance, the process ends. The highest accuracy that the system can achieve is one pixel, which is the position error given by the image correlation process. In the micromanipulation system, one pixel correspond to 5 μm.
The time to achieve the displacement of a bead in a close loop is given by the sum of: the laser exposure time (50-90 ms) and the scanner response time (125 ms) that gives 215 ms. The correlation time (2 ms) is not taken into account because the image correlation is performed in a parallel thread.

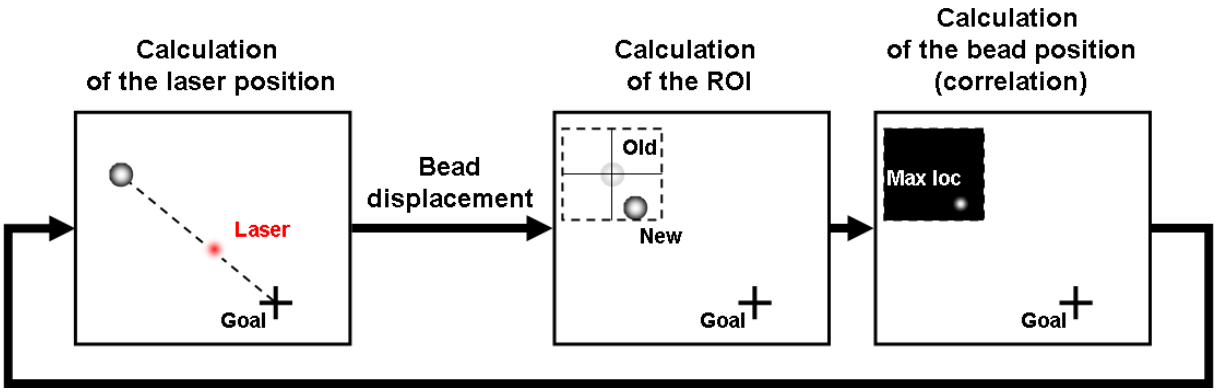

Figure 4.16: Representation scheme of the tracking method using image correlation. The laser is shot to drag the bead, the bead moves and the ROI updates its position to find the bead. Once the bead position is computed, the laser is shot.

Experimental validation

First experiments are aimed to validate the full automation of this novel non-contact manipulation technique. The automatic manipulation of two beads is depicted in Figure 4.17. These beads are 50 and 85 μm in diameter respectively. The water depth is 450 μm
Firstly, the beads are located by the user and contained in an image frame of 500 $\times$ 500 pixels (Figure 4.17(a)). One pixel corresponds to 5 μm in the workspace. Then the detection process is activated by the user on the GUI. A detection filter is also implemented to avoid the detection of impurities or beads smaller than 30 μm and larger than 150 μm in diameter. These parameters can be changed in the program.
Once the beads are detected, the user introduces the goal positions or destinations by clicking with a computer mouse on the video displayed (Figure 4.17(b)). The goal positions are shown by a black circle of 50 μm in radius. This dimension also represents the positioning tolerance. That means when the bead's center of mass is located at a distance smaller the 50 μm from the goal position, the automatic process stops. This tolerance can be changed in the program.
After the introduction of the goal positions, the laser is shot at a distance of 450 μm from each bead during 90 ms of exposure time (Figure 4.17(c)). The laser position is switched from one bead to the other, thus each bead is moved of one step after the other (Figure 4.17(c-h)). This strategy is implemented due to the radial shape of flows. That means for one laser shot all beads go toward the laser if they are close enough.
Due to the different distant destinations, one of the two beads arrives to its goal position faster (cf. Figure 4.17(g)). As a result, the laser will focus on the remaining bead till it reaches its destination. When the two beads are in their respective goal positions the automatic process stops.
The pictures in Figure 4.17(b-h) are shown at an interval of 1 s, taking a time of 6 s, since the user introduces the goal positions, for both beads to arrive to their destinations.

Limitations of the implemented control algorithm

We demonstrated the automation of this method by implementing a simple position feedback, in which the computed error (distance between the bead and goal position) is compared to the tolerance position without regulation. A regulator can be implemented to improve the performances of the system, it can increase the speed and accuracy of the automatic process. For instance, in our program the distance at which the laser is shot is not variable as well as the exposure time. If this parameters are varied with respect to the position error, the bead could move faster when it is far from the goal position and slower when it is close to it. In this way, an accuracy of 1 pixel can be reached in a shorter time. One pixel is the error due to the image correlation.

The main drawback of this method for a multiple bead manipulation is the cross-talk engendered due to the radial symmetry of convection flows with respect to the heat source. The implemented control algorithm does not take into account this cross-talk. A more sophisticated algorithm has to be implemented with a suitable regulator.

Apart from the control algorithm, to better address the cross-talk a faster laser-scanner is required. Thus the laser can switch from one bead to another much faster or to produce dedicated patterns almost in parallel in order to reduce the cross-talk. The laser-scanner used has a response time of about 125 ms.

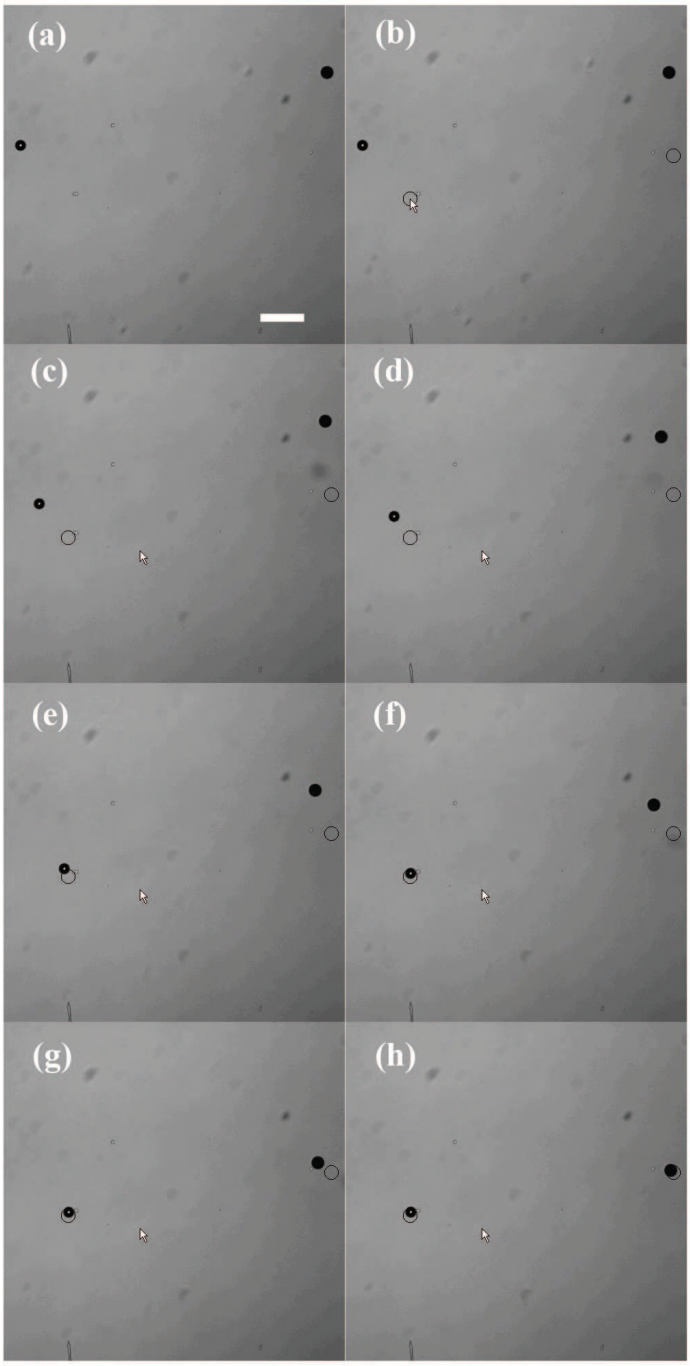

Figure 4.17: Image sequence depicting the automatic manipulation of two beads. (a) The bead positions are detected by the program. (b) The user introduces the respective goal positions with a computer mouse by only clicking on the image frame. (c-h) The IR laser is shot by switching from one bead to the other till the beads arrive to destination. The pictures are shown at intervals of 1 s. Scale bar of 200 μm

4.4 Conclusions

In this chapter a first fully automated non-contact fluidic-based micromanipulation system using visual servoing is presented. Immersed spherical beads ranging from 30 up to 250 μm in diameter can be handled manually and autonomously.
The automatic manipulation of two spherical beads is successfully achieved and presented. A laser-scanner device is used to address an IR laser to a specified position with respect to the beads and their destinations. The IR laser generates localized convection flows close to the beads, these flows are used to drag the beads to their destinations.
In addition, a manual operation mode is proposed. It allows an user to handle micro-parts by only clicking with a computer mouse on a image frame displayed on a GUI.

The operation modes developed show the feasibility of handling micro-parts within a liquid medium. This is of great interest for the fabrication of microdevices, self-assembly or production with batch processes in the mesoscale. Moreover, our system can be extended to handle biological cells either in manual or automatic operation modes.

The main drawbacks of this method for a parallel manipulation of single beads, is the cross-talk engendered by the flows. In order to reduce that, a better control algorithm has to be studied and developed. Moreover, a better control algorithm will allow to enhance greatly the performance of the method proposed in terms of rapidity, accuracy and number of beads to be handled.
Future work will deal with the study of better control and image processing algorithms for multiple beads and non-spherical micro-objects manipulation in an autonomous manner.

Conclusions and Perspectives

In this work, a novel contactless micromanipulation technique in fluid medium is developed. Handling micro-parts in the 1 - 100 μm range is an actual challenge for the industrialization of new products based on opto-electro-mechanical components, namely MEMS, OLEDs etc. All this components are fabricated from bulk on silicon or similar wafers and the production of complex systems requires reliable assembly process.
The manipulation technique proposed here is based on the use of thermal induced convection flows in liquid. The Marangoni effect is a torus shaped flow generated around a local heat source in a fluid. The micromanipulation setup designed and constructed in this work generates controllably these Marangoni convection flows using a single laser beam. A full closed loop operation is possible thanks to implemented high frequency vision feedback and image treatment. The high dynamic and controllability of the system makes it suitable for massive parallel manipulation and assembly.

In the first chapter, an overview of different micromanipulation methods is given with a comparison of contact and non-contact techniques. These analysis points some advantages of contactless techniques, especially when the size and the shape of the objects may vary. Additionally, contactless methods in liquid allow to minimize the effects of adhesion phenomena, which are the most dominant forces at this scale.
Among the liquid convection phenomena, Marangoni effect stands out because of its ability to generate locally high-speed flows. The strength of these flows and their spatial distribution are enough to drag several micro-parts in parallel. Moreover, as this phenomenon is based on surface forces (proportional to L), it is more suitable for miniaturisation than free convection which is based on body forces (proportional to L^3). Their theoretical and experimental analysis is presented in chapter 2. This analysis shows that this method can be implemented by using a single laser beam as a heat source. The main advantage advantage of using a laser is that it can be focused in a very small surface, thus obtaining a very localized convection flows.
Additionally, different fluidic flow patterns can be easily performed only by scanning the laser beam on the sample.

The third chapter describes the experimental setup designed and constructed for Marangoni-effect based fluid micromanipulation. The system is composed of an optical microscope, a scanner holding a mirror to address the laser at any point on the manipulation area and a fast camera based vision system. This system is then characterized in its technical specificities and is used to define physical parameters influencing the Marangoni effect, such as the water depth, object shapes and dimensions the laser power.

The fourth chapter takes the robotic implementation one step further. Based on the cal-

ibration physical and technical specificities of the manipulation system, a full automation is implemented. The control loop is closed using vision feedback. In this purpose, several image treatment techniques are investigated in order to implement a high speed feedback loop. Image correlation is used to track the beads on real time. This method is robust to noise and fast enough, allowing to compute the positions of several beads for multiple beads manipulation. Two operation modes are implemented. The first one is the manual operation where the user controls directly the laser focal point's position. The second one is an automatic mode. A full automation algorithm is implemented using complete closed-loop vision servoing. The user just points the target position and the system drags the object at that desired location. This mode is also experimentally validated in a multiple manipulation scenarii. In this experiments, the user defines 2 target positions for two beads and the system moves them to these desired locations without further user interaction.

The developed techniques show the feasibility of parallel handling micro-parts within a liquid medium using convection flows. This is of great interest for the fabrication of microdevices, self-assembly or production with batch processes in the mesoscale. Moreover, our system can be extended to handle biological cells either in manual or automatic operation mode.
This work opens several perspectives, through a more reliable analysis of the fluidic convection or by increasing the technical capabilities of the scanner and the vision system, in order to be able to address larger populations of microparts.

Bibliography

Abidin, Z. Z., & Markx, G. H. 2005. High-gradient electric field system for the dielectrophoretic separation of cells. *Journal of Electrostatics*, **63**, 823–830.

Adamson, A. W., & Gast, A. P. 1997. *Physical Chemistry of Surfaces*. 6 edn. Wiley-Interscience Publication.

Agarwal, R., Ladavac, K., Roichman, Y., Yu, G., Lieber, C., & Grier, D. 2005. Manipulation and assembly of nanowires with holographic optical traps. *Optics Express*, **13**(22), 8906–8912.

Arai, F., Yoshikawa, K., Sakami, T., & Fukuda, T. 2004. Synchronized laser micromanipulation of multiple targets along each trajectory by single laser. *Applied Physics Letters*, **85**(19), 4301.1–4301.3.

Arai, F., Endo, T., Yamuchi, R., & Fukuda, T. 2006. 3D 6DOF manipulation of micro-objects using laser-trapped microtool. *In: IEEE International Conference on Robotics and Automation.*

Ashkin, A. 1970. Acceleration and trapping of particles by radiation pressure. *Physical Review Letters*, **24**(4), 156–159.

Ashkin, A. 1992. Forces of a single-beam gradient laser trap on a dielectric sphere in the ray optics regime. *Biophysical Journal*, **61**(2), 569–582.

Ashkin, A., & Dziedzic, J. M. 1971. Optical levitation by radiation pressure. *Applied Physics Letters*, **19**(8), 283–285.

Ashkin, A., Schuetze, K., Dziedzic, J.M., Euteneuer, U., & Schliwa, M. 1990. Force generation of organelle transport measured in vivo by an infrared laser trap. *Nature*, **348**, 346–348.

Assi, F., Jenks, R., Yang, J., Love, Ch., & Prentiss, M. 2002. Massively parallel adhesion and reactivity measurements using simple and inexpensive magnetic tweezers. *Journal of Applied Physics*, **92**(9), 5584–5586.

Basu, A. S., & Gianchandani, Y. B. 2009. A Programmable Array for Contact-Free Manipulation of Floating Droplets on Featureless Substrates by the Modulation of Surface Tension. *Journal of Microelectromechanical Systems*, **18**, 1163–1172.

Basu, A. S., & Gianchandani, Y. E. 2005 (June). Trapping and Manipulation of Particles and Droplets using Micro-toroidal Convection Currents. *Pages 85–88 of: TRANSDUCERS'O5, The 13th International Conference on Solid-state Sensors, Actuators and Microsystems.*

Basu, A. S., Yee, S. Y., & Gianchandani, Y. B. 2007. Virtual Components for Droplet Control using Marangoni Flows: Size-Selective Filters, Traps, Channels, and Pumps. *Pages 401–404 of: MEMS 2007.*

Basu, Amar S., & Gianchandani, Yogesh B. 2007. Shaping high-speed Marangoni flow in liquid films by microscale perturbations in surface temperature. *Applied Physics Letters*, **90**(3), 034102.1–034102.3.

Basu, Amar S, & Gianchandani, Yogesh B. 2008. Virtual microfluidic traps, filters, channels and pumps using Marangoni flows. *JOURNAL OF MICROMECHANICS AND MICROENGINEERING*, **18**(11), 115031.1–115031.11.

Becker, F., Gascoyne, P., Huang, Y., & Wang, X.-B. 1999. Method and apparatus for manipulation using spiral electrodes. *Brevet 5,858,192*, **USA**.

Bénard, H. 1900. Les tourbillons cellulaires dans une nappe liquide. *Rev. Gen. Sci. Pures Appl.*, **11**, 1261–1271.

Boer, G., Johann, R., Rohner, J., Merenda, F., Delacretaz, G., Renaud, Ph., & Salathe, R.-P. 2007. Combining multiple optical trapping with microflow manipulation for the rapid bioanalytics on microparticles in a chip. *Review of Scientific Instruments*, **78**(11), 116101–3.

Burns, M A, Mastrangelo, C H, Sammarco, T S, Man, F P, Webster, J R, Johnsons, B N, Foerster, B, Jones, D, Fields, Y, Kaiser, A R, & Burke, D T. 1996. Microfabricated structures for integrated DNA analysis. *Proceedings of the National Academy of Sciences of the United States of America*, **93**(11), 5556–5561.

Chen, Xiaowei, Zhou, Xiaobo, & Wong, Stephen T. C. 2006. Automated Segmentation, Classification, and Tracking of Cancer Cell Nuclei in Time-Lapse Microscopy. *IEEE TRANSACTIONS ON BIOMEDICAL ENGINEERING*, **53**(4), 762–766.

Chiou, Pei Yu, Ohta, Aaron T., & Wu, Ming C. 2005. Massively parallel manipulation of single cells and microparticles using optical images. *Nature letters*, **436**(7049), 370–372.

Chu, S. 1991. Laser Manipulation of Atoms and Particles. *Science*, **253**(5022), 861 – 866.

Cordero, M. L., Burnham, D. R., Baroud, Ch. N., & McGloin, D. 2008. Thermocapillary manipulation of droplets using holographic beam shaping: Microfluidic pin ball. *Applied Physics Letters*, **93**(3), 034107.1–034107.3.

Curtis, J. E., Koss, B. A., & Grier, D. G. 2002. Dynamic holographic optical tweezers. *Optics Communications*, **207**(1), 169–175.

DaCosta, German. 1993. Optical visualization of the velocity distribution in a laser-induced thermocapillary liquid flow. *APPLIED OPTICS*, **32**(12), 2143–2151.

Darhuber, A. A., Valentino, J. P., Troian, S. M., & Wagner, S. 2003. Thermocapillary Actuation of Droplets on Chemically Patterned Surfaces by Programmable Microheater Arrays. *Journal of Microelectromechanical Systems*, **12**(6), 873–879.

Darhuber, Anton A., & Troian, Sandra M. 2005. PRINCIPLES OF MICROFLUIDIC ACTUATION BY MODULATION OF SURFACE STRESSES. *Annu. Rev. Fluid Mech.*, **37**, 425–455.

Dionnet, F., Regnier, S., & Guinot, J. C. 2004 (May). Vision and Force Based Autonomous Micromanipulation. *Pages 5019–5024 of: IEEE Int. Conf. on Robotics and Automation*, vol. 5.

Emiliani, V., Sanvitto, D., Zahid, M., Gerbal, F., & Coppey-Moisan, M. 2004. Multiforce optical tweezers to generate gradients of forces. *Optics Express*, **12**.

Emiliani, V., Cojoc, D., Ferrari, E., Garbin, V., Durieux, Ch., Coppey-Moisan, M., & Di Fabrizio, E. 2005. Wave front engineering for microscopy of living cells. *Optics Express*, **13**(5), 1395–1405.

Farahi, R. H., Passian, A., Ferrell, T. L., & Thundat, T. 2004. Microfluidic manipulation via Marangoni forces. *Applied Physics Letters*, **85**(18), 4237–4239.

Ferrari, E., Emiliani, V., Cojoc, D., Garbin, V., Zahid, M., Durieux, C., Coppey-Moisan, M., & Fabrizio, E. Di. 2005. Biological samples micro-manipulation by means of optical tweezers. *Microelectronic Engineering*, **78-79**(Mar.), 575–581.

Frenea, M., Faure, S., Pioufle, B. L., Coquet, P., & Fujita, H. 2003. Positioning living cells on a high-density electrode array by negative dielectrophoresis. *Material Science and Engineering*, **C23**, 597–603.

Furlani, E. P. 2007. Magnetophoretic separation of blood cells at the microscale. *J. Phys. D: Appl. Phys.*, **40**(5).

Gascoyne, P., & Vikoukal, J. 2004. Dielectrophoresis-Based Sample Handle in General-Purpose Programmable Diagnostic Instruments. *In: IEEE Proceedings.*

Gelles, Jeff, Schnapp, Bruce J., & Scheetz, Michael P. 1998. Tracking kinetic-driven movements with nanometric scale precision. *Nature*, **331**(4), 450–453.

Goksör, M., Enger, J., & Hanstorp, D. 2004. Optical manipulation in combination with multiphoton microscopy for single-cell studies. *Applied Optics*, **43**(25), 4831–4837.

Grier, A., & Lopes, W. 2007. Apparatus and method to generate and control optical traps to manipulate small particles. *USA Patent 7 161 140.*

Guyon, E., Hulin, J-P., & Petit, L. 2001. *Hydrodynamique Physique.* EDP, Sciences/CNRS Editions.

Haake, A., & Dual, J. 2002. Micro-manipulation of small particles by node position control of an ultrasonic standing wave. *Ultrasonics*, **40**(1-8), 317–322.

Hafez, Moustapha. 2000. *Compact fast-steering tip/tilt laser scanner for high power material processing applications.* Ph.D. thesis, EPFL.

Hollis, A., Rastegar, S., Descloux, L., Delacréttaz, G., & Rink, K. 1996. Analysis of Dynamics of Zona Pellucida Microdrilling by a 1.48μm Diode Laser. *Pages 2059–2060 of: IEEE Engineering in Medicine and Biology Society.*

Holmlin, R. E., Schiavoni, M., Chen, C. Y., Smith, S. P., Prentiss, M. G., & Whitesides, G. M. 2000. Light-driven microfabrication: Assembly of multicomponent, three-dimensional structures by using optical tweezers. *Angew. Chem.*, **39**(19), 3503–3506.

Hunt, T. P., Lee, H., & Westervelt, R. M. 2004. Addressable micropost array for the dielectrophoretic manipulation of particles in fluid. *Applied Physics Letters*, **85**(26), 6421–6423.

Ishibashi, I., Perry, C. III, & Agarwal, T. K. 1994. Experimental determinations of contact friction for spherical glass particles. *Soils and foundations*, **34**(4), 79–84.

Jähnisch, M., & Fatikow, S. 2007. 3-D Vision Feedback for Nanohandling Monitoring in a Scanning Electron Microscope. *International Journal of Optomechatronics Technologies*, **1**, 4–27.

Johnson, Richard W. (ed). 1998. *The Handbook of fluid dynamics*. CRC Press and Springer-Verlag.

Jones, Th. B. 2003. Basic Theory of Dielectrophoresis and Electrorotation. *IEEE Engineering in Medicine and Biology Magazine*, 33–42.

Kataoka, Dawn E., & Troian, Sandra M. 1999. Patterning liquid flow on the microscopic scale. *Nature*, **402**(6763), 794–797.

Kemshead, J. T., & Ugelstad, J. 1985. Magnetic separation techniques: their applications to medicine. *Molecular and Cellular Biochemistry*, **67**, 11–18.

Lee, H., Purdon, A. M., & Westervelt, R. M. 2004. Manipulation of biological cells using a microelectromagnet matrix. *Applied Physics Letters*, **85**(6), 1063–1065.

Longtin, J P., Hijikata, K, & Ogawa, K. 1999. Laser induced surface tension driven flows in liquids. *International Journal of Heat and Mass Transfer*, **42**(1), 85–93.

Manneberg, O., Vanherberghen, B., Önfelt, B., & Wiklund, M. 2009. Flow-free transport of cells in microchannels by frequency-modulated ultrasound. *Lab on a Chip*, **9**(6), 833–837.

Marangoni, Carl. 1871. Ueber die Ausbreitung der Tropfen einer Flüssigkeit auf der Oberfläche einer anderen. *Annalen der Physik*, **219**(7), 337–354.

Maroto, J. A., Pérez-Munuzuri, V., & Romero-Cano, M. S. 2007. Introductory analysis of Bénard-Marangoni convection. *EUROPEAN JOURNAL OF PHYSICS*, **28**, 311–320.

Merenda, F., Rohnera, J., Lamothea, E., P. Pascoal, J.-M. Fourniera, & Salathé, R-P. 2007. Micro-Optics for Optical Trapping in Microfluidics. *Page 66440P of: SPIE*, vol. 6644.

Moesner, Felix M., & Higuchi, Toshiro. 1997 (October). Contactless Manipulation of Microparts by Electric Field Traps. *Pages 168–175 of: SPIE's International Symposium on Microrobotics and Microsystem Fabrication*, vol. 3202.

Nambiar, R., Gajraj, A., & Meiners, J.-C. 2004. All-Optical Constant-Force Laser-Tweezers. *Biophysical Journal*, **87**, 1972–1980.

Ohta, A. T., Jamshidi, A., Valley, J. K., Hsu, H-Y., & Wu, M. C. 2007. Optically actuated thermocapillary movement of gas bubbles on an absorbing substrate. *Applied Physics Letters*, **91**(7), 074103.1–074103.3.

Pal, N. R., & Pal, S. K. 1993. A Review on Image Segmentation Techniques. *Pattern Recognition*, **26**(9), 1277– 1294.

Pawashe, Chytra, & Sitti, Metin. 2006. Two-dimensional vision-based autonomous microparticle manipulation using a nanoprobe. *Journal of Micromechatronics*, **3**(3–4), 285–306.

Pearson, J. R. A. 1958. On convection cells induced by surface tension. *Journal of Fluid Mechanics*, **4**(5), 489–500.

Petersson, Filip, Aberg, Lena, Swärd-Nilsson, Ann-Margret, & Laurell, Thomas. 2007. Free Flow Acoustophoresis:? Microfluidic-Based Mode of Particle and Cell Separation. *Analytical Chemistry*, **79**(14), 5117–5123.

Pohl, H. A. 1950. The Motion and Precipitation of Suspensoids in Divergent Electric Fields. *Journal of Applied Physics*, **22**(7), 869–871.

Politano, D. C., Prati, P. V., Woo, S-J, Homan, O. J., Moesner, F. M., & Stemmer, A. 1998. Dielectrophoretic Handling of Mesoscopic Objects. *Pages 66–71 of: Fourth International Conference on Motion and Vibration Control MOVIC' 98.*

Pollack, M. G., Fair, R. B., & Shenderov, A. D. 2000. Electrowetting-based actuation of liquid droplets for microfluidic applications. *Applied Physics Letters*, **77**(11), 1725–1726.

Probst, Martin, Hürzeler, Christoph, Borer, Ruedi, & Nelson, Bradley J. 2009. A Microassembly System for the Flexible Assembly of Hybrid Robotic MEMS Devices. *International Journal of Optomechatronics*, **3**(2), 69–90.

Ramsay, W., & Shields, J. 1893. The Molecular Complexity of Liquids. *Journal of Chemical Society*, **LXXXI**, 1089–1103.

Reddy, G. D., & Saggau, P. 2005. Fast three-dimensional laser scanning scheme using acousto-optic deflectors. *Journal of Biomedical Optics*, **10**(6), 064038–10.

Ren, Hong, Fair, Richard B., Pollack, Michael G., & Shaughnessy, Edward J. 2002. Dynamics of electro-wetting droplet transport. *Sensors and Actuators B: Chemical*, **87**(1), 201–206.

Roselier, S., & Hafez, M. 2006. ViFlex: A Compact Haptic 2D Interface with Force Feedback for Mobile Devices. *Pages 93–104 of: EuroHaptics.*

Rosenthal, A., & Voldman, J. 2005. Dielectrophoresis Traps for Single-Particles Patterning. *Biophysical Journal*, **88**.

Sasaki, K., Koshioka, M., Misawa, H., Kitamura, N., & Masuhara, H. 1991. Pattern formation and flow control of fine particles by laser-scanning micromanipulation. *Optics Letters*, **16**(19), 1463–1465.

Schnelle, Th., Müller, T., & Fuhr, G. 2000. Trapping in AC octode field cages. *Journal of Electrostatics*, **50**, 17–29.

Seo, H.-W., Han, C.-S., Choi, D.-G., King, K.-S., & Lee, Y.-H. 2005. Controlled assembly of single SWNTs bundle using dielectrophoresis. *Microelectronic Engineering*, **81**, 83–89.

Shi, Jinjie, Ahmed, Daniel, Mao, Xiaole, Lin, Sz-Chin Steven, Lawit, Aitan, & Huang, Tony Jun. 2009. Acoustic tweezers: patterning cells and microparticles using standing surface acoustic waves (SSAW). *Lab on a Chip*, **9**, 2890–2895.

Sitti, M., & Hashimoto, H. 2000. Two-Dimensional Fine Particle Positioning Under Optical Microscope Using a Piezoresistive Cantilever as a Manipulator. *Journal of Micromechatronics*, **1**(1), 25–48.

Straub, J. 1993. *VDI-Heat Atlas.* VDI-Verlag.

Suehiro, J., Zhou, G., Imamura, Manabu, & Hara, Masanori. 2003. Dielectrophoretic Filter for Separation and Recovery of Biological Cells in Water. *IEEE Transactions on Industry Applications*, **39**(5), 1514–1521.

Svoboda, K, & Block, S M. 1994. Biological Applications of Optical Forces. *Annual Review of Biophysics and Biomolecular Structure*, **23**(1), 247–285.

Tanaka, Yoshio, Kawada, Hiroyuki, Hirano, Ken, Ishikawa, Mitsuru, , & Kitajima, Hiroyuki. 2008. Automated manipulation of non-spherical microobjects using optical tweezers combined with image processing techniques. *Optics Express*, **16**(19), 15115–15122.

Vela, E., Pacoret, C., Bouchigny, S., Régnier, S., Rink, K., & Bergander, A. 2008 (September). Non-contact Mesoscale Manipulation Using Laser Induced Convection Flows. *Pages 913–918 of: IEEE/RSJ International Conference on Intelligent Robots and Systems.*

Vela, E., Hafez, M., & Régnier, S. 2009. Laser-Induced Thermocapillary Convection for Mesoscale Manipulation. *International Journal of Optomechatronics*, **3**(4), 289–303.

Velev, O. D., & Bhatt, K. H. 2006. On-chip micromanipulation and assembly of colloidal particles by electric fields. *Soft Matter*, **2**, 738–750.

Yan, J., Skoko, D., & Marko, J. 2004. Near-field-magnetic-tweezer manipulation of single DNA molecules. *Physical Review E*, **70**(1), 011905–5.

Yu, S., & Nelson, B. 2002. Biological Cell Injection Using an Autonomous MicroRobotic System. *The International Journal of Robotics Research*, **21**(10-11), 861–868.

Yu, Sun, & Nelson, Bradley J. 2001. Autonomous Injection of Biological Cells Using Visual Servoing. *Pages 169–178 of: Experimental Robotics VII*, vol. 271. Springer Berlin / Heidelberg.

Zborowski, M., Ostera, G. R., Moore, L. R., Milliron, S., Chalmers, J. J., & Schechter, A. N. 2003. Red blood cell magnetophoresis. *Biophysical Journal*, **84**, 2638–2645.